Distribution Agreement

In presenting this thesis or dissertation as a partial fulfillment of the requirements for an advanced degree from Emory University, I hereby grant to Emory University and its agents the non-exclusive license to archive, make accessible, and display my thesis or dissertation in whole or in part in all forms of media, now or hereafter known, including display on the world wide web. I understand that I may select some access restrictions as part of the online submission of this thesis or dissertation. I retain all ownership rights to the copyright of the thesis or dissertation. I also retain the right to use in future works (such as articles or books) all or part of this thesis or dissertation.

Signature:

_____ _____

Michael McKinnon Date

Characterization of Thoracic Sympathetic Postganglionic Neurons

By

Michael McKinnon
Doctor of Philosophy

Graduate Division of Biological and Biomedical Science
Neuroscience

_____

Shawn Hochman
Advisor

_____

Arthur English
Committee Member

_____

Sandra Garraway
Committee Member

_____

Marie-Claude Perreault
Committee Member

_____

Astrid Prinz
Committee Member

Accepted:

_____

Lisa A. Tedesco, Ph.D.
Dean of the James T. Laney School of Graduate Studies

_____

Date

Characterization of Thoracic Sympathetic Postganglionic Neurons

By

Michael McKinnon
BS, Georgia Institute of Technology, 2012

Advisor: Shawn Hochman, Ph.D.

An abstract of
A dissertation submitted to the Faculty of the
James T. Laney School of Graduate Studies of Emory University
in partial fulfillment of the requirements for the degree of
Doctor of Philosophy
in Neuroscience
2019

Abstract

Characterization of Thoracic Sympathetic Postganglionic Neurons

By

Michael McKinnon

Thoracic sympathetic postganglionic neurons (tSPNs) comprise the final output of the distributed sympathetic nervous system controlling vascular and thermoregulatory systems. Traditionally considered a non-integrating relay, what little is known of tSPN intrinsic excitability has been determined by sharp microelectrodes with presumed impalement injury. We thus undertook the first electrophysiological characterization of mouse tSPN cellular and synaptic properties using whole-cell recordings and coupled results with a conductance-based model to explore the principles governing tSPN excitability.

Input resistance and time constant values were an order of magnitude greater than values reported elsewhere, leading to much lower rheobase. All cells were capable of repetitive firing, in contrast to prior reports. We used the computational model to explain observed phenomena and to account for the differences in observed properties compared to prior recordings. Frequency of spontaneous events (sEPSCs) was highly variable between cells. Amplitude of sEPSCs averaged 40pA, and evoked synaptic events ranged from approximately the same size as sEPSCs to an order of magnitude greater. Values of time constant were consistent with kinetic properties of $\alpha 3\beta 4$ nicotinic receptors. sEPSCs were not blocked by TTX, indicating that they occur in the absence of action potentials.

We then explored changes that might occur in these neurons after high thoracic spinal cord transection (SCI) that would lead to emergent autonomic dysfunction. Three to six weeks after SCI, tSPN intrinsic membrane properties were comparable to controls, but frequency and amplitude of spontaneous preganglionic synaptic activity was increased, potentially a homeostatic response to SCI-induced decreased presynaptic drive. Overall, this suggests that while the intrinsic excitability of tSPNs is unaltered after SCI, they are likely to be driven more robustly by SCI-induced increases in presynaptic drive.

Taken together, whole-cell recordings reveal tSPNs have more dramatically amplified excitability than previously thought, with greater intrinsic capacity for synaptic integration and with the ability for maintained firing to support sustained actions on vasomotor tone and thermoregulatory function. Rather than acting as a relay, these studies support a more responsive role and possible intrinsic capacity for tSPNs to drive sympathetic autonomic function.

Characterization of Thoracic Sympathetic Postganglionic Neurons

By

Michael McKinnon
BS, Georgia Institute of Technology, 2012

Advisor: Shawn Hochman, Ph.D.

A dissertation submitted to the Faculty of the
James T. Laney School of Graduate Studies of Emory University
in partial fulfillment of the requirements for the degree of
Doctor of Philosophy
in Neuroscience
2019

ACKNOWLEDGEMENTS

I want to thank the people who have helped and encouraged me through this process. It has been, by far, the most trying endeavor I have ever undertaken and it would not have been possible without the support and encouragement of my friends, family, and lab mates.

First to my family, I want to thank all of you for your patience. This journey has been long and often frustrating, but you've always been right there cheering me on. I hope I've made you proud. To David, my husband, thank you for being a friend. My life is so much better with you in it. To my amazing friends, those I had coming into grad school and those I've made while here, your friendship, support, and understanding mean the world to me.

To my committee, Astrid Prinz, Sandra Garraway, Marie-Claude Perreault, and Art English, thank you for your guidance and helpful suggestions along the way. I want to thank the members of the Prinz lab as well. Kun Tian, the computational model you developed was crucial to many of the conclusions made in this document. David Stockton, your fitting algorithm saved me many hours of work.

To my lab mates, this would not have happened without you. Jacob, you taught me to enjoy my time in grad school, and I may have taken your advice a little too seriously. Shaquia, you've been a wonderful friend, and I'm sorry I hit you with a snowball the first day I met you—I was aiming at Don. Maka, your snarky sense of humor made lab so much more fun, and I hope you're enjoying life out in the real world! Heidi, you're a statistics queen. You're the reason the whole paper isn't just a hundred t-tests. Celia, this would have been a much less impressive dissertation

without you. You single-handedly doubled the amount of data available for my project, and I'm so happy you decided to learn how to patch postganglionics. Mallika, I think this project owes its success as much to you as it does to me. You figured out how to dissect the mouse sympathetic chain and proved that this project was even possible. Let me know anytime you want to take an excursion to Buford Highway. Bubble tea is on me. Don likes unicorns (personal observation, see also Shreckengost, 2011). Mike, you are an endless fountain of knowledge and expertise. You're truly the most interesting man in the world, and if even half of the stories you tell us are true, Dos Equis made the wrong choice. And finally, Shawn, you've been an amazing mentor, advocate, and friend. I can't imagine doing this project with anyone else. I'm going to miss my time in the Hochman lab.

Specific Contributions

Camila Makhlouta, Mi Hyun Choi, and Meredith Lucy Galvin completed the studies on the microanatomy of tSPNs depicted in Figure 1.3 under the supervision of Dr. Alan Sokoloff. Kun Tian created the single-compartment conductance based model and performed critical analyses. Dr. Yaqing Li recorded a significant portion of the whole-cell recordings and the majority of spinal cord injury data, and contributed analysis on post-injury intrinsic property data. I collaborated with Dr. David Stockton to create the algorithm used to extract the amplitude and time constants from spontaneous synaptic events. Dr. Shawn Hochman was instrumental in editing this dissertation to its final form (for better or worse), with additional edits suggested by Dr. Astrid Prinz, Dr. Sandra Garraway, Dr. Marie-Claude Perreault, and Dr. Arthur English.

LIST OF FIGURES

LIST OF TABLES

LIST OF ABBREVIATIONS

ACh	acetylcholine
AD	autonomic dysreflexia
ANS	autonomic nervous system
AP	action potential
AR	adrenoceptor
ATP	adenosine triphosphate
cAMP	cyclic AMP
CART	cocaine and amphetamine-regulated transcript
CGRP	calcitonin gene-related peptide
ChAT	choline acetyltransferase
ChR2	channelrhodopsin
C_m	membrane capacitance
CRE	CRE recombinase
CRF	corticotropin-releasing factor
CVLM	caudal ventrolateral medulla
DRG	dorsal root ganglion
eEPSC	evoked excitatory postsynaptic potential
eGFP	enhanced green fluorescent protein
ENS	enteric nervous system
EPSP	excitatory postsynaptic potential
f	frequency
fAHP	fast afterhyperpolarization

g_{in}	input conductance
g_X	X-conductance
G_X	maximal X-conductance
IC	intercalated nucleus
ICpe	paraependymal intercalated nucleus
IFR	instantaneous firing rate
IML	intermediolateral nucleus pars principalis
IMLf	Intermediolateral nucleus pars funicularis
IP_3	inositol triphosphate
IPSP	inhibitory postsynaptic potential
-IR	immunoreactive
I_X	X-current
L1…L5	lumbar level 1…5
LHRH	luteinizing hormone-releasing hormone
LSG	lumbar sympathetic ganglion
LST	lumbar sympathetic trunk
mAChR	muscarinic acetylcholine receptor
nAChR	nicotinic acetylcholine receptor
NGF	nerve growth factor
NO	nitric oxide
NPY	neuropeptide Y
NTS	nucleus of the solitary tract
PAG	periaqueductal gray

PLC	phospholipase C
PNS	parasympathetic nervous system
PO	preoptic area of the hypothalamus
PVN	paraventricular nucleus of the hypothalamus
Q_{10}	coefficient of temperature dependence
R_{in}	input resistance
RMP	resting membrane potential
RVLM	rostral ventrolateral medulla
RVMM	rostral ventromedial medulla
sAHP	slow afterhyperpolarization
SCG	superior cervical ganglion
SCI	spinal cord injury
sEPSC	spontaneous excitatory post-synaptic current
SNS	sympathetic nervous system
SP	substance P
SRA	spike rate adaptation
T1…T13	thoracic level 1…13
TdTomato	red fluorescent protein variant
TH	tyrosine hydroxylase
tSPN	thoracic sympathetic postganglionic neuron
TTX	tetrodotoxin
usAHP	ultra-slow AHP
VIP	vasoactive intestinal peptide

VTA	ventral tegmental area
τ_D	decay time constant
τ_m	membrane time constant
τ_R	rise time constant

TABLE OF CONTENTS

1 Introduction

The sympathetic nervous system (SNS) is the division of the autonomic nervous system largely responsible for vasoregulation, thermoregulation, cardioregulation, and respiration. Such processes are critical for maintenance of homeostasis, and perturbations to this system can be devastating to patients suffering from dysautonomic conditions like autonomic dysreflexia. It is therefore of critical importance to understand both the normal functioning of sympathetic neurons, as well as any maladaptive changes that may occur after spinal cord injury. This dissertation begins with a general overview of what is known about the sympathetic nervous system presented alongside our own anatomical observations. I then describe original research on the intrinsic and synaptic properties of sympathetic ganglia before and after spinal cord injury. I conclude with a series of unanswered questions that have been raised by this work. Detailed methodology is provided at the end.

1.1 Overview of the sympathetic nervous system

The field of autonomic research originated with Langley's classical experiments around the turn of the 20th century (Langley, 1903). Langley coined the term "autonomic nervous system" (ANS) to differentiate this division of the nervous system from the sensory and motor systems. Langley further proposed dividing the ANS into three anatomically defined systems: the sympathetic nervous system (SNS), the parasympathetic nervous system (PNS), and the enteric nervous system (ENS) (Langley, 1921). The SNS and PNS are commonly thought to have reciprocal actions on target tissues, but this represents an overly simplified viewpoint (Jänig, 2006). The remainder of this dissertation will focus on the SNS; the physiology of the PNS and ENS are beyond the scope of this dissertation. For a thorough overview of the entire ANS, see Jänig 2006.

Various subcortical and brainstem nuclei (*e.g.* RVLM, PVN, Raphe, etc.) comprise the control center of the SNS (Guyenet, 2006; Jänig, 2006). These nuclei integrate relevant physiological signals and project to sympathetic preganglionic neurons in the spinal cord. Preganglionic neurons in the thoracolumbar spinal cord comprise the final common output of the SNS (Janig, 1986). Preganglionic neurons are cholinergic and synapse onto postganglionic neurons in sympathetic ganglia. Postganglionic neurons in turn innervate and control vasculature in muscle, skin and visceral organs, as well as piloerector muscles, sweat glands, and brown adipose tissue (Jänig, 2006; Bartness et al., 2010). The majority of postganglionic neurons are adrenergic, while a few are cholinergic. Postganglionic neurons may reside in prevertebral or paravertebral ganglia. Prevertebral ganglia such as the coeliac ganglia and superior/inferior mesenteric ganglia are associated with one or more visceral organs in a discrete location. Paravertebral ganglia are associated with distributed structures such as vasculature, sweat glands, and piloerector muscles (Jänig, 2006). The sympathetic chain, also known as the sympathetic trunk, comprises a group of interconnected paravertebral ganglia situated in the ventral side of the vertebral column and can be thought of as a distribution system for sympathetic activity that must span the body (Jänig, 2006). An image of the mouse sympathetic chain in situ and a diagram of general organization is presented in Figure 1.1. A more detailed description of SNS circuitry is described below.

1.2 **Anatomical organization**

1.2.1 *Gross anatomy*

The sympathetic chain is often depicted as an orderly group of ganglia, one per spinal segment, each approximately the same size and shape, innervated by rami communicantes originating

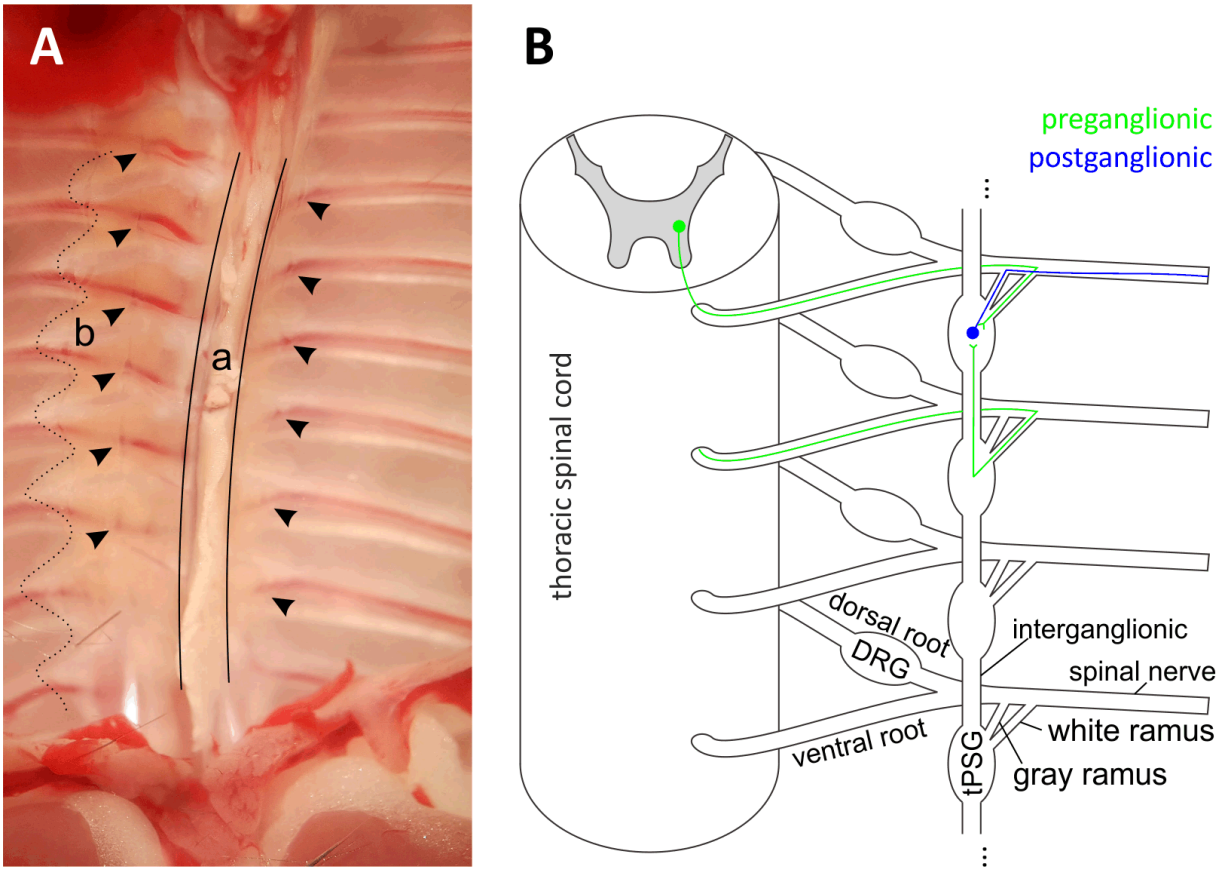

Figure 1.1 Anatomy
A, Ventral side of thoracic cavity. Arrowheads indicate thoracic ganglia. a, aorta covering spinal column. b, boundary between intercostal muscle and adherent brown adipose tissue. Ganglia indicated on the right side of the figure (animal's left side) are difficult to see at this angle. B, Schematic representation of basic organization of thoracic ganglia.

from the corresponding spinal nerve, with adjacent ganglia connected to each other by an interganglionic nerve (Standring, 2016). In truth, there exists considerable diversity in the gross anatomical morphology of the sympathetic chain. Much of the recent research on morphological diversity in sympathetic chains has been conducted in human cadavers with the purpose of improving surgical outcomes (Murata et al., 2003; Cho et al., 2005; Kommuru et al., 2014; Jain et al., 2016; Won et al., 2018).

All upper thoracic ganglia (T5 and above) are innervated by a ramus arising from the corresponding spinal nerve, while some are additionally innervated by a ramus arising from one segment rostral or caudal. The additional innervation is most common in T2 and becomes progressively less common in more caudal segments (Cho et al., 2005). Another cadaver study of thoracic chain notes considerable diversity in the presence or absence of the stellate ganglion, number of ganglia present, as well as the segmental origin of splanchnic nerves (Kommuru et al., 2014). A study of rat lumbar sympathetic trunk (LST) found that L1 and L4 varies little between subjects, but L2 and L3 exhibit considerable diversity in terms of ramus innervation (Miao et al., 1995).

We conducted our own anatomical study of thoracic chain ganglia, largely motivated by the difficulty of identifying separate ganglia once tissue was removed from the animal. In short, tissue was dissected and digested in collagenase (see Methods for more detailed procedure) and carefully exposed. The chains were observed under a dissecting microscope and the shape and location of sympathetic ganglia and interganglionic nerves were sketched by hand. Observations on rami were not feasible because of limitations related to time (chains were used in subsequent patch clamp recordings, so dissections needed to be fast) and equipment (dissecting scope was not always able to resolve fine processes). Figure 1.2 shows drawings made from several sympathetic chains from closely related mice of the same strain and genotype, most of whom were produced by the same breeding trio (same sire, one of two littermate dams). Immediately obvious from this figure is that the canonical view of sympathetic chain organization is overly simplistic. In general, the more rostral segments tend to obey the aforementioned scheme, with a single well-defined ganglion per segment, connected to its neighboring ganglia with a single

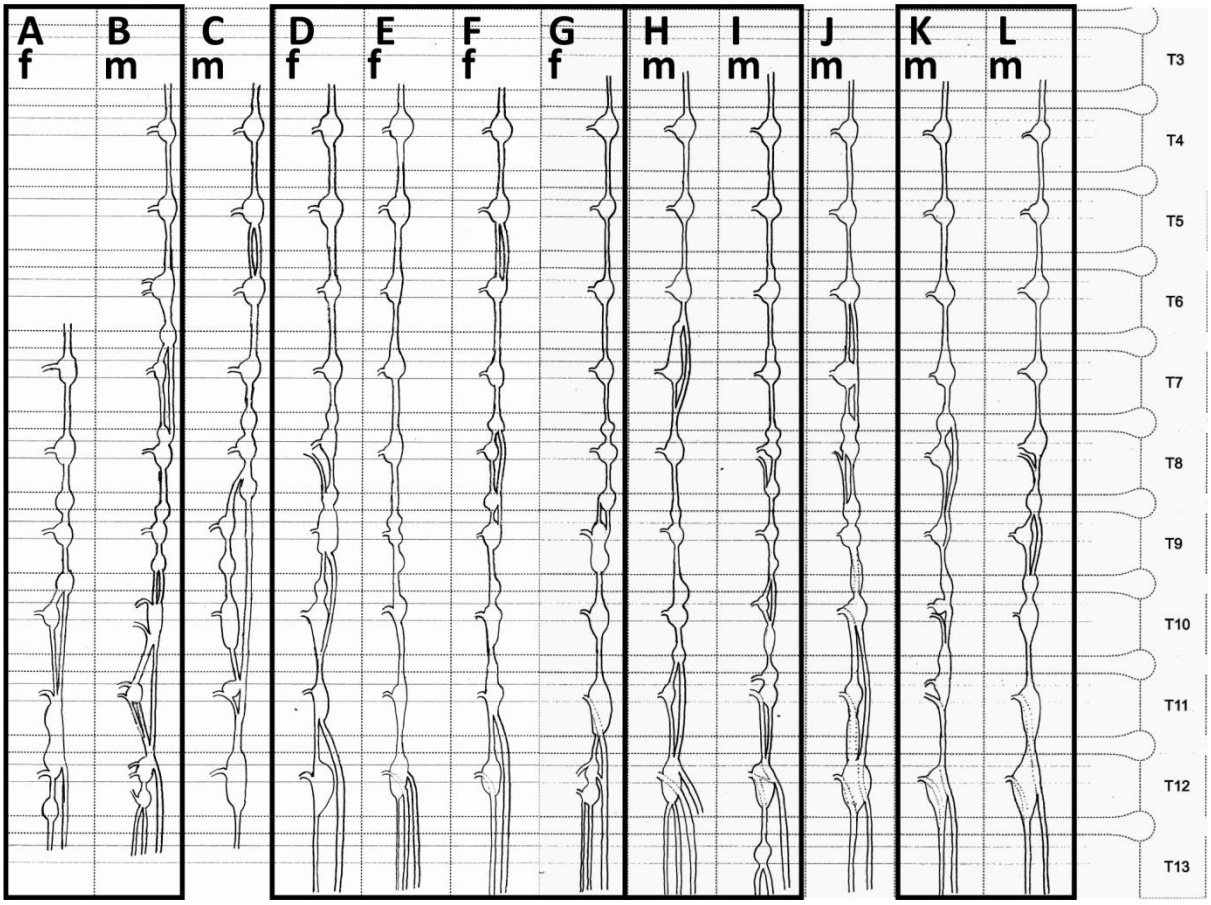

Figure 1.2 Anatomical diversity of sympathetic chains from related mice
All mice were ChAT-IRES-Cre::ChR2. Solid boxes indicate littermates. All but C had the same parents. Sex is indicated by m or f. The drawings were made *in situ* after collagenase treatment, but prior to removal of the tissue for recording (see McKinnon, et. al 2019 or Methods for more detail). Drawings are not to scale and chains were adjusted to line up for direct comparisons between segments and subjects. However, the shape and connections between ganglia are accurate.

interganglionic nerve. In the caudal portion of the chain, anatomical variability becomes more pronounced. Several segments were associated with multiple ganglia, or a single ganglion with multiple lobes. Often, the interganglionic nerve split into two, with one side occasionally skipping entire ganglia. T13 was absent in most but not all chains observed. It is possible that T13 tends to fuse with T12, which is often much larger than other ganglia. These observations do not appear to be sex-specific, as evidenced by the variability between littermates of the same sex.

1.2.2 *Cellular morphology*

The complexity of the dendritic arbor increases with animal size in mammalian SCG (Purves et al., 1986). The complexity of mouse tSPN dendritic arborizations is highly variable; some have no dendrites, others have five or more (Jobling and Gibbins, 1999). We undertook our own morphological characterization of postganglionic neurons in thoracic ganglia. We used a TH-CRE::TdTomato mouse in which a random subset of adrenergic postganglionic neurons is labeled, allowing visualization of dendritic arborizations. Confocal images of these sparsely labeled tSPNs from adult mice illustrate the morphological diversity of tSPNs (Figure 1.3A). Some tSPNs have relatively elaborate arborizations while others appear unipolar. This is similar to the results reported by Jobling and Gibbins. Postganglionic neurons have been shown to be either adrenergic or cholinergic (Jobling and Gibbins, 1999; Jänig, 2006). In order to assess neurotransmitter identity throughout the sympathetic chain, we used a choline-acetyltransferase (ChAT) transgenic mouse which fluorescently labels putative cholinergic postganglionic neurons (ChAT::eGFP), and co-immunolabelled tissue with an antibody to tyrosine hydroxylase (TH) to label putative adrenergic neurons. Neurons were counted from stellate (T1 and T2) to T13 ganglia. We found that TH^+ neurons comprised >97% of the population and no ganglion contained greater than 6% presumptive cholinergic neurons. This agrees with prior findings in rodent thoracic ganglia which found few cholinergic neurons (Schafer et al., 1998; Jobling and Gibbins, 1999; Masliukov and Timmermans, 2004; Schutz et al., 2015; see also Furlan et al., 2016). This indicates that cholinergic neurons in thoracic ganglia are rare. We therefore assume that a large majority of recorded cells were adrenergic.

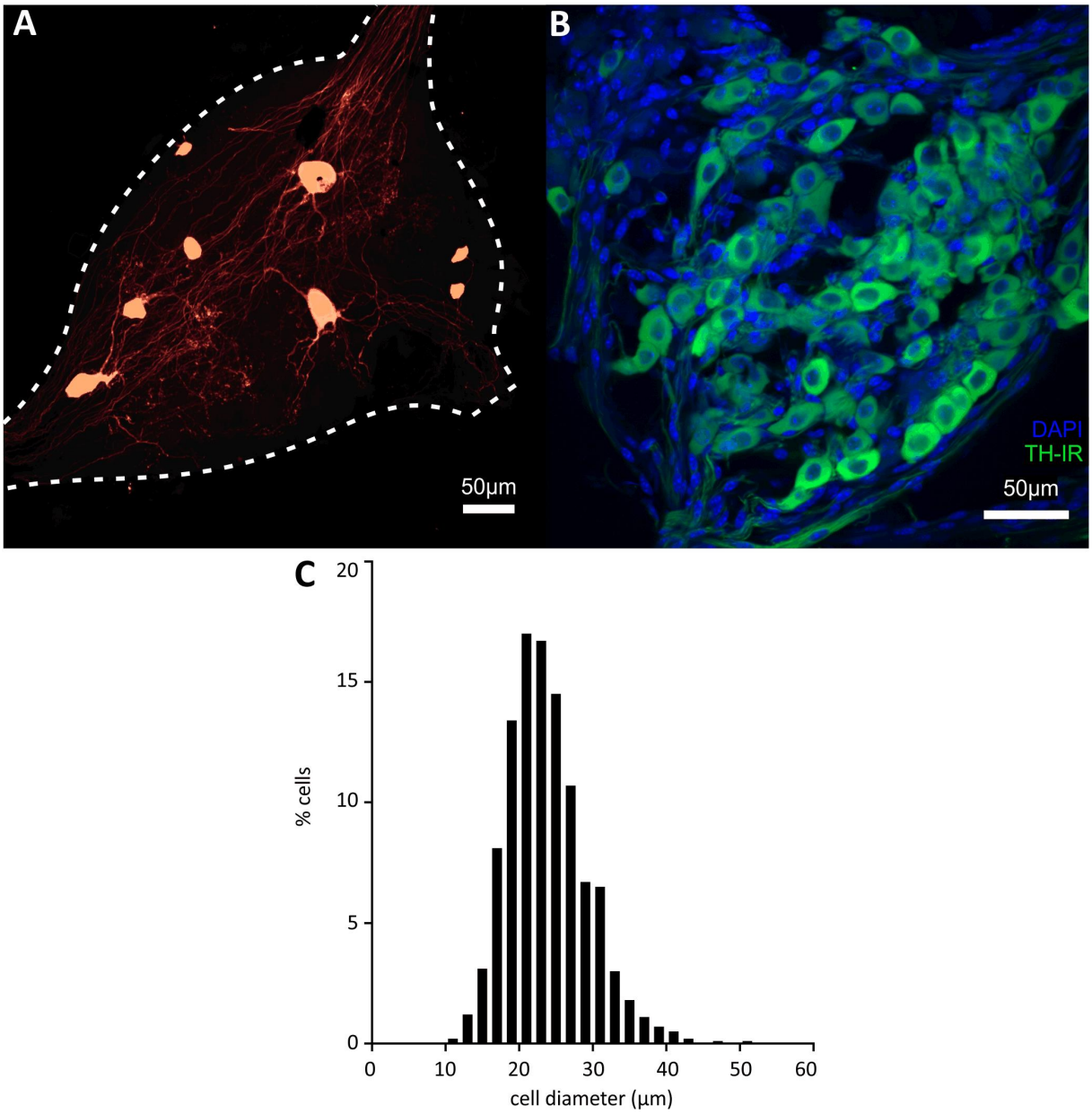

Figure 1.3 Cellular microanatomy
A, confocal image of sparsely-labelled TH^+ tSPNs in an adult mouse T5 ganglion. Dashed line denotes ganglion boundary. Note the morphological diversity of dendritic arborizations. Image taken by Camila Makhlouta. B, Confocal slice through whole-mounted tissue showing TH immunolabeling and nuclear labeling with DAPI. Note the numerous smaller and more intensely labeled nuclei that are presumably non-neuronal cells. Scale bar in A and B is 50µm. Image taken by Mi Hyun Choi. C, Histogram showing distribution of TH-IR cell diameters in T5 ganglia of 6 animals. Analysis performed by Meredith Lucy Galvin. All images and analysis were completed under the supervision of Alan Sokoloff.

Prior studies of adult mouse tSPNs in T4-T6 ganglia reported mean cell diameters of 31.0±1.2 μm (Jobling and Gibbins, 1999). As the majority of electrophysiological recordings focused on T5, diameter and number of TH-IR cells were examined in T5 ganglia in a separate sample from 6 adult mice (Figure 1.3B). The mean number of TH-IR neurons counted in T5 ganglia was 247 ± 127 (ranging from 106-418). tSPNs had a mean cell diameter of 23.8 ± 5.4μm. Cell size distribution is shown in Figure 1.3C. These values are smaller than those reported previously (Jobling and Gibbins, 1999). Differing methodology may explain this discrepancy. The aforementioned study measured the diameter of dye-filled cells after microelectrode impalement, which would preferentially target larger neurons (Brown, 1981).

1.3 **Circuitry**

The neural circuitry underlying the sympathetic nervous system is complex, and not fully understood. In general, various nuclei in the brain or brainstem integrate sensory information and then project to appropriate preganglionic neurons in the spinal cord. These preganglionic neurons project to postganglionic neurons in sympathetic ganglia, and postganglionic neurons innervate the appropriate effectors to bring about a physiologic response. This section will focus on the pathways underlying central control of blood pressure and body temperature, as these are the physiological variables that tSPNs help regulate. A graphical summary of this section is provided in Figure 1.4.

1.3.1 *Brain and brainstem nuclei*

Central control of blood pressure begins in the brainstem. The rostral ventrolateral medulla (RVLM) integrates signals from several other brainstem nuclei (CVLM, NTS) and provides

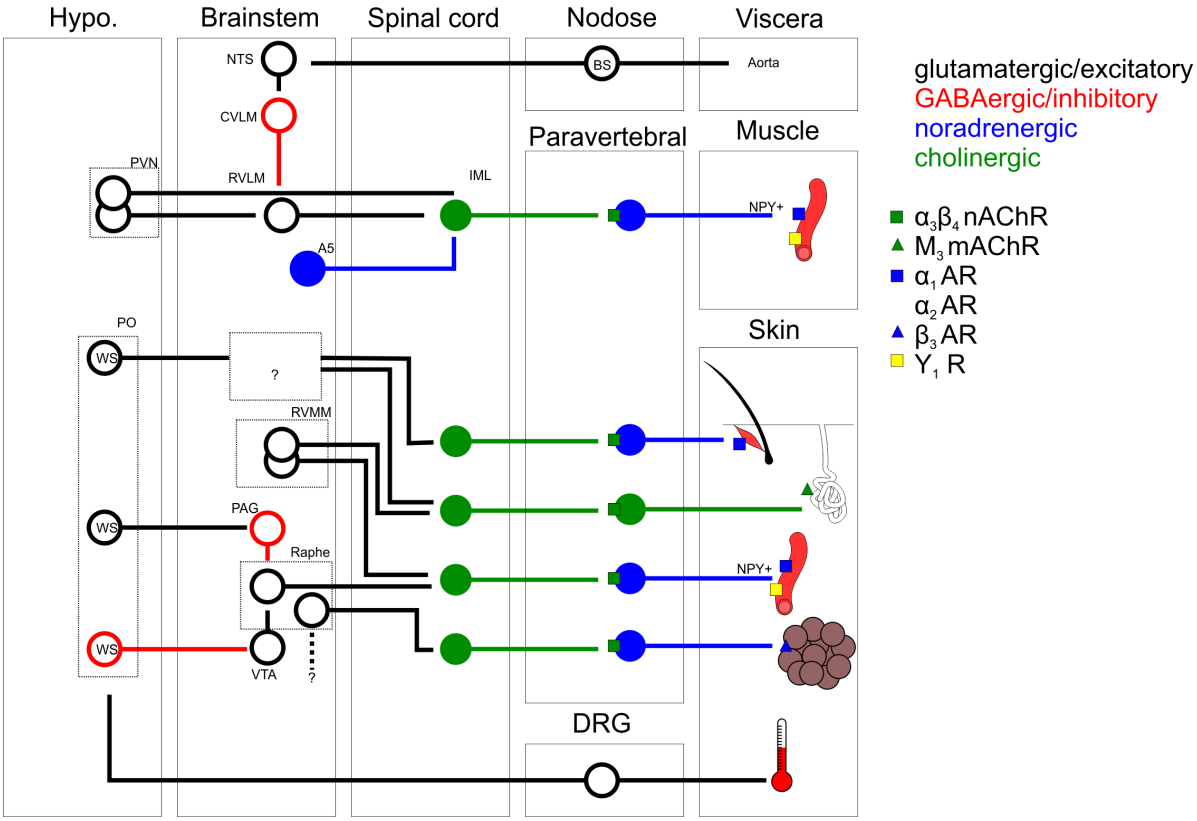

Figure 1.4 General organization of sympathetic nervous system circuitry
Schematic shows an overview of the interconnections within the sympathetic nervous system. Information was compiled and modified from Nagashima et. al. 2000; Guyenet, 2006; Shafton and McAllen 2013; A5, noradrenergic cell group; BS, barosensitive afferent; CVLM, caudal ventrolateral medulla; DRG, dorsal root ganglion; IML, intermediolateral cell column; NPY, neuropeptide Y; NTS, nucleus of the solitary tract; PAG, periaqueductal gray; PO, preoptic area of the hypothalamus; PVN, paraventricular nucleus of the hypothalamus; RVLM, rostral ventrolateral medulla; RVMM, rostral ventromedial medulla; VTA, ventral tegmental area; WS, warm sensitive neuron.

descending excitatory input (glutamatergic, with 70% of inputs also adrenergic) to sympathetic preganglionic neurons (Guyenet, 2006). Due to links between brainstem nuclei responsible for vasomotor and respiratory activity, vasoconstrictor activity tends to be linked to breathing and heart-rate (McLachlan, 2007). Central control of thermoregulation begins in the preoptic area of the hypothalamus (PO) (Nagashima et al., 2000). Thermosensitive neurons provide excitatory input to neurons in the periaqueductal gray (PAG), and inhibitory input to the ventral tegmental area (VTA). The PAG and VTA provide inhibitory and excitatory input, respectively, to the Raphe nuclei. The Raphe nuclei provide excitatory input to cutaneous vasoconstrictor

preganglionic neurons in the spinal cord (Nagashima et al., 2000), as well as brown adipose tissue (Deuchars and Lall, 2015). Specific inputs to sudo- and pilomotor preganglionic neurons arise from the hypothalamus as well (Tansey and Johnson, 2015; Hu et al., 2018).

1.3.2 *Preganglionic neurons*

Sympathetic preganglionics are located in thoracolumbar intermediolateral nucleus pars principalis (IML), the intermediolateral nucleus pars funicularis (IMLf), intercalated nucleus (IC), and the paraependymal intercalated nucleus (ICpe) between T1 and L2 (Deuchars and Lall, 2015). The majority of preganglionic neurons (75-80%) reside in the IML (Deuchars and Lall, 2015). Preganglionic neurons within the IML are arranged rostrocaudally in clusters of 20-150 neurons, with 100-500 um between adjacent clusters (Deuchars and Lall, 2015). There is a rostrocaudal organization of preganglionic neurons whereby neurons in the rostral IML project to rostral ganglia and caudal neurons project caudally. The levels overlap such that a horizontal slice through a spinal segment will contain preganglionic neurons projecting both rostrally and caudally. At a given segment, rostrally-projecting preganglionics are located in the dorsomedial IML and caudally-projecting preganglionics are more laterally located (Pyner and Coote, 1994; Deuchars and Lall, 2015). Preganglionics fire based on integrated input from many small excitatory and inhibitory inputs from brainstem and spinal interneurons (McLachlan, 2007; Deuchars and Lall, 2015). Vasoconstrictor preganglionics exhibit ongoing activity while sudomotor, pilomotor, and vasodilator preganglionics are silent in anaesthetized preparations (Janig and Szulczyk, 1980, 1981; Jänig, 1988). Preganglionic neurons project through ventral roots, typically within the same segment (Kuo et al., 1980; Deuchars and Lall, 2015). From the ventral root, preganglionic axons traverse the white ramus communicans to synapse onto

postganglionic neurons in sympathetic ganglia. The degree of myelination of preganglionic axons within white rami varies between species: the majority (60%) are myelinated in cat (Coggeshall and Galbraith, 1978), but few (<5%) are myelinated in the mouse and rat (Lewis and Burton, 1977; Gilbey et al., 1982; Serebryakova, 2008). All preganglionics are cholinergic and often express secondary transmitters associated with the function of their end effectors (Deuchars and Lall, 2015). These secondary transmitters include nitric oxide (NO), substance P (SP), vasoactive intestinal peptide (VIP), enkephalin, somatostatin, neurotensin, corticotrophin-releasing factor (CRF), Cocaine and amphetamine-regulated transcript peptide (CART), and luteinizing hormone-releasing hormone (LHRH) (Deuchars and Lall, 2015). CRF marks sudomotor preganglionics (Shafton et al., 1992) and CART preferentially marks vasoconstrictor preganglionics (Gonsalvez et al., 2010), but in general the function of a preganglionic neuron is difficult to identify with certainty based on neuropeptide markers (Deuchars and Lall, 2015).

1.3.3 *Postganglionic neurons*

The ratio of pre- to postganglionic neurons varies by species and tends to decrease with animal size (Purves et al., 1986). In rat SCG, the ratio is approximately 1:15 (Purves et al., 1986) while in humans it is closer to 1:200, indicating that a major function of postganglionic neurons is to amplify preganglionic signals (McLachlan, 2003). In mouse SCG, a single preganglionic neuron makes contact with ~64 postganglionic neurons, while in humans preganglionics contact around 4000 (Purves et al., 1986; McLachlan, 2003). The number of preganglionics that innervate a single postganglionic increase with animal size and range from 4-5 in mouse to 15 in rabbit to ~20 in humans (Purves et al., 1986; McLachlan, 2003). The number of synaptic inputs are approximately equal to the number of primary dendrites (Purves and Hume, 1981), and

microanatomical studies of mouse thoracic neurons report 6 primary dendrites on average (Jobling and Gibbins, 1999). Postganglionic neurons reside in either paravertebral ganglia (superior cervical ganglion, stellate/inferior cervical ganglion, thoracic, lumbar, sacral, ganglion impar) or prevertebral ganglia (coeliac ganglion, superior mesenteric ganglion, inferior mesenteric ganglion)(Jänig, 2006). Postganglionic neurons in paravertebral ganglia project through gray rami to their end organs (*e.g.* vasculature, arrector pili, sweat glands etc.) while postganglionic neurons in prevertebral ganglia innervate pelvic viscera (Jänig, 2006). Postganglionic neurons innervating vasculature of muscle and viscera are tonically active *in vivo* and are responsible for maintenance of blood pressure. They tend to be entrained to the cardiac cycle (Jänig, 1988). Postganglionic neurons innervating cutaneous vasculature are less likely to exhibit cardiac rhythmicity *in vivo* (Bini et al., 1981; Fagius et al., 1985; Jänig, 1988), and cutaneous vasomotor tone is maintained predominantly by circulating humoral factors rather than ongoing postganglionic activity (Willette et al., 1991). Cutaneous vasoconstriction, piloerection, and sweat secretion are primarily involved in thermoregulation. Cutaneous vasoconstriction reduces heat loss, piloerection increases thermal insulation in haired animals (e.g. mouse, rat, cat), and sweating leads to evaporative cooling in humans and horses (Jänig, 2006). In humans, pilomotor neurons are silent unless activated by a stimulus (*i.e*. hypothermia, strong emotional stimuli), and sudomotor neurons have little to no ongoing activity *in vivo* (Jänig, 2006).

1.3.4 *Effectors*

Postganglionic innervation leads to effects in end organ circuitry. Vasomotor postganglionics are adrenergic and cause vasoconstriction in vascular smooth muscle by activating α_1-adrenoceptors

(Jänig, 2006). The α_1-adrenoceptor is a G_q-protein coupled receptor which leads to vasoconstriction by activation of the IP_3 pathway (Docherty, 2010). Vasomotor postganglionics also release neuropeptide Y (NPY) (Elfvin et al., 1993). NPY activates the Y_1 receptor, a G_i-protein coupled receptor which leads to vasoconstriction via activation of the cAMP/PLC pathway (Hodges et al., 2009). NPY has independent vasoconstrictor activity of a similar degree to the adrenergic pathway (Hodges et al., 2009), and also has a synergistic effect with noradrenaline in setting vasomotor tone by reducing α_1-adrenoceptor desensitization (Wahlestedt et al., 1990; Hodges et al., 2009). Pilomotor postganglionics are also adrenergic and cause contraction of arrector pili by similarly activating α_1-adrenoceptors (Jänig, 2006). They do not express NPY (Gibbins, 1991). Sudomotor postganglionics are cholinergic and cause sweat secretion by activating M_3 mAChRs (Hu et al., 2018). Notably, sweat glands also contain adrenoceptors, primarily activated by circulating adrenaline and noradrenaline (Hu et al., 2018).

1.4 **Intrinsic properties of SPNs**

The electrical properties of sympathetic neurons have been studied in the SCG (Eccles, 1935; Erulkar and Woodward, 1968; Purves and Wigston, 1983; Li and Horn, 2006; Springer et al., 2015) and to a lesser extent the stellate and lumbar ganglia (Jänig, 1985; Cassell et al., 1986; Valli et al., 1989; Bratton et al., 2010), but to date only three studies have revealed electrophysiological properties of thoracic ganglia (Blackman and Purves, 1969; Lichtman et al., 1980; Jobling and Gibbins, 1999), which comprise the primary postganglionic innervation of vasculature, arrector pili, sweat glands, and brown adipose tissue. These studies all used microelectrode recordings, which have been shown to considerably alter passive and active properties of sympathetic neurons (Staley et al., 1992; Springer et al., 2015). As such, there is

currently very little known about the electrical properties of postganglionic neurons within the thoracic region of the sympathetic chain.

1.4.1 *Passive and firing properties*

A study using microelectrode recordings from mouse thoracic ganglia reported input resistance (R_{in}) of 118MΩ and a membrane time constant (τ_m) of 7.2ms (Jobling and Gibbins, 1999), and similar recordings in guinea pig report these values as 56MΩ and 9.1ms (Blackman and Purves, 1969). The same mouse study reported the R_{in} and τ_m of SCG neurons as 110 MΩ and 11.7ms, respectively, while another study (Springer et al., 2015) which used whole-cell recordings from intact rat SCG neurons reported R_{in} of 454MΩ. In this study, introduction of an artificial leak led to passive membrane property values closer in magnitude to microelectrode recordings, so the difference was attributed to the leak introduced by microelectrode recordings.

The aforementioned studies also disagree on the capacity for paravertebral neurons to fire repetitively. A prior study in guinea pig thoracic neurons reports tonic firing in response to sustained current injection (Blackman and Purves, 1969), while recordings in the mouse (Jobling and Gibbins, 1999) report that both SCG and thoracic neurons fire phasically, *i.e.* they fire few APs in response to sustained current injection. Phasic firing is believed to be the normal mode of operation for nearly all paravertebral neurons (Jänig, 1988), but these observations have typically relied upon microelectrode recordings. As before, a recent study proposed that the leak introduced by microelectrode recording alters firing properties of paravertebral neurons, and showed that when recorded using the whole-cell patch clamp technique, rat SCG neurons fire repetitively (Springer et al., 2015). They further showed that introduction of an artificial leak can

Study	Species	Technique	Ganglion	R_{in} (MΩ)	τ_m (ms)	Firing
Blackman and Purves, 1969	GP	ME	ThG	55.5	9.11	Tonic
Cassell et al., 1986	GP	ME	LSG	179	27.2	Phasic
Jobling and Gibbins, 1999	Mouse	ME	ThG	117.9	7.19	Phasic
"	"	"	SCG	109.7	11.7	Phasic
Springer et al., 2015	Rat	WC	SCG	454	38	Tonic
"		WC + leak	SCG	182	16	Phasic
McKinnon et al., 2019	Mouse	WC	ThG	1044	91.5	Tonic

Table 1.1 Prior reports of passive membrane properties of paravertebral neurons
GP, Guinea Pig; LSG, lumbar sympathetic ganglion; ME, microelectrode; SCG, superior cervical ganglion; ThG, thoracic ganglion; WC, whole-cell patch clamp.

cause repetitively firing neurons to fire phasically. In light of these vastly different observations, we undertook whole-cell recordings in mouse thoracic ganglia to determine, among other things, the basic and firing properties of thoracic postganglionic neurons. Table 1.1 provides a summary of these prior studies and the values of R_{in} and τ_m reported therein, alongside values from our own research (elaborated further in Chapter 2) for ease of comparison.

1.4.2 *Ion channels*

A-type K^+ current, M-type K^+ current, and H-current have been described in mouse thoracic neurons (Jobling and Gibbins, 1999). These currents as well as Ca^{2+}-dependent K^+ current, delayed rectifier K^+ current, and L-type Ca^{2+} current have also been described in rat SCG (Galvan and Sedlmeir, 1984; Sacchi et al., 1995; Rittenhouse and Zigmond, 1999). A recent RNA-seq study of thoracic neurons (Furlan et al., 2016) found RNA transcript expression of each of the aforementioned ion channels. Our computational model (See section 1.6) incorporated generalized models of these ion channels, but if RNA transcript levels could be

correlated with ion channel expression, future computational studies could be tailored to the specific molecular subtypes expressed in individual cells.

1.5 **Synaptic properties of SPNs**

1.5.1 *Types of synaptic input*

The primary method of transmission at sympathetic ganglia is fast nicotinic transmission from preganglionic axons. Langley was the first to note nicotine's ability to evoke responses in effectors when applied to sympathetic ganglia (Langley and Dickinson, 1889). The most common nicotinic receptor is the α3β4 subtype (Skok, 2002; Del Signore et al., 2004), though other receptor subunits (α3, α4, α5, α7, β3, β4) are present in autonomic ganglia (Skok, 2002). In thoracic ganglia, α3 and β4 are the most common based on RNA transcript count, with very low expression of α5, α7, and β2 (β3 was only expressed in glutamatergic neurons) (Furlan et al., 2016). EPSCs in sympathetic ganglia are driven by activation of α3β4 nicotinic receptors (Sargent, 2014). Postganglionic neurons may also have extrasynaptic α7 receptors (Sargent, 2014). EPSCs in rat SCG have a decay time constant in the range of 4-6ms (Hirst and McLachlan, 1984; Sacchi et al., 2006; Springer et al., 2015), and sometimes a second component was detected with a time constant of ~20ms (Kertser et al., 1998). In the lumbar sympathetic trunk, recruitment of fast-conducting preganglionic fibers is responsible for nicotinic receptor activation (Janig et al., 1984). There are no known fast inhibitory synapses in sympathetic ganglia (McLachlan, 2007). However, 'slow' metabotropic IPSPs and EPSPs following activation of muscarinic receptors have been described previously (Horn and Dodd, 1981; Cole and Shinnick-Gallagher, 1984; North, 1986). Intact paravertebral postganglionics are insensitive to purinergic transmission (Inokuchi and McLachlan, 1995), but they are known to release ATP

as a co-transmitter with either noradrenaline or acetylcholine onto smooth muscle effectors (Kennedy, 2015).

1.5.2 *Primary and secondary nicotinic synapses*

Most postganglionic neurons receive a single primary (or strong) synapse and few secondary (or weak) synapses, an organizational scheme termed the N+1 rule (Karila and Horn, 2000; McLachlan, 2007). Primary EPSPs are always suprathreshold and drive postganglionic firing, while secondary EPSPs are much smaller and were long thought to be ineffective at recruiting postganglionic cells. Secondary synapses have a lower quantal content than primary synapses (McLachlan, 1975). Secondary synapses are the first to appear during rat development, followed by primary synapses which appear gradually several weeks later (Hirst and McLachlan, 1984). A similar phenomenon is observed during re-innervation experiments; secondary synapses are the first to form after denervation of adult ganglia and primary synapses appear some time thereafter (McLachlan, 1974; Njå and Purves, 1977b; Njå and Purves, 1978). It is unclear if primary and secondary synapses represent functionally distinct classes of preganglionic neurons or the selective strengthening of one of several presynaptic inputs (Ireland, 1999; McLachlan, 2003; Bratton et al., 2010). Only secondary synapses express P-type calcium channels, but both types express R- and N-type calcium channels (Ireland et al., 1999; McLachlan, 2003). In guinea pig, less than 2% of cell surface area is dedicated to synaptic input, so the total number of synapses per neuron is low; the number of synapses is proportional to cell size and total dendritic length (Gibbins et al., 1998; Gibbins et al., 2000; Gibbins, 2013).

1.5.3 *Synaptic integration*

Secondary synapses are often viewed as inconsequential to cell recruitment, as their amplitude is not sufficient to recruit a postganglionic cell alone (McLachlan et al., 1998; Karila and Horn, 2000; McLachlan, 2003; Wheeler et al., 2004; Rimmer and Horn, 2010). The low firing rate of preganglionic neurons suggests that spatial or temporal summation of secondary inputs is very rare and does not contribute appreciably to postganglionic firing rate (McLachlan, 2003). However, a stimulus which drives preganglionic neurons at high frequency could elevate the importance of synaptic summation (McLachlan, 2003). In addition, synaptic facilitation of secondary synapses after repetitive stimulation at relatively low frequency (<0.5 Hz) has been observed (McLachlan, 1975). Also, repetitive stimulation of thin, slower-conducting fibers can lead to long-lasting enhancement of sympathetic activity in vasomotor but not sudomotor or pilomotor neurons (Janig et al., 1982; Blumberg and Janig, 1983), and this phenomenon is reliant on non-nicotinic and non-cholinergic mechanisms (Janig et al., 1984). Muscarinic activation may be due to spillover from highly active synapses (Eccles and Libet, 1961). These metabotropic mechanisms may enhance the efficacy of secondary synapses in recruiting postganglionic neurons and provide a means other than convergence by which preganglionic activity may be integrated over time (Janig et al., 1982).

1.6 **Computational modeling**

Biophysical models of excitable membranes come in many different varieties (De Schutter, 2010). The one most relevant to this dissertation is the family of conductance based modeling tools that descend ultimately from Hodgkin and Huxley's landmark squid giant axon experiments (Hodgkin and Huxley, 1952). In such a model, excitable membranes are modeled as

a capacitor in parallel with a number of transmembrane components that represent various ion channels. The original Hodgkin Huxley model included only three conductances: voltage-dependent sodium (g_{Na}), delayed-rectifier potassium (g_K), and a non-specific leak conductance (g_L) (Hodgkin and Huxley, 1952). This model may be extended by introducing additional parallel conductances, or by constructing a multi-compartment model which simulates more complex neuronal morphology (De Schutter, 2010). This section will focus on conductance based modeling of sympathetic paravertebral neurons.

1.6.1 *Intrinsic membrane properties*

Computational models of paravertebral neurons exist for rat SCG (Belluzzi and Sacchi, 1991; Sacchi et al., 1998) and bullfrog sympathetic B-neurons (Schobesberger et al., 2000; Wheeler et al., 2004). Both of these are single-compartment models, as rat and bullfrog sympathetic neurons are electrotonically compact (Belluzzi et al., 1985; Yamada et al., 1989). As with all Hodgkin Huxley type models, each of the previous models of sympathetic neurons include g_{Na}, g_K and g_L. The bullfrog models add a cyclic nucleotide-gated leak conductance (g_{CNG}) and an M-type potassium current conductance (g_M) (Schobesberger et al., 2000; Wheeler et al., 2004). The rodent model omits g_M and g_{CNG} and instead adds an A-type potassium conductance (g_A), a general calcium conductance (g_{Ca}), and two calcium-dependent potassium currents (g_{KCa}, g_{AHP}) (Belluzzi and Sacchi, 1991; Sacchi et al., 1998). The differences could be related to species, but may also reflect differences in motivation: Sacchi and colleagues were interested in modeling the action potential of rodent sympathetic neurons while the bullfrog models from Horn and colleagues were more concerned with synaptic interactions.

1.6.2 *Synaptic and network properties*

Modeling postganglionic recruitment relies on an accurate computational representation of fast nicotinic EPSCs. Several approaches to modeling EPSCs exist, which range from fairly simple template based models (Schobesberger et al., 2000; Roth and van Rossum, 2009) to more complex kinetic models (Edelstein et al., 1996). Horn and colleagues have advanced several computational models that support a role for secondary synapses in contributing to synaptic gain in both bullfrog and rat models (Karila and Horn, 2000; Wheeler et al., 2004; Horn and Kullmann, 2007; Springer et al., 2015). Such models indicate that the smaller EPSCs delivered by secondary synapses can recruit postganglionic neurons if the right conditions are met (e.g. high preganglionic firing rate, muscarinic enhancement, reduced leak, etc.).

1.7 **Effect of spinal cord injury on autonomic function**

As of 2018, there were approximately 300,000 people living with spinal cord injury in the United states (NSCISC, 2019). Spinal cord injury impairs normal autonomic function in addition to the more obvious sensory and motor deficits (Hou and Rabchevsky, 2014). Indeed, improving autonomic function after SCI is of greater importance to paraplegic patients than sensorimotor recovery (Anderson, 2004). This section focuses on the changes that occur in the sympathetic nervous system that modulates blood pressure after SCI, with specific emphasis on autonomic dysreflexia.

1.7.1 *Changes in cardiovascular function*

In the intact system, adrenergic input from C1 and serotonergic input from the caudal Raphe maintain sympathetic vasomotor tone (Madden and Morrison, 2006; Marina et al., 2006). Loss of

these inputs after SCI leads to chronic hypotension (Coote, 1990; Mathias, 2006; Hou and Rabchevsky, 2014) and spinal reflex circuitry comes to dominate the vasomotor pathway (Hou and Rabchevsky, 2014). In the acute phase after SCI, preganglionic neurons at the lesion site undergo cell death, demyelination, or cavitation (Tator, 1995). Below the lesion, preganglionic neurons undergo acute atrophy (Krassioukov and Weaver, 1995), but normal morphology is re-established gradually (Krassioukov and Weaver, 1996; Krassioukov et al., 1999; Llewellyn-Smith and Weaver, 2001). This reorganization likely results from spinal interneurons replacing lost brainstem connections (Weaver et al., 1997). These interneurons are ascending propriospinal neurons traveling within the dorsal gray commissure (Hou et al., 2008). The commissural neurons receive input from pelvic visceral afferents, which relay signals via unmyelinated c-fibers (Hou and Rabchevsky, 2014). After SCI, elevated levels of nerve growth factor (NGF) lead to sprouting of pelvic visceral afferents, as evidenced by an increase in the density of $CGRP^{+}$ afferent fibers in the lumbosacral spinal cord (Krenz and Weaver, 1998; Brown et al., 2004; Hou et al., 2009). Peripheral alpha-adrenoceptors become hyper-responsive to adrenaline after SCI (Hou and Rabchevsky, 2014). This phenomenon has been observed in humans and animals (Innes and Kosterlitz, 1954; Mathias et al., 1976; Rummery et al., 2010; Tripovic et al., 2010; Tripovic et al., 2011), but the mechanism by which this occurs is uncertain (Teasell et al., 2000). Some studies fail to report α-AR hyper-responsiveness in SCI animals, and attribute the enhanced sympathetic response to episodes of preganglionic hyperactivity (Osborn et al., 1989; Mallory, 1994).

1.7.2 *Autonomic dysreflexia*

Autonomic dysreflexia (AD) is an autonomic disorder characterized by a sudden hypertensive episode in response to a noxious stimulus caudal to a spinal lesion (Karlsson, 1999; Hou and Rabchevsky, 2014). AD afflicts the majority of patients with upper thoracic SCI (Karlsson, 1999; Hou and Rabchevsky, 2014). Typically, AD episodes present with headache, blurred vision, shivering, sweating, malaise, anxiety, and/or nausea, and in extreme cases can also result in seizure, stroke and intracerebral hemorrhage (Karlsson, 1999; Hou and Rabchevsky, 2014). Intracerebral hemorrhage may become an even greater problem in the future, given the aging population of SCI patients in the United States (Karlsson, 1999). Full expression of AD pathology requires loss of descending inhibitory input to visceral vasoconstrictors (Karlsson, 1999; Hou and Rabchevsky, 2014). As a result, AD is reported in the majority of SCI patients with a lesion at T6 or higher, but cases have been reported in patients with lesions as caudal as T10 (Karlsson, 1999; Hou and Rabchevsky, 2014). Symptoms are more severe if the lesion is complete or more rostral (Karlsson, 1999; Hou and Rabchevsky, 2014). Episodes are usually triggered by noxious stimuli originating below the level of the lesion (e.g. colon or bladder distention), but can also be triggered by benign stimuli (e.g. gentle stroking of the skin) (Hou and Rabchevsky, 2014). In the acute stage, AD can be brought on by the loss of descending bulbospinal modulation of preganglionic neurons (Hou and Rabchevsky, 2014). In the chronic phase, AD is maintained by NGF-mediated aberrant sprouting of $CGRP^{+}$ c-fiber afferents (Hou et al., 2009; Hou and Rabchevsky, 2014). These c-fibers form connections with propriospinal neurons within the dorsal gray commissure, which innervate preganglionic neurons (Hou et al., 2008; Hou and Rabchevsky, 2014). These two stages of reorganization correspond with the milder acute stage of AD and the more severe chronic stage (Hou and Rabchevsky, 2014).

1.8 **Summary and goals**

The sympathetic nervous system is partially responsible for homeostatic regulation of physiological parameters such as body temperature and blood pressure. It is essential that these variables are tightly regulated, but after high thoracic SCI, proper functioning of the SNS is compromised. Much of the information regarding the normal physiological function of paravertebral sympathetic neurons has been inferred from recordings in the SCG or lumbar ganglia. However, there is a notable gap in our understanding of neurons within the thoracic portion of the sympathetic chain. In addition, the majority of electrophysiological recordings of sympathetic neurons have relied on microelectrode recordings which can alter the properties of postganglionic neurons. We therefore acquired whole-cell recordings from mouse thoracic paravertebral neurons in order to address this gap in knowledge. We also present an analysis of the effect SCI has on intrinsic and synaptic properties of thoracic neurons as few studies of SCI have focused on paravertebral ganglia.

This dissertation began with an overview of the pertinent literature. Hereafter, I present original research on the intrinsic membrane properties of thoracic neurons as well as a comparison of their properties after SCI [Chapter 2]. I then present an analysis of synaptic input to thoracic neurons along with evidence of injury-induced synaptic reorganization [Chapter 3]. Finally, I conclude with a general summary of findings and a series of unanswered questions raised during the course of this project [Chapter 4]. There is significant overlap in methodology between Chapters 2 and 3, so a detailed methods section which applies to both is provided at the end [Chapter 5]. Through this dissertation, I aim to show that thoracic postganglionic neurons are

more than simple relay stations for central sympathetic commands; rather, they are actively involved in integration and amplification of preganglionic input. Furthermore, they are potentially the site of injury-induced reorganization following spinal cord injury.

2 Intrinsic membrane properties of thoracic postganglionic neurons

This chapter was adapted in part from work published in eNeuro (McKinnon et al., 2019).

2.1 **Abstract**

Thoracic paravertebral sympathetic chain postganglionic neurons (tSPNs) comprise the final integrative output of the distributed sympathetic nervous system controlling vascular and thermoregulatory systems. Considered a non-integrating relay, what little is known of tSPN intrinsic excitability has been determined by sharp microelectrodes with presumed impalement injury. We thus undertook the first electrophysiological characterization of tSPN cellular properties using whole-cell recordings and coupled results with a conductance-based model to explore the principles governing their excitability in adult mice of both sexes.

Recorded membrane resistance and time constant values were an order of magnitude greater than values previously obtained, leading to a demonstrable capacity for synaptic integration in driving recruitment. Variation in membrane resistivity was the primary determinant controlling cell excitability with vastly lower currents required for tSPN recruitment. Unlike previous microelectrode recordings in mouse which observed inability to sustain firing, all tSPNs were capable of repetitive firing. Computational modeling demonstrated that observed differences are explained by introduction of a microelectrode impalement injury conductance. Overall, tSPNs largely linearly encoded injected current magnitudes over a broad frequency range with distinct subpopulations differentiable based on repetitive firing signatures.

Thus, whole-cell recordings reveal tSPNs have more dramatically amplified excitability than previously thought, with greater intrinsic capacity for synaptic integration and with the ability for

maintained firing to support sustained actions on vasomotor tone and thermoregulatory function. Rather than acting as a relay, these studies support a more responsive role and possible intrinsic capacity for tSPNs to drive sympathetic autonomic function.

2.2 **Significance**

Thoracic sympathetic postganglionic neurons (tSPNs) represent the final neural output for control of vasomotor and thermoregulatory function. We used whole-cell-recordings and computational modeling to provide broad insight on intrinsic cellular mechanisms controlling excitability and capacity for synaptic integration. Compared to past intracellular recordings using microelectrode impalement, we observed dramatically higher membrane resistivity with primacy in controlling enhanced tSPN excitability and recruitment via synaptic integration. Compared to reported phasic firing, all tSPNs fire repetitively and linearly encode injected current magnitude to firing frequency over a broad range. Modeling studies suggest microelectrode impalement injury accounts for differences in tSPN properties previously observed. Overall, intrinsic tSPN excitability plays a much greater role in the integration and maintenance of sympathetic output than previously thought.

2.3 **Introduction**

Sympathetic postganglionic neurons within paravertebral chain ganglia (SPNs) represent a large fraction of the final output of the sympathetic nervous system. Whereas prevertebral sympathetic ganglia are typically associated with one or more visceral organs in a discrete location (celiac ganglion, superior/inferior mesenteric ganglion), thoracic paravertebral chain ganglia are associated with control of dispersed tissue systems such as vasculature, brown adipose tissue,

sweat glands, and piloerector muscles (Jänig, 2006; Bartness et al., 2010). As such, the sympathetic chain can be thought of as a distribution system for sympathetic activity that spans the body. The vast majority of paravertebral postganglionic neurons in mice are adrenergic (Gibbins, 1991; Jobling and Gibbins, 1999) since sweat glands, innervated by cholinergic postganglionic neurons, are largely absent in the mouse (Lu and Fuchs, 2014).

Traditionally, thoracic sympathetic postganglionic neurons (tSPNs) have been envisioned as passive followers of intraspinal preganglionic neuronal activity. By this viewpoint, postganglionic neurons fire if and only if preganglionics fire and serve as 1:1 relays that pass central commands to the periphery (Jänig, 2006). This relationship is explained by the "n+1" rule, wherein postganglionic neurons receive n small synaptic inputs, and one major, always suprathreshold input which leads to firing with a high safety factor. The n smaller synaptic inputs are typically sub-threshold and infrequent, and are not thought to contribute appreciably to the firing rate (McLachlan et al., 1998; Karila and Horn, 2000; McLachlan, 2003; Wheeler et al., 2004; Rimmer and Horn, 2010). However, recent evidence from rodent sympathetic ganglia has shown that postganglionic neurons play a more active role in shaping sympathetic output (Bratton et al., 2010; Springer et al., 2015). In light of these findings, we must reconsider the role that sympathetic postganglionic neurons play in synaptic integration and signal transmission.

Despite their critical importance as the final output controlling sympathetic neural commands, surprisingly little is known about the SPNs in thoracic segments (tSPNs) of the sympathetic chain. The most likely reason for this is their near inaccessibility to in vivo study, and the relative difficulty for in vitro cellular characterization. Because of this difficulty,

electrophysiological properties of sympathetic neurons have been largely inferred from recordings in other mammalian paravertebral sympathetic ganglia, namely the superior cervical ganglion (SCG) (Eccles, 1935; Erulkar and Woodward, 1968; Purves and Wigston, 1983; Li and Horn, 2006) and to a lesser extent the stellate and lumbar ganglia (Jänig, 1985; Cassell et al., 1986; Valli et al., 1989; Bratton et al., 2010). Compared to SCG, mouse tSPNs are smaller, have less elaborate dendritic arbors, are likely more excitable, and differ in measures of action potential shape (Jobling and Gibbins, 1999). Thoracic ganglia also contain a different subset of molecularly distinct SPN subpopulations and project to different end-organs (Jänig, 2006; Furlan et al., 2016). Unfortunately, few studies have directly characterized electrophysiological properties of thoracic ganglia (Blackman and Purves, 1969; Lichtman et al., 1980; Jobling and Gibbins, 1999). These studies used sharp microelectrodes for recordings, which likely introduce a considerable impalement injury conductance compared to whole-cell patch clamp recordings (Staley et al., 1992; Springer et al., 2015). This injury-induced conductance alters basic membrane properties, such as input resistance and membrane time constant, which reduce recruitment and synaptic integrative actions according to classical cable theory (Rall, 2011; Springer et al., 2015). The impalement conductance introduced by microelectrode recordings can also prevent expression of repetitive firing properties (Cymbalyuk et al., 2002; Springer et al., 2015). Indeed, while it is generally thought that most paravertebral SPNs fire phasically (Cassell et al., 1986; Jobling and Gibbins, 1999; Li and Horn, 2006), whole-cell recordings in SCG support repetitive rather than phasic firing (Springer et al., 2015). Whether repetitive firing properties are predominant in tSPNs remains unknown.

The aim of the present study is to investigate the electrophysiological properties of tSPNs using whole cell recordings to more accurately characterize the cellular mechanisms that drive and modulate excitability of tSPNs. We furthermore matched recordings to a computational model to better understand how synaptic inputs and passive and active membrane properties interact to recruit neurons and generate the firing properties observed.

2.4 **Results**

2.4.1 *Passive membrane properties*

Whole cell patch clamp recordings were acquired from 35 tSPNs obtained from 30 adult mice. Basic cellular properties are summarized in Table 2.2. The distribution of resting membrane potential is shown in Figure 2.1A. Input resistance (R_{in}) and membrane time constant (τ_m) were, on average, an order of magnitude higher than values recorded using microelectrode recordings in mouse (Jobling and Gibbins, 1999) and guinea pig (Blackman and Purves, 1969) thoracic ganglia. R_{in} was strongly correlated with τ_m (Figure 2.1B), but not cell capacitance (C_m), an estimate of cell size. This indicates that membrane resistivity, but not cell size, is primarily responsible for the variability seen in resistance measures (Gustafsson and Pinter, 1984). C_m was also moderately correlated with τ_m. A summary of correlation parameters is provided in Table 2.3.

One impact of larger τ_m is longer duration spontaneous EPSPs (sEPSPs) and consequently greater capacity for temporal summation. Spontaneous synaptic activity is often observed in whole-cell recordings, including instances of sEPSP summation that lead to recruitment of action

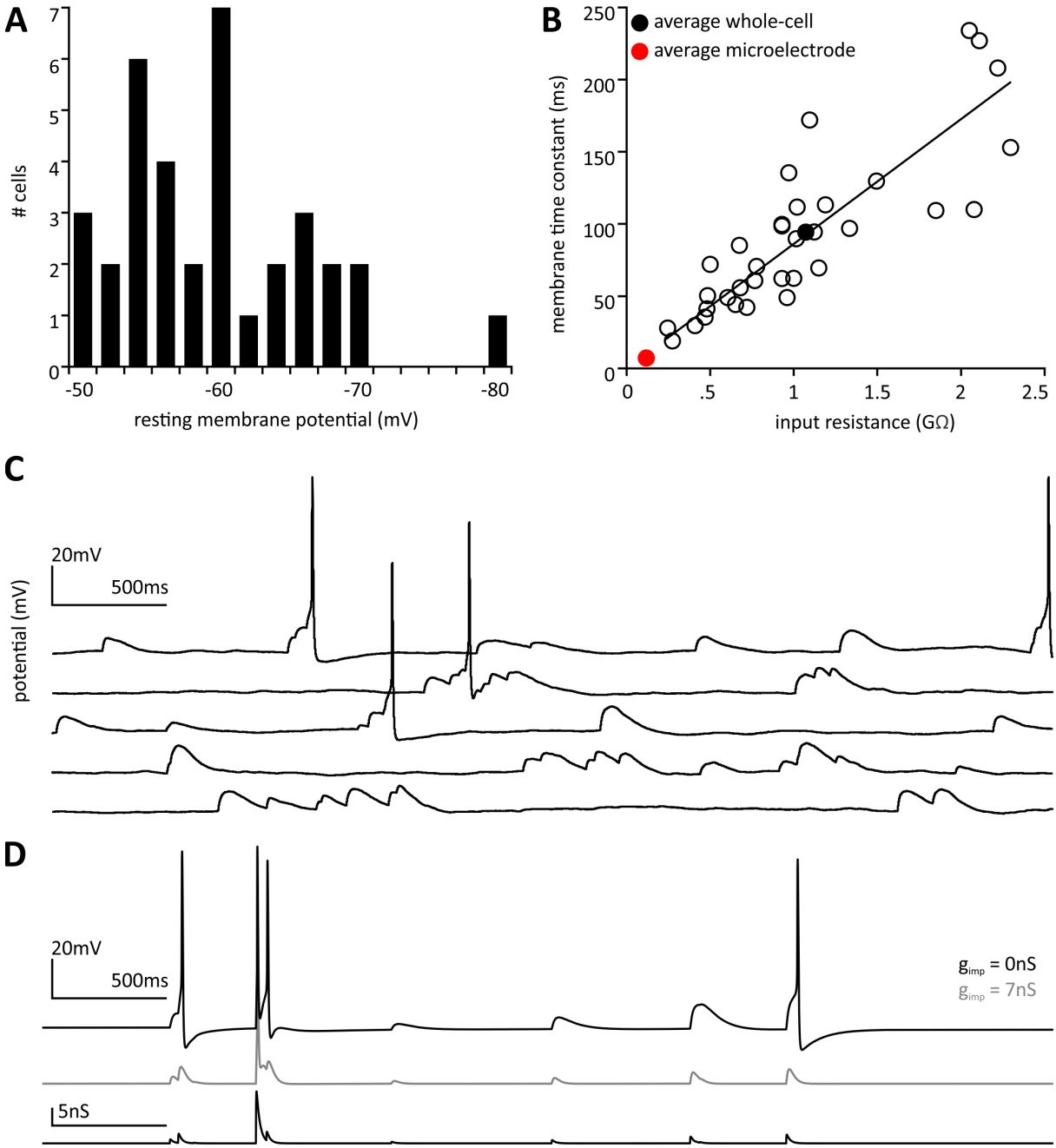

Figure 2.1 Passive membrane properties

A, Histogram showing distribution of resting membrane potential values. B, Input resistance is highly correlated with membrane time constant. Solid line indicates linear least-squares fit. Filled black circle represents population mean. Red filled circle, population mean from (Jobling and Gibbins, 1999). C, Example of synaptic summation leading to action potential recruitment in a particularly active recording. Shown is a raster of epochs of spontaneous synaptic activity. Cell resting membrane potential was −60 mV. In this neuron a τ_m of 109 ms led to comparably long EPSP membrane voltage decay time constants. Vertical scale bar is 20mV; horizontal scale bar is 500ms. D, Top, model neuron subjected to simulated synaptic input fires in response to synaptic summation. Middle, if an impalement conductance is added, synaptic summation is no longer effective. Bottom, simulated g_{syn} used to generate voltage traces. Horizontal scale bar is 500ms; vertical scale bars are 20mV and 5nS, respectively.

potentials (Figure 2.1C). In this neuron a τ_m of 109 ms led to comparably long sEPSP membrane voltage decay time constant. To explore the impact of preserved passive membrane properties on synaptic summation, we implemented a synaptic conductance in the computational model. A template conductance was constructed with Poisson-distributed events whose amplitudes and mean frequency match values from whole-cell voltage clamp recordings. This template conductance was used to stimulate a standard model neuron (Figure 2.1D, top trace) and a model neuron with simulated microelectrode impalement injury (middle trace). In the intact cell, synaptic events are larger in amplitude and synaptic summation can lead to cell recruitment. In the model neuron with simulated impalement, AP recruitment was observed only in response to the largest single synaptic event.

2.4.2 *Rheobase*

The current required to depolarize a cell from its holding potential to firing threshold (rheobase) was examined in 35 cells by injecting long duration (1.5-3s) pulses through patch electrodes. In order to control for the possible influence of a variable resting membrane potential on rheobase, tonic bias current was injected to hold cells at approximately −70mV prior to rheobase estimation. Fluctuations in membrane voltage made it difficult to precisely set holding potential prior to injected current steps, and values ranged from −56 to −83 mV. We compared actual holding voltage against rheobase to determine if this variability altered rheobase estimation. Rheobase was not correlated with holding potential.

Voltage threshold was assessed at minimal suprathreshold current intensity. Assuming cell depolarization is governed by Ohmic or non-rectifying processes, the ratio of relative voltage

threshold to input resistance would predict rheobase (Gustafsson and Pinter, 1984). Indeed, measured and calculated rheobase are well correlated (Figure 2.2A, Table 2.3) and approximately equal, indicating that rectifying currents do not play a major role in determining rheobase for the population. However, deviation of calculated rheobase values above and below those predicted by Ohmic processes support a role for voltage-dependent conductances (Gustafsson and Pinter 1984). Values of measured and calculated rheobase are presented in Table 2.2. As calculated rheobase provides a more precise index of excitability, further analysis focuses on this parameter.

Calculated rheobase current was strongly correlated with input conductance, $g_{in}=R_{in}^{-1}$ (Figure 2.2B), and moderately correlated with the inverse of time constant, τ_m^{-1}, but was uncorrelated with capacitance. A summary of correlation parameters is provided in Table 2.3.

We further investigated the relationship between input conductance and rheobase in a model cell. We adjusted g_{leak} in order to vary input conductance of a model neuron over most of the range observed in recorded neurons (0.5 to 3nS). Bias current was adjusted to hold the model cell at −70mV. The rheobase was then calculated for each value of input conductance by using a binary search algorithm to find the minimal injected current which produces a spike (Figure 2.2B, gray line). The results show that there is a deterministic relationship between rheobase and input conductance that can help to explain some of the correlation observed in recorded neurons. However, given the variability of rheobase measures in recorded cells with comparable values for input conductance, it is clear that input conductance alone does not fully explain the range of rheobase values observed in recorded neurons.

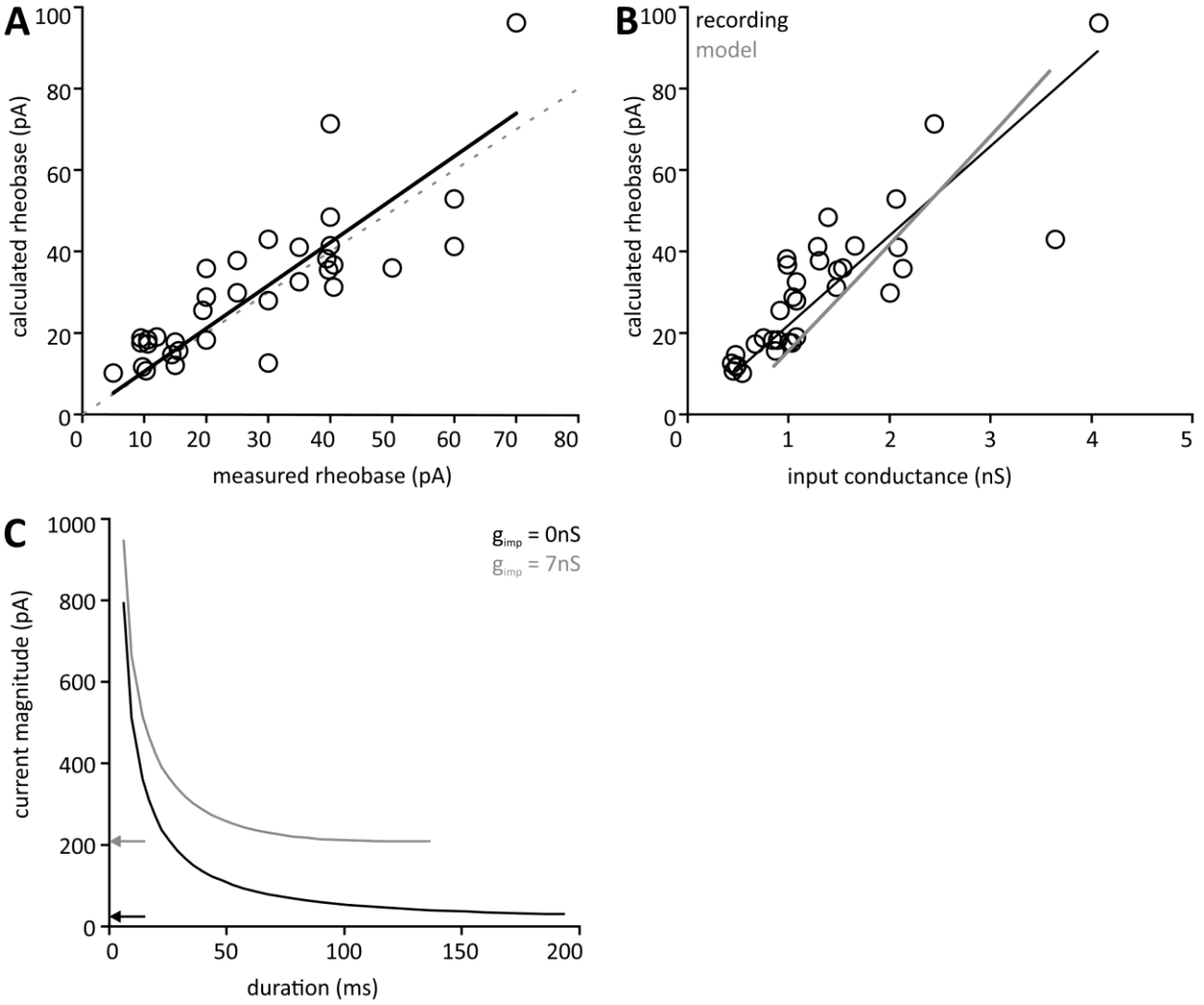

Figure 2.2 Factors affecting rheobase
A, There is a strong correlation between measured rheobase and calculated rheobase and the two values are approximately equal. This suggests that rheobase is predominantly governed by Ohmic phenomena. Dashed line is line of identity. B, Calculated rheobase was well correlated with input conductance in recorded neurons, open circles. Gray line represents the rheobase versus input conductance relationship for a single model neuron chosen to fit experimental data. Standard model cell with G_M=20nS and G_A=15nS. In A and B, solid line represents least squares regression. C, Strength-duration curves for model neurons. Black, standard model cell with no impalement conductance. Black arrow indicates rheobase. Gray, standard cell with gimp = 7nS, comparable to a microelectrode recording. Gray arrow indicates much higher rheobase for impaled cell.

Rheobase values were 80-90% lower than values estimated in tSPNs previously with microelectrode recordings in both mouse and guinea pig (Blackman and Purves, 1969; Jobling and Gibbins, 1999). Reduced rheobase values indicate that tSPNs are much more excitable than previously considered. To more fully explore the influence of microelectrode impalement on cell

excitability, we constructed strength-duration curves for model cells. In a standard model cell, the strength-duration curve follows a characteristic inverse curve. After implementation of an impalement conductance consistent with a microelectrode recording, rheobase is increased about 8-fold (Figure 2.2C). This is consistent with the discrepancy between our experimental findings and the aforementioned studies using microelectrodes.

2.4.3 *Repetitive Firing*

Increasing current steps were delivered to assess repetitive firing properties from a holding potential of approximately −70mV. All cells (n=35) were capable of repetitive firing in response to sustained current injection. This contradicts an earlier report that tSPNs fire phasically in response to depolarization (Jobling and Gibbins, 1999). Figure 2.3A shows an example of a recorded cell which fires repetitively at progressively higher frequency in response to increasing depolarizing current steps (top). A model neuron that used known voltage-dependent conductances for paravertebral sympathetic neurons and incorporated values for input conductance obtained from our whole-cell recordings was able to replicate repetitive firing (Figure 2.3A, bottom). Frequency-current (f-I) relations were obtained by plotting the maximal (initial) and sustained firing rate versus injected current magnitude. Figure 2.3Bi and Bii show the maximal and sustained (respectively) f-I curves for all cells. Maximal instantaneous firing rate did not exceed 28 Hz, while sustained firing rate did not exceed 17 Hz for the highest steps given. f-I curves were approximately linear. In order to determine the role that input conductance plays in determining f-I relations in tSPNs, we selected a model neuron that matches the experimental f-I curves and then systematically changed input conductance by varying g_{leak} from 0 to 3nS. Of note, varying input conductance also changes holding potential so

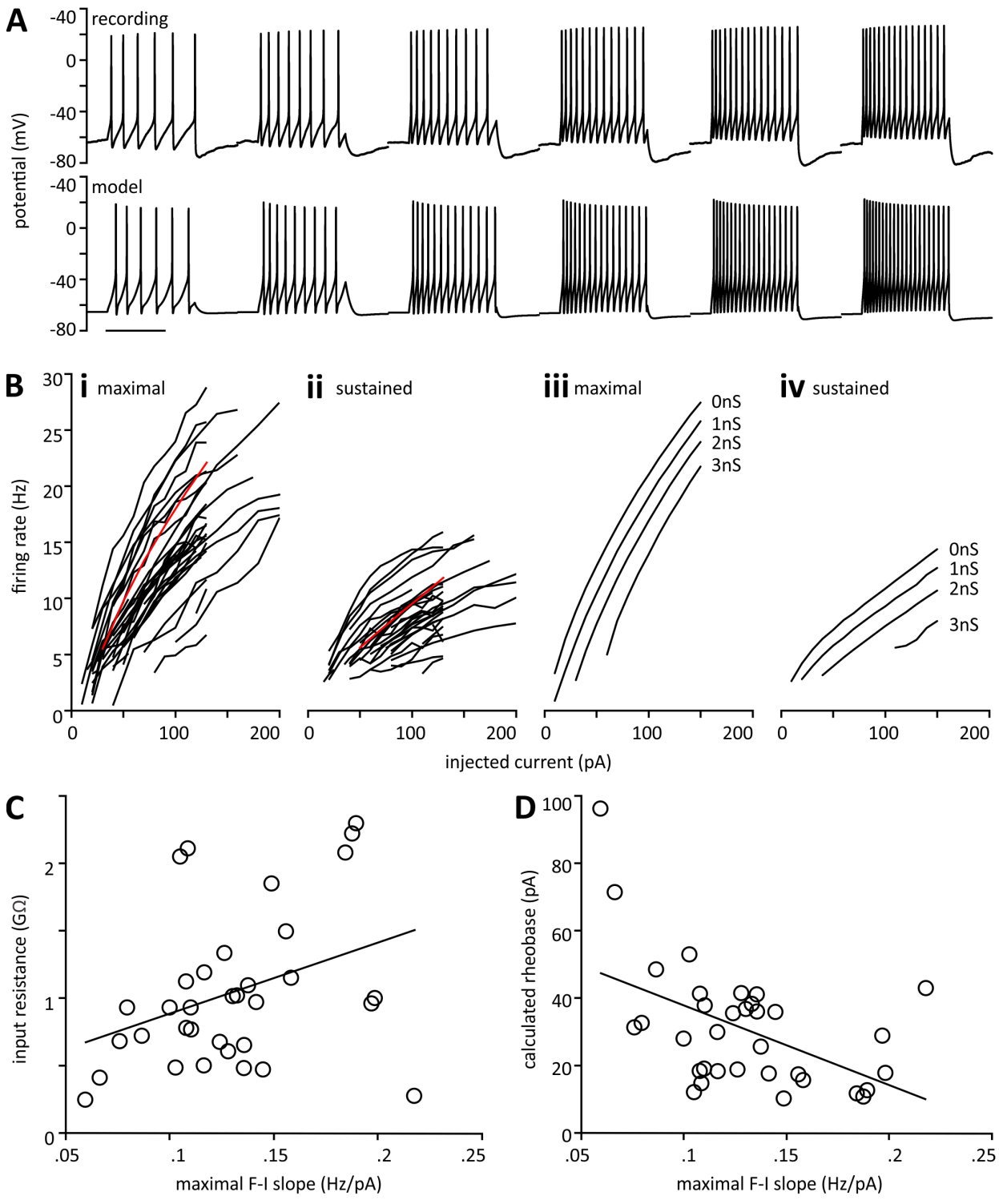
A
recording
model
potential (mV)
-40
0
-40
-80
-40
0
-40
-80
B
i maximal
ii sustained
iii maximal
iv sustained
0nS
1nS
2nS
3nS
0nS
1nS
2nS
3nS
firing rate (Hz)
30
25
20
15
10
5
0
0
100
200
injected current (pA)
C
input resistance (GΩ)
2
1
0
.05
.1
.15
.2
.25
maximal F-I slope (Hz/pA)
D
calculated rheobase (pA)
100
80
60
40
20
0
.05
.1
.15
.2
.25
maximal F-I slope (Hz/pA)

Figure 2.3 tSPNs exhibit repetitive firing.
A, Top, representative trace from a tSPN showing increases in repetitive firing frequency in response to increasing current steps. Bottom, model neuron also showing repetitive firing. Standard model with G_M=30, G_{KCa}=70, G_A=80, G_{leak}=2nS. Injected current from left to right in both recorded neuron and model is 30, 50, 70, 90, 110, 130pA. Scale bar is 1s. B, *f*-I relations for recorded and model neurons. (i) maximal instantaneous firing rate is plotted versus injected current for all cells. (ii), same as Ci with sustained firing rate. Red line in i and ii is maximal and sustained *f*-I curve from model neuron in A. (iii) maximal *f*-I curve from a model neuron in which gleak was adjusted from 0 to 3nS. Note: as varying input conductance also changes holding potential, each model neuron was subjected to a different holding current to hold the initial voltage at -70mV. Also note that g_{leak} is distinct from g_{imp}. (iv) corresponding sustained *f*-I curves. Model parameters other than gleak are the same as in A. C, Maximal *f*-I slope is positively correlated with input resistance. D, Maximal *f*-I slope is negatively correlated with calculated rheobase.

in order to remain consistent with experimental protocol, each model neuron was subjected to a different holding current to hold the initial voltage at −70mV. Figure 2.3Biii and Biv demonstrates that altering g_{leak} can shift the *f*-I curve, but it does not appear to change the *f*-I slope. Thus, input conductance cannot fully account for the range of *f*-I curves observed. To determine if other model parameters are capable of changing *f*-I slope, we systematically varied each parameter and observed its influence on maximal and sustained *f*-I curves. Most notably, C_m appears to influence the slope of the maximal *f*-I curve while G_{CaL} and G_{KCa} impact the slope of the sustained *f*-I curve. Other model parameters (G_{Na}, G_K, G_M, G_A, G_{leak}) are able to shift *f*-I curves without significantly altering slope. Thus, we are able to match any realistic *f*-I curve by adjusting model parameters, which implies that a host of intrinsic cellular properties are responsible for the range of *f*-I curves we observed.

Slope for both maximal and sustained *f*-I curves was calculated as a measure of excitability (Zimmerman and Hochman, 2010). In short, a cell with a higher *f*-I slope would respond to an incremental change in current with a higher change in firing frequency. In this way, *f*-I slope can be thought of as the gain between input and output of a neuron. Values for maximal and sustained *f*-I slope are given in Table 2.2.

We assessed the role of variations in R_{in} and rheobase in cell excitability based on *f*-I slope measures. Maximal firing rate at 100pA current injection was significantly correlated with R_{in}. Maximal *f*-I slope was moderately correlated with R_{in} (Figure 2.3C), and moderately and negatively correlated with calculated rheobase (Figure 2.3D). No such relationship was found for τ_m or C_m. A summary of correlation parameters is provided in Table 2.3. Cells with lower rheobase and higher R_{in} had higher *f*-I slopes, suggesting that Ohmic properties contribute to the frequency-current response.

2.4.4 *Impalement simulation*

The discrepancy between observations of phasic and repetitive firing likely arises as a result of leak introduced by microelectrode impalement (Springer et al., 2015). We undertook additional modeling to test whether an impalement injury can convert repetitive to phasic firing. An additional impalement conductance, g_{imp}, was added to a standard model cell. Reversal potential of g_{imp} was set at −15mV (see Methods). We explored the relationship between g_{imp} and firing type over a range of conductance and current injection combinations (Figure 2.4). For a given set of g_{imp} and injected current, a model cell was characterized as non-firing (N), phasic firing (P), or repetitively firing (R). Setting g_{imp} to 7nS results in an input resistance of ~100MΩ, the mean value of input resistance reported by Jobling and Gibbins (1999). With this level of microelectrode leak, non-firing was observed in response to subthreshold current injection (Figure 2.4Ai), and phasic firing was observed in response to suprathreshold current injection over the range of current values tested by Jobling and Gibbins (Figure 2.4Aii). However, when g_{imp} was set at 0nS, analogous to a whole-cell recording, repetitive firing was observed instead (Figure 2.4Aiii).

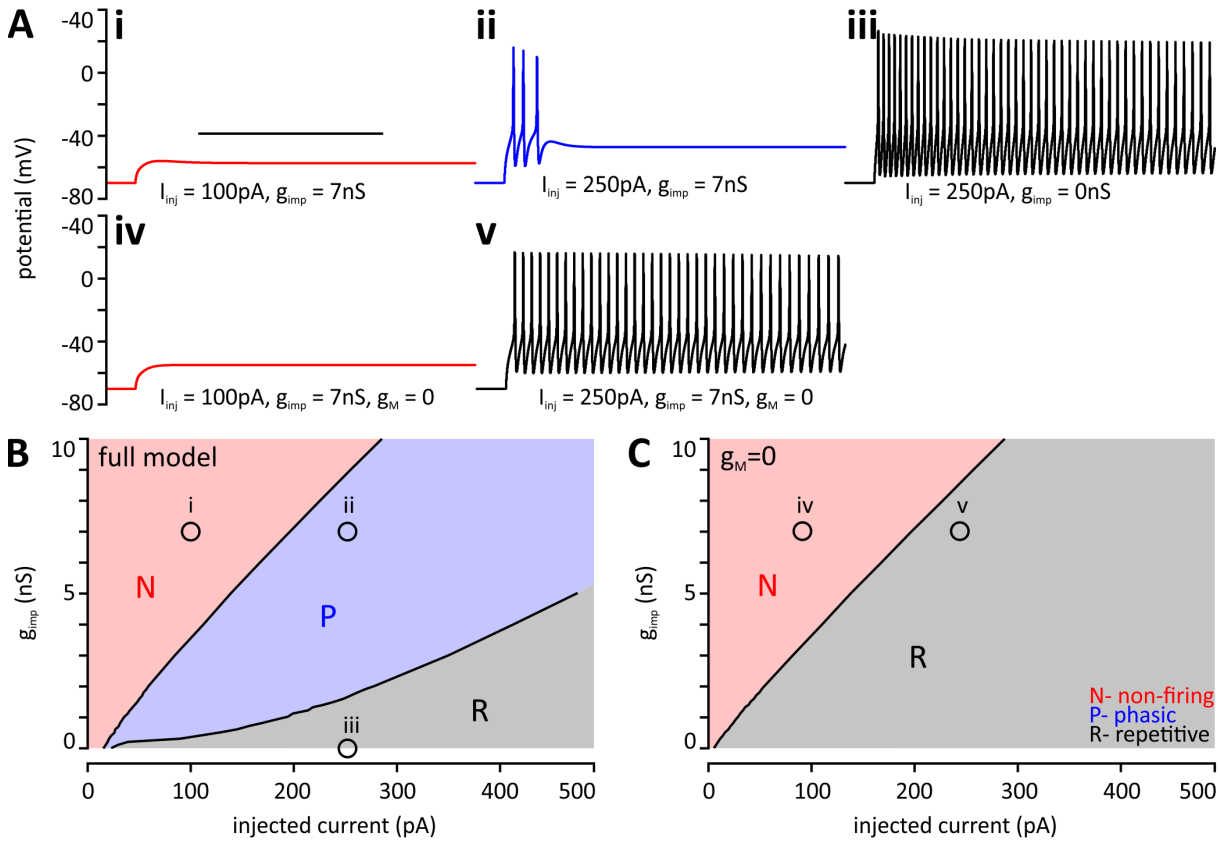

Figure 2.4 Simulated impalement can alter firing properties.
A, Impact of injected current and impalement conductance, g_{imp}, on firing properties. Voltage response of a model cell to subthreshold (i) and suprathreshold (ii) current injection after gimp is set to 7nS, analogous to a microelectrode recording. Only phasic firing is observed. (iii) Repetitive firing is observed when gimp is set to 0nS, analogous to a whole-cell recording. When g_M is removed from the model, the same parameters used in i and ii lead to non-firing (iv) and repetitive firing (v). B, Shaded regions indicate the set of all parameters which lead to non-firing (N, red), phasic firing (P, blue), and repetitive firing (R, black/gray). At g_{imp}=0nS the model neuron transitions rapidly from N to R, and repetitive firing results from any current injection above ~20pA. At gimp = 7nS, the model neuron transitions from N to P at around 200pA current injection, and repetitive firing is not observed for injected current less than 500pA. C, same as B with g_M set to 0nS. Removing I_M from the model by setting g_M=0nS eliminates phasic firing altogether, i.e., cells transition directly from N to R regardless of impalement conductance. Open circles in B and C indicate the g_{imp} and injected current values used to generate traces in A. Standard model with g_{leak}=0.5nS.

Prior studies have reported that phasic firing sympathetic neurons could instead fire repetitively if I_M was blocked (Brown and Adams, 1980; Cassell et al., 1986). To test this, we blocked I_M in our model cell by setting g_M to 0nS. This change completely eliminated phasic firing in the model, and only non-firing (Figure 2.4Aiv) or repetitive firing was observed (Figure 2.4Av). To more extensively characterize this phenomenon, the boundaries between each of the three firing

types were identified using a binary search algorithm. In the case where I_M is included in the model (Figure 2.4B), there was a rapid transition from repetitive to phasic firing as g_{imp} is increased. When I_M is removed (Figure 2.4C), the phasic firing region (P) disappears.

2.4.5 *Spike rate adaptation*

Implicit in the observation that sustained firing rates were lower than initial observed frequencies is that all cells displayed spike rate adaptation (SRA), or a decrease in firing rate over time. We were able to replicate SRA in our model (Figure 2.5A). The time-course of adaptation consists of a fast and a slow phase (Figure 2.5B).

The difference between the initial firing rate and the sustained firing rate becomes more pronounced as injected current is increased in all cells. This can be illustrated by comparing the maximal f-I curve to the sustained f-I curve in both recorded and model neurons over a range of current injection (Figure 2.5C). This relationship between maximal and sustained firing rate is a common feature of adapting neurons (Benda and Herz, 2003).

Several mechanisms have been proposed to underlie SRA in different neuronal populations including Na^+ channel inactivation (Miles et al., 2005), fast AHP summation (Powers et al., 1999), activation of I_{KCa} (Miles et al., 2005) and activation of I_M (Yi et al., 2015). We selectively removed conductances from the model and determined which were primarily responsible for SRA (Figure 2.5D). Removal of I_{KCa} preferentially impaired the later phase of adaptation (curve 1) while removal of I_M preferentially impaired the early phase of adaptation (curve 2). Removal

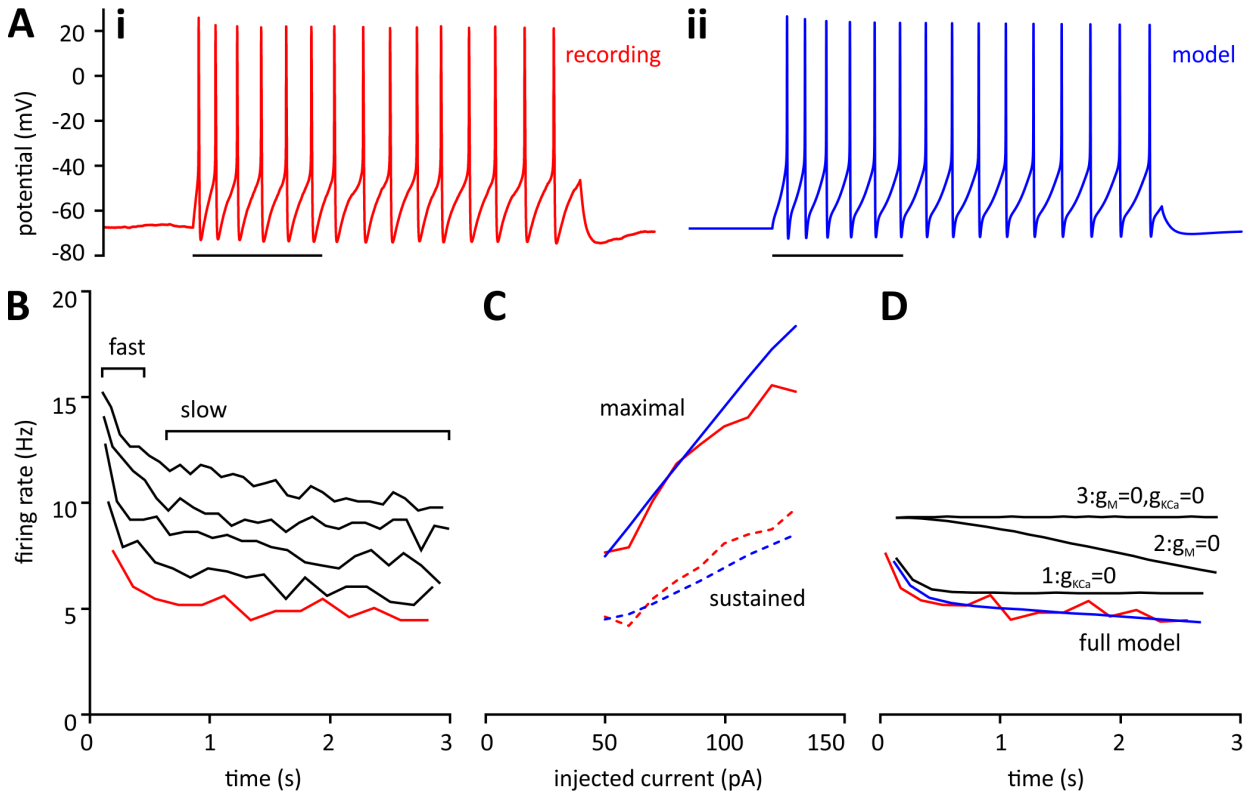

Figure 2.5 Spike rate adaptation depends on both I_M and I_{KCa}.
A, (i) Representative trace showing tSPN response to 50pA current injection. Note that the inter-spike interval increases over time, corresponding to a decrease in instantaneous frequency. (ii) Trace from a model cell chosen to fit the recording shows similar SRA for 50pA current injection. Maximal conductances are (in nS): G_{Na}=400, G_K=3000, G_{CaL}=1.2, G_M=40, G_{KCa}=60, G_A=80, G_H=1, G_{leak}=2. Scale bar in both panels is 1 second. B, Instantaneous frequency versus time for the same recorded cell at 50, 70, 90, 110, 130pA current injection (from bottom to top). The 50pA curve (red) corresponds to the trace in panel Ai. Fast and slow components of adaptation are indicated. C, Maximal and sustained *f*-I curves match well between recorded and modeled cell over a range of injected currents. Red, maximal (top, solid) and sustained (bottom, dashed) *f*-I curves for the cell in panel Ai and B. Blue lines are the corresponding *f*-I curves from the model cell in panel Aii. D, Instantaneous frequency versus time curves for the model cell in panel Aii. The recorded 50pA curve from panel B is reproduced for comparison to the analogous curve generated in the model cell in Aii (blue). Black curves numbered 1-3 represent effect of removal of two conductances from the model. Removal of g_{KCa} (curve 1) predominantly influences the slow SRA. Removal of g_M (curve 2) predominantly influences the fast SRA. Removal of both (curve 3) eliminates SRA. The ordinate axis is shared among panels B-D.

of both I_{KCa} and I_M completely eliminated SRA (curve 3). Our model supports the conclusion that the combination of these conductances is necessary in order to replicate SRA.

2.4.6 *Cell firing type classification*

We noted variability in spike height of the initial spike compared to subsequent spikes in a spike train during repetitive firing. Neurons were divided into three categories based on the peak voltage of the initial spike in a spike train compared to the peak voltage of subsequent spikes. Of the 35 neurons examined, the initial spike had slightly lower amplitude than subsequent spikes in 19 cells (type 1), and substantially higher amplitude in 12 cells (type 2) (Figure 2.6A). Note that this classification scheme is distinct from the classical Hodgkin firing criteria (Hodgkin and Huxley, 1952). The classification scheme presented here provides a quantitative way to differentiate cells into subtypes based on simple electrophysiological measures. In type 1 and 2 cells, this phenomenon became more pronounced with greater current injection. In 4 cells, both firing patterns were observed, with type 1 characteristics at lower current steps giving way to type 2 characteristics at higher current steps (type 3). The difference between the initial spike peak voltage and the mean spike peak voltage was plotted for all cells as a function of calculated change in membrane voltage (injected current × R_{in}) (Figure 2.6B). These differences did not appear to be associated with any basic membrane properties, threshold properties or the fAHP (defined below). In contrast, all measured parameters related to action potential (AP) shape showed significant difference between groups including maximal rise slope (Figure 2.6C), peak value (Figure 2.6D) (one-way ANOVA). All AP parameters differed significantly between type 1 and type 2 cells. A summary of statistical measures is given in Table 2.1. However, as a post

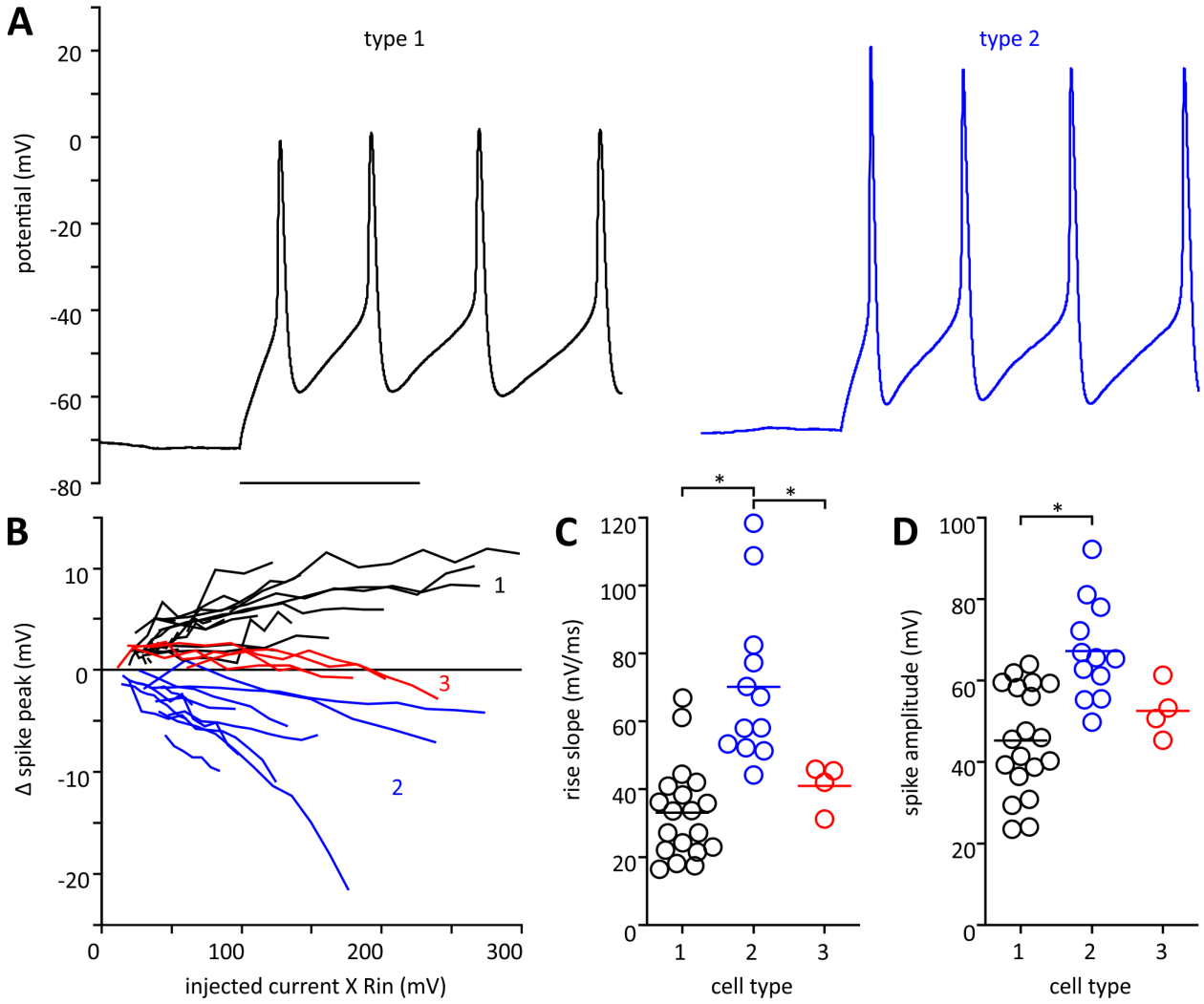

Figure 2.6 tSPNs are differentiable into subtypes based on direction of spike height changes.
A, Example traces from a type 1 (left, black) and type 2 (right, blue) cell. Scale bar 200ms. B, Population of cells showing a variety of firing types. The difference in the initial spike peak versus the mean of all subsequent spike peaks is plotted versus the product of injected current and input resistance for all cells (n=39). Type 1 cells with a positive change in spike peak are shown in solid black line; Type 2 cells with a negative change in spike peak are shown in dotted blue line; Type 3 cells which convert from type 1 to type 2 dynamics as injected current is increased are shown in dashed red line. C, Maximal rise slope for all three cell types. Type 2 cells have a significantly higher rate of depolarization than type 1 and 3 (P=.001; P=.04 respectively). D, Amplitude of the initial spike at rheobase current injection. Type 2 cells have significantly higher peak values than type 1 but not type 3 (P=.001; P=.09 respectively). Horizontal bars indicate mean value for C and D.

	Type 1	Type 2	Type 3	
Membrane properties				
RMP, mV	−60.0 ± 7.6 (19)	−57.5 ± 5.4 (12)	−63.0 ± 6.8 (4)	$F_{(2,32)}$=0.66 p=0.52
R_{in}, MΩ	1041 ± 643 (19)	961 ± 526 (11)	1285 ± 381 (4)	$F_{(2,31)}$=0.45 p=0.64
τ_m, ms	96.4 ± 60.8 (19)	83.1 ± 57.6 (11)	90.8 ± 16.5 (4)	$F_{(2,31)}$=0.19 p=0.83
C_m, pF	95.0 ± 28.7 (19)	84.9 ± 24.5 (11)	73.0 ± 15.4 (4)	$F_{(2,31)}$=1.4 p=0.27
Threshold				
Absolute, mV	−43.5 ± 6.6 (19)	−40.4 ± 5.9 (12)	−43.2 ± 4.2 (4)	$F_{(2,32)}$=0.97 p=0.39
Relative, mV	24.9 ± 6.5 (19)	24.0 ± 4.9 (12)	23.6 ± 9.1 (4)	$F_{(2,32)}$=0.11 p=0.90
Calc. rheobase, pA	32.8 ± 20.4 (19)	30.8 ± 15.8 (11)	20.1 ± 11.5 (4)	$F_{(2,31)}$=0.80 p=0.46
Action potential				
Amplitude, mV	45.3 ± 13.1[a] (19)	67.1 ± 12.1[b] (12)	52.6 ± 6.6 (4)	$F_{(2,32)}$=11.6 $p=1.7\cdot10^{-4}$*
Peak, mV	1.8 ± 15.0[a] (19)	26.7 ± 8.9[b] (12)	9.4 ± 9.3[a] (4)	$F_{(2,32)}$=14.0 $p=4.1\cdot10^{-5}$*
Half-width, ms	5.1 ± 0.9[a] (19)	3.7 ± 0.7[b] (12)	4.4 ± 0.5 (4)	$F_{(2,32)}$=10.8 $p=2.6\cdot10^{-4}$*
Rise slope, mV/ms	33.1 ± 13.9[a] (19)	70.0 ± 23.2[b] (12)	41.0 ± 6.8[a] (4)	$F_{(2,32)}$=17.0 $p=9.3\cdot10^{-6}$*
fAHP				
Amplitude, mV	−13.9 ± 2.8 (14)	−17.3 ± 4.6 (8)	−13.3 ± 3.2 (2)	$F_{(2,21)}$=2.6 p=0.10
Half-decay, ms	86.5 ± 27.6 (14)	68.2 ± 40.2 (8)	85.8 ± 66.3 (2)	$F_{(2,21)}$=0.73 p=0.50
Duration, ms	245 ± 58 (14)	213 ± 77 (8)	181 ± 101 (2)	$F_{(2,21)}$=1.1 p=0.34

Table 2.1 Comparison of basic properties of neuron subtypes

Values given as mean ± SD with number of observations in parentheses. a,b Statistically different groups as determined by one-way ANOVA and Tukey's post hoc test. Asterisk indicates statistically significant comparison at α=0.05. RMP, resting membrane potential; Rin, input resistance; τm, membrane time constant; Cm, membrane capacitance; fAHP, afterhyperpolarization.

hoc power analysis indicated a power of 0.5, we cannot conclusively say that there are no other significant differences between groups.

2.4.7 *Afterhyperpolarization*

Afterhyperpolarization (AHP) dynamics play an important role in regulating neuronal firing. Based on decay time, we identified three types of AHP within the thoracic ganglia. These include the fast AHP (fAHP) after a single action potential, and the slow AHP (sAHP) and ultra-slow AHP (usAHP) after multiple action potentials (Figure 2.7A).

Fast post-spike after-hyperpolarization (fAHP) amplitude, half-decay time, and duration were measured at rheobase current injection (Figure 2.7Ai). Parameters related to fAHP are summarized in Table 2.2. Half-decay time was very well correlated with duration and more reliably obtained, so further analysis focused on fAHP half-decay time. fAHP half-decay time was compared to passive membrane properties and rheobase. fAHP half-decay time was not correlated with R_{in}, C_m, or rheobase, but was moderately correlated with τ_m. Previous studies have reported an inverse relationship between fAHP duration and firing rate in motoneurons (Brownstone et al., 1992; Stauffer et al., 2007). To determine if this relationship exists in postganglionic neurons, we plotted fAHP half-decay time versus sustained firing rate at two times the minimal suprathreshold current injection. Note that this corresponds to twice the current magnitude used to estimate fAHP half-decay time. We found that there is indeed a moderate negative correlation between fAHP half-decay time and maximal firing rate (Figure 2.7B). fAHP half-decay time was also moderately correlated with sustained f-I slope but not f-I slope.

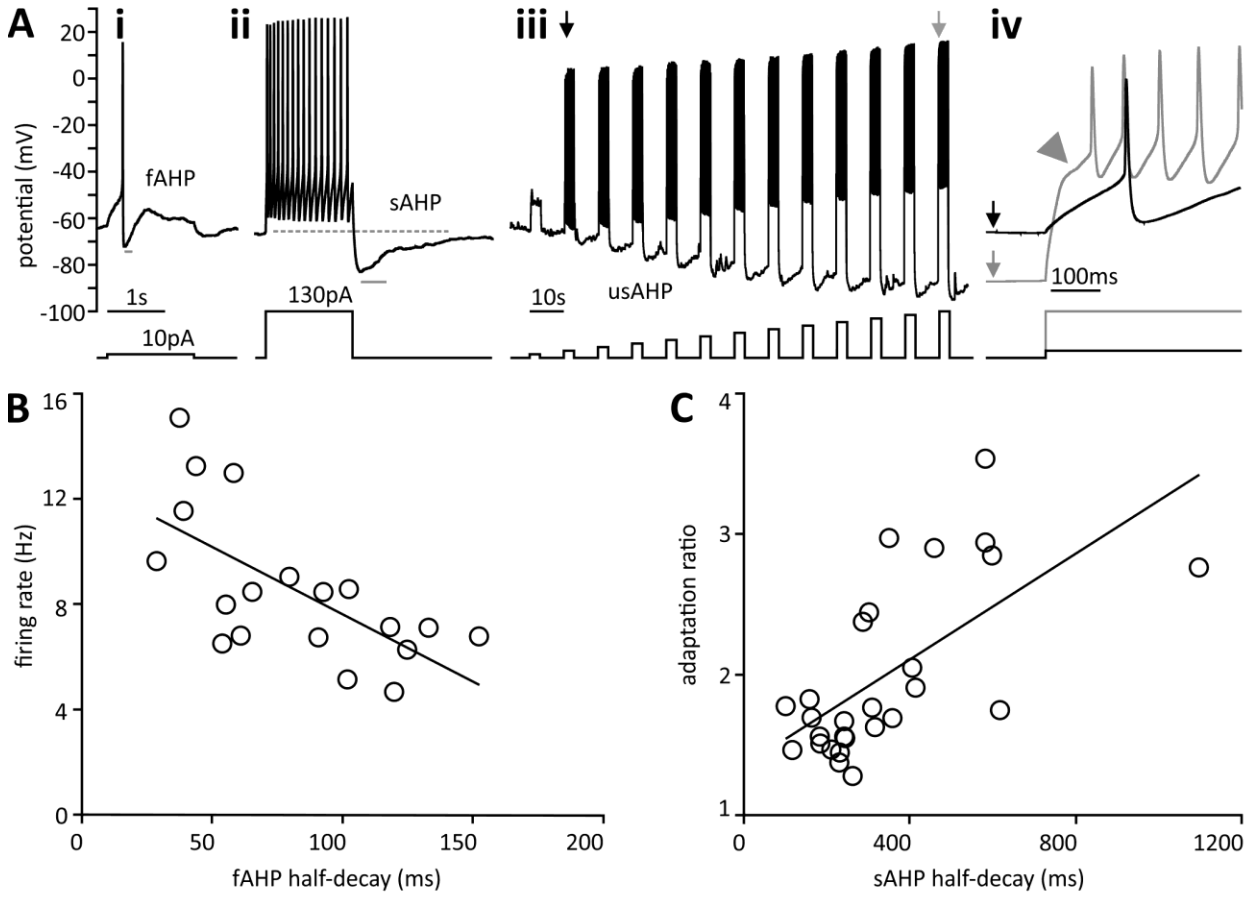

Figure 2.7 Afterhyperpolarization.
A, Side by side comparison of three types of AHPs. (i) fAHP present after single spike. (ii) sAHP is present in the same cell only after repetitive firing. The half-decay time of fast and slow AHPs are indicated by the gray bar beneath each trace. Scale bar 1s. (iii) Depolarizing current steps (10 to 130pA in 10pA increments) in a different cell showing the progressive hyperpolarization characteristic of the usAHP. Scale bar 10s. (iv) Expanded view of voltage traces in Aiii indicated by vertical arrows. Note that the gray trace is hyperpolarized by 20mV compared to the black trace and has a characteristic "notch" (arrowhead) upon depolarization. Current injection profile is shown below each trace. B, fAHP half-decay was negatively correlated with maximal firing rate at twice the minimal suprathreshold current. C, SRA ratio is positively correlated with sAHP half-decay. Black line is the linear regression.

Slow AHPs (sAHP) were also observed following larger depolarizing steps that elicited higher repetitive firing frequencies (Figure 2.7Aii). Only cells displaying obvious sAHP were analyzed (n=27 of 35). sAHPs were measured at maximal current injection. Parameters related to sAHP are summarized in Table 2.2. sAHP half-decay time was four-fold longer on average than fAHP half-decay, but the two were not correlated. To examine the relationship between sAHP and SRA, we plotted the sAHP half-decay versus the SRA ratio for 27 cells (Figure 2.7C). We found

the two parameters were significantly correlated. A summary of correlation parameters for both fAHP and sAHP is provided in Table 2.3. As with SRA, our computational model showed that I_M and I_{KCa} were capable of reproducing sAHP after repetitive firing (not shown).

Prior work in the rabbit superior cervical ganglion identified a long-lasting AHP following sustained depolarization that was due to the ouabain sensitive Na^+/K^+-ATPase (Lees and Wallis, 1974). In the neonatal mouse spinal cord, it has been shown to be due to activation of α3 Na^+/K^+-ATPase (Picton et al., 2017). This AHP is unique in its ability to hyperpolarize a cell membrane beyond the reversal potential of K^+. We identified an AHP with a similar time-course. We injected depolarizing current to cause the cell to fire repetitively. This repetitive firing led to a steadily increasing hyperpolarization (Figure 2.7Aiii). In the example shown, induced epochs of repetitive firing led to a 20mV membrane hyperpolarization (Figure 2.7Aiv). This feature was present in 2 of 14 cells tested with a current step protocol that would allow for its observation. Of note, the usAHP was observed only in relatively high resistance cells when ATP and GTP were included in the electrode solution. This AHP was also able to achieve a membrane potential of −101.7 ± 11.5 mV, which is more negative than the calculated −98 mV K^+ reversal potential. The time-course of this hyperpolarization is too long to be due to I_M or I_{KCa}.

2.4.8 *Subthreshold conductances*

Subthreshold conductances can play an important role in determining cell excitability and firing properties. We evaluated activation of these conductances with current steps that included assessment at hyperpolarized membrane potentials seen during the usAHP. In response to depolarizing current steps, membrane voltage first followed an exponential time-course with

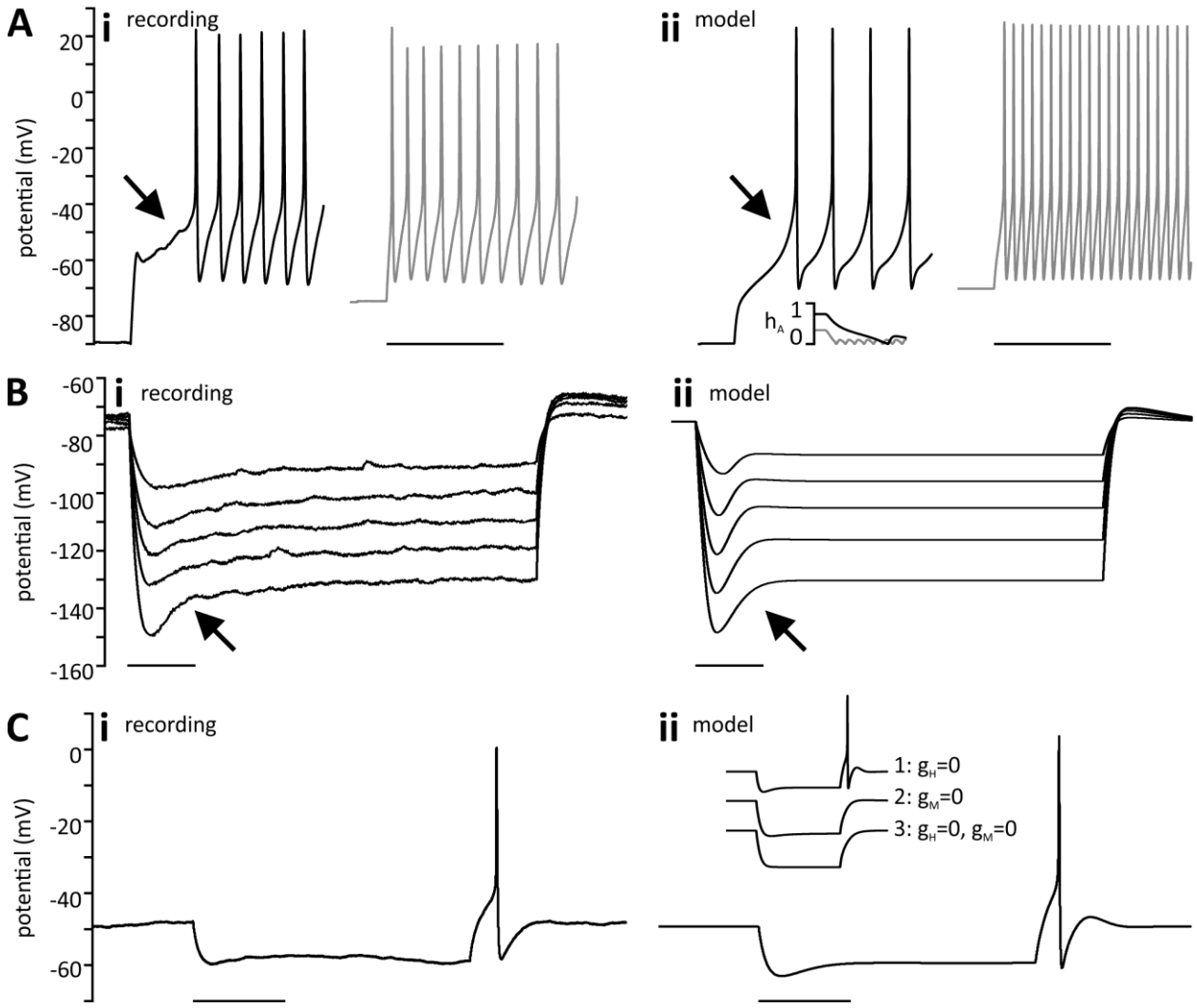

Figure 2.8 Subthreshold conductances.

A, (i) A cell depolarized from −90 mV exhibits a characteristic notch (arrow) accompanied by a delay in spiking (black trace). The same cell depolarized from −70mV does not have a notch (gray trace). (ii) Model neuron showing comparable results with pre-spike inflection seen only for hyperpolarized trace. Standard model with G_M=10, G_{KCa}=10, G_A=90, G_{leak}=0nS. Inset: Magnitude of h_A at onset of current injection shows that I_A is less inactivated (h_A is higher) at hyperpolarized voltage, and I_A takes longer to fully inactivate. Scale bars represent 500ms for all panels. B, (i) Voltage "sag," indicated by arrow, upon hyperpolarization beyond −90mV in a cell held at −70mV. Note that the effect becomes more pronounced with greater hyperpolarization. (ii) Model neuron showing similar sag. Standard model with G_A=5 and G_{leak}=.1nS. C, (i) Hyperpolarizing trace from a different cell held at −50mV showing rebound spiking associated with voltage sag. (ii) Model neuron showing rebound spiking at the same holding voltage and current injection. Maximal conductances are (in nS): G_{Na}=200, G_K=2000, G_{CaL}=1.2, G_M=20, G_{KCa}=20, G_A=20, G_H=1, G_{leak}=2. Removal of g_H (curve 1) does not inhibit rebound firing. Removal of g_M eliminates firing (curve 2) as does removal of both currents (curve 3).

subsequent recruitment of voltage-gated conductances that altered the trajectory. In 24 of 35 cells, membrane trajectory exhibited a negative deflection from the exponential trajectory which preceded activation of voltage gated Na^+ conductance. The observed deflection, or "notch", in membrane led to a delay in the first action potential in a train (Figure 2.8Ai) and has been described previously in tSPNs (Jobling and Gibbins, 1999). This phenomenon was often observed at a holding potential of −70mV, and became more pronounced with greater hyperpolarization (−90mV). This is consistent with activation of the transient, voltage-gated A-type K^+ current (I_A). To test the contribution of I_A to the notch and delayed firing, we held a model neuron at two different holding potentials and found that the change in trajectory was indeed attributable to de-inactivation of I_A (Figure 2.8Aii) (Rush and Rinzel, 1995). Notably, a similar notch was observed in cells displaying usAHP (Figure 2.7Aiv), demonstrating that the usAHP leads to a state of membrane hyperpolarization where I_A would delay onset of firing.

During hyperpolarizing current injection, a depolarizing voltage "sag" was often observed. When present, a voltage sag was easily detected with membrane hyperpolarization beyond −100mV (Figure 2.8Bi) but was also observed at less negative hyperpolarization (Figure 2.8Ci). We found a voltage sag in 17 of 28 cells hyperpolarized to at least −100mV from a holding potential of −70mV. This phenomenon has been previously reported in mouse tSPNs (Jobling and Gibbins, 1999) and other mammalian sympathetic neurons (Cassell et al., 1986) where it has been attributed to the anomalous rectifier, or H-current (I_H). To support a role for I_H, this conductance was implemented in the computational model and was found to reproduce the observed voltage sag (Figure 2.8Bii). I_H has also been shown to contribute to a more depolarized membrane potential (Pape, 1996; Lamas, 1998), so we compared resting membrane potential in cells with

Property	mean ± SD (n)	range
Membrane properties		
RMP, mV	−59.8 ± 6.8 (35)	−50 to −80
Input Resistance, MΩ	1044 ± 576 (34)	246 to 2297
Input conductance, nS	1.31 ± 0.84 (34)	0.44 to 4.1
Membrane time constant, ms	91.5 ± 55.5 (34)	19 to 234
Capacitance, pF	89.1 ± 26.6 (34)	51 to 157
Threshold		
Absolute voltage, mV	−42.4 ± 6.2 (35)	−29.2 to −58.8
Relative to V_{hold}, mV	24.5 ± 6.2 (35)	11.8 to 38.9
Measured rheobase, pA	27.5 ± 16.5 (35)	5 to 70
Calculated rheobase, pA	30.7 ± 18.2 (34)	10.1 to 95.9
Action Potential		
Amplitude, mV	53.6 ± 15.7 (35)	23.4 to 92.1
Peak, mV	11.2 ± 16.9 (35)	−30.8 to 47.0
Half-width, ms	4.6 ± 1.0 (35)	2.9 to 7.2
Rise slope, mV/ms	46.6 ± 24.1 (35)	16.3 to 118
Fast afterhyperpolarization		
Amplitude, mV	15.0 ± 3.7 (24)	6.7 to 21.1
Half-decay, ms	80.4 ± 34.5 (24)	28.6 to 152
Duration, ms	229 ± 68 (24)	109 to 363
Slow afterhyperpolarization		
Amplitude, mV	8.5 ± 4.5 (28)	2.8 to 18.4
Half-decay, ms	342 ± 211 (27)	101 to 1097
f-I slope		
Maximal, Hz/pA	0.13 ± 0.04 (35)	0.06 to 0.22
Sustained, Hz/pA	0.06 ± 0.04 (33)	−0.16 to 0.11

Table 2.2 Basic properties of tSPNs
Values of basic properties of tSPNs reported as mean ± SD and range of observed values.

(n=17) and without (n=11) evidence of I_H but found no significant differences (Student's t-test, two-tailed, p=0.17).

I_H has also been implicated in post-inhibitory rebound firing (Pape, 1996; Ascoli et al., 2010; Engbers et al., 2011; Ferrante et al., 2017). Sag was seen in 12 of 13 tSPNs exhibiting rebound firing, but rebound firing was only observed when cells were held closer to firing threshold (between −60 and −50mV; Figure 2.8Ci) where I_M has been shown to be responsible for inducing a voltage sag and rebound firing (Constanti and Galvan, 1983).

		r	R^2	n	p
Membrane properties					
R_{in}	τ_m	0.84	0.70	34	$6.2 \cdot 10^{-10}$*
″	C_m	−0.11	0.01	″	0.55
τ_m	C_m	0.40	0.16	″	0.020
Rheobase					
Calculated I_{rheo}	Measured I_{rheo}	0.82	0.68	34	$2.0 \cdot 10^{-9}$*
″	V_{hold}	−0.18	0.03	″	0.30
″	g_{in} (R_{in}^{-1})	0.85	0.72	″	$3.0 \cdot 10^{-10}$*
″	τ_m^{-1}	0.72	0.52	″	$1.5 \cdot 10^{-6}$*
″	C_m	0.06	0.00	″	0.73
Firing frequency					
f_{max} @ 100pA	R_{in}	0.58	0.33	30	0.00086*
f_{sus} @ 100pA	R_{in}	0.21	0.05	26	0.29
f_{max}-I slope	R_{in}	0.36	0.13	34	0.039
″	I_{rheo}, calc.	−0.51	0.26	″	0.0023
″	τ_m	0.14	0.02	″	0.43
″	C_m	−0.31	0.10	″	0.073
f_{sus}-I slope	R_{in}	0.29	0.09	32	0.10
″	I_{rheo}, calc.	−0.24	0.06	″	0.19
″	τ_m	0.26	0.07	″	0.15
″	C_m	−0.07	0.00	″	0.70
Afterhyperpolarization					
fAHP half-decay	fAHP duration	0.84	0.70	24	$3.0 \cdot 10^{-7}$*
″	R_{in}	0.34	0.12	″	0.10
″	C_m	0.15	0.02	″	0.47
″	τ_m	0.43	0.18	″	0.036
″	I_{rheo}, calc.	−0.36	0.13	″	0.083
″	f_{max} @ $2 \cdot I_{min}$	−0.66	0.43	19	0.0022
″	f_{sus} @ $2 \cdot I_{min}$	−0.42	0.18	12	0.17
″	f_{max}-I slope	−0.02	0.00	24	0.92
″	f_{sus}-I slope	0.45	0.20	22	0.037
″	sAHP half-decay	−0.38	0.14	19	0.11
sAHP half-decay	SRA ratio	0.65	0.42	27	0.00027*

Table 2.3 Selected correlations between tSPN parameters

Selected correlations reported in results. r, Pearson's correlation coefficient. R^2, coefficient of determination. n, number of observations. p-values calculated from two-tailed t-test. Asterisk indicates statistically significant correlation at Šidák-corrected $\alpha<0.0017$. R_{in}, input resistance; τ_m, membrane time constant; C_m, membrane capacitance; I_{rheo}, rheobase current; V_{hold}, holding voltage; g_{in}, input conductance; V_{th}, threshold voltage; f_{max}, maximal instantaneous firing rate; f_{sus}, sustained firing rate; I_{min}, minimal suprathreshold current; fAHP, fast afterhyperpolarization; sAHP, slow afterhyperpolarization.

We used a computational model to understand the relative contributions of I_H and I_M and determined that sag is due to I_H for significant hyperpolarizations, and I_M for more moderate hyperpolarization. Rebound firing can occur in the absence of I_H but does not occur in the absence of I_M following release from moderate (~10mV) hyperpolarization, indicating that I_H is neither necessary nor sufficient to induce rebound firing in tSPNs (Figure 2.8Cii).

2.4.9 *Effect of spinal cord injury*

Spinal cord injury is known to impair normal autonomic function (Hou and Rabchevsky, 2014). In order to determine if such injury has an effect on the intrinsic membrane properties of tSPNs, we performed a T2 spinal cord transection on 19 adult mice. Mice were allowed to survive for 3 weeks (n = 5) or 6 weeks (n = 14), after which whole-cell recordings were obtained. Data from mice in the 3 and 6 week groups were pooled to increase statistical power. We found that the intrinsic properties of tSPNs were indistinguishable between groups for nearly all measures. There was a decrease in capacitance, but the statistical significance disappears if p-values are adjusted for multiple comparisons. A summary of parameter values and statistical measures is provided in Table 2.4.

2.5 **Discussion**

2.5.1 *Re-appraisal of physiological consequence of passive membrane properties*

We obtained high-quality recordings of mouse tSPNs and built a computational model to provide mechanistic insight into their function. Whole-cell recordings preserve membrane properties and provide an accurate representation of tSPN function. This is critically important, as the impalement conductance introduced by microelectrode recordings can change passive membrane

Property	Naïve	SCI	p
Membrane properties			
RMP, mV	−59.8 ± 6.8 (35)	−59.7 ± 8.7 (26)	0.85
Input Resistance, MΩ	1044 ± 576 (34)	1426 ± 962 (26)	0.82
Membrane time constant, ms	91.5 ± 55.5 (34)	97.9 ± 44.5 (25)	0.15
Capacitance, pF	89.1 ± 26.6 (34)	81.1 ± 29.3 (25)	0.03*
Threshold			
Absolute voltage, mV	−42.4 ± 6.2 (35)	−46.0 ± 6.2 (25)	1.00
Relative to V_{hold}, mV	24.5 ± 6.2 (35)	24.1 ± 8.7 (25)	0.75
Measured rheobase, pA	27.5 ± 16.5 (35)	26.3 ± 19.3 (25)	0.99
Calculated rheobase, pA	30.7 ± 18.2 (34)	24.5 ± 14.0 (25)	0.97
Action Potential			
Amplitude, mV	53.6 ± 15.7 (35)	72.0 ± 10.3 (25)	0.11
Overshoot, mV	11.2 ± 16.9 (35)	25.9 ± 10.6 (25)	0.13
Half-width, ms	4.6 ± 1.0 (35)	4.4 ± 1.0 (25)	0.89
Rise slope, mV/ms	46.6 ± 24.1 (35)	62.8 ± 20 (25)	0.21
Fast afterhyperpolarization			
Amplitude, mV	15.0 ± 3.7 (24)	17.6 ± 4.2 (15)	0.06
Half-decay, ms	80.4 ± 34.5 (24)	103.6 ± 58.5 (15)	0.18
Duration, ms	229 ± 68 (24)	285.3 ± 113.3 (15)	0.10
f-I slope			
Maximal, Hz/pA	0.13 ± 0.04 (35)	0.12 ± 0.03 (24)	0.30
Sustained, Hz/pA	0.06 ± 0.04 (33)	0.06 ± 0.03 (24)	0.92
SRA ratio	1.9 ± 0.6 (35)	1.6 ± 0.3 (24)	0.20

Table 2.4 Comparison of basic properties in naïve and post-SCI
Values reported as mean ± SD. 3 week and 6 week post-SCI groups were pooled. p-values calculated by two-tailed t-test. RMP, resting membrane potential; SRA, spike rate adaptation; *, $p<0.05$; The data analysis for this table was the result of a collaboration with Yaqing Li.

properties (Staley et al., 1992; Cymbalyuk et al., 2002; Springer et al., 2015), reduce apparent excitability, underestimate the importance of synaptic convergence (Karila and Horn, 2000; Horn and Kullmann, 2007), and prevent repetitive firing (Springer et al., 2015).

Input resistance (R_{in}) and membrane time constant (τ_m) were highly correlated and their values, as well as rheobase, occupy an approximately ten-fold range. Values of R_{in} and τ_m are an order of magnitude larger than values previously obtained from the same population using traditional

microelectrode recordings (Blackman and Purves, 1969; Jobling and Gibbins, 1999), which indicates that the excitability of tSPNs has been substantially underestimated. Measured cell diameters in the T5 ganglion occupied a five-fold range (cf. Jobling and Gibbins, 1999). Capacitance (C_m) values occupied a three-fold range, and were unrelated to cell recruitment. The strong observed relationship between R_{in} and measures of firing threshold (i.e., rheobase) demonstrate that Ohmic processes dominate tSPN recruitment. These observations suggest that membrane resistivity rather than cell size is the primary determinant of recruitment threshold across the population (Gustafsson and Pinter, 1984), though it is unclear if the observed variability in excitability represents a population recruitment principle.

The preservation of the passive membrane electrical properties R_{in} and τ_m leads to synaptic events of greater amplitude and longer duration, which has important consequences for synaptic recruitment. Paravertebral neurons receive nicotinic EPSPs comprising both sub- and suprathreshold events of variable amplitude (Nishi and Koketsu, 1960; Blackman and Purves, 1969; Karila and Horn, 2000; Bratton et al., 2010). An overall increase in EPSP amplitude would convert many subthreshold events into suprathreshold events, thereby increasing tSPN firing rate (Bratton et al., 2010). Traditionally, summation of EPSPs was not thought to contribute to cell recruitment in paravertebral ganglia (North, 1986; McLachlan et al., 1997; Jänig, 2006). However, recent whole-cell recordings from rat superior cervical ganglion demonstrate long-duration sEPSPs with much greater capacity for summation (Springer et al., 2015). We also observed long-duration sEPSPs with decay time-constant comparable to τ_m and examples of sEPSP summation leading to cell recruitment. This provides direct support for the gain hypothesis for amplification of preganglionic activity (Karila and Horn, 2000; Horn and

Kullmann, 2007). The observed τ_m values indicate that tSPNs could act as integrators during states of strong preganglionic sympathetic drive from individual neurons (see Jänig, 1985; Ivanov and Purves, 1989) and could widen the temporal window for coincidence detection and summation of convergent synchronous preganglionic inputs (Skok, 1973; Konig et al., 1996; Ratte et al., 2013). These observations support the concept that tSPNs do not merely relay preganglionic activity, but rather actively integrate and amplify sympathetic output. Metabotropic receptor-mediated changes in intrinsic membrane conductances may further amplify this process (North, 1986; Karila and Horn, 2000).

Additionally important was the observation that all tSPNs were capable of firing repetitively, which contrasts traditional observations in all paravertebral neurons, including tSPNs, of phasic firing in response to sustained current injection (Jobling and Gibbins, 1999; Jänig, 2006; Springer et al., 2015). Recent whole-cell recordings in rat SCG similarly found paravertebral neurons were capable of repetitive firing, and suggested the discrepancy was a result of impalement conductance (Springer et al., 2015). We were able to replicate these results using our model; by introducing an impalement conductance consistent with microelectrode impalement, we were able to convert repetitively firing model neurons to phasically firing model neurons. Phasic firing after impalement injury appears to be dependent on the presence of I_M, as blocking I_M can convert sympathetic neurons from phasic to repetitively firing (Brown and Adams, 1980; Brown and Constanti, 1980; Cassell et al., 1986; Luther and Birren, 2009). This observation was reproduced by subtracting I_M in our model. I_{KCa} has also been shown to contribute to the interconversion of sympathetic neuron membrane firing properties (Sacchi et al., 1995; Luther and Birren, 2009). Thus, the firing properties of paravertebral sympathetic neurons that exhibit

I_M and I_{KCa} are particularly sensitive to impalement leak, which underscores the importance of using whole-cell recordings. Blackman and colleagues were able to observe repetitive firing with microelectrodes, a finding that has been consistently overlooked (Blackman and Purves, 1969). A possible explanation could be differences in ion channel expression between the mouse and guinea pig.

2.5.2 *The physiological relevance of repetitive firing in tSPNs*

The physiological relevance of repetitive firing in tSPNs in response to current stimulation might be dismissed if one assumes that postganglionic neurons are only driven by nicotinic preganglionic input. However, paravertebral neurons can exhibit long-lasting depolarization and sustained firing (Blackman and Purves, 1969; Janig et al., 1982; Kawatani et al., 1987). Activation of metabotropic muscarinic and various other non-cholinergic receptors are implicated (Janig et al., 1982; North, 1986; Kawatani et al., 1987; Elfvin et al., 1993). These studies support the idea that tSPNs can generate sustained sympathetic drive with limited influence from preganglionics.

Passive membrane properties and various conductances are responsible for sculpting the firing response of tSPNs. R_{in} is important in determining firing rate over a range of injected current values. R_{in} also impacts the slope of the f-I curve. tSPNs with steeper slope may be more effective at amplifying postganglionic output gain (Salinas and Thier, 2000; Zimmerman and Hochman, 2010). Given the relatively low steady-state firing rates of preganglionic neurons observed in vivo (Jänig, 2006), the physiological relevance of variability in response amplification is unclear (Springer et al., 2015).

However, synaptic drive may contribute to response amplification during bouts of metabotropic receptor-mediated sustained activity described above. We observe spontaneous excitatory post-synaptic currents with amplitudes ranging from 10pA to over 100pA (data not shown). Comparing these amplitudes to values of rheobase (range 5-70 pA) supports conditions where synaptic actions are capable of transient response amplification.

2.5.3 *Relating observed cellular properties to underlying conductances*

While the firing rate of tSPNs is strongly determined by the temporal dynamics of the fAHP, a feature carried by I_A and I_K in rodent SCG (Belluzzi and Sacchi, 1988), the mechanisms underlying spike rate adaptation (SRA) have not been studied in paravertebral ganglia including tSPNs. SRA has been well characterized elsewhere (Benda and Herz, 2003; Benda and Tabak, 2013). Contributions from I_M and I_{KCa} are among the proposed mechanisms (Sawczuk et al., 1997; Powers et al., 1999; Miles et al., 2005; Yi et al., 2015), and these currents have been previously identified in rodent paravertebral ganglia (Sacchi et al., 1995; Davies et al., 1996; Haley et al., 2000; Locknar et al., 2004; Maingret et al., 2008). Our modeling found that I_M and I_{KCa} were required to replicate the fast and slow components of SRA, respectively. I_M and I_{KCa} are also known to contribute to the slow AHP in rodent SCG and hippocampus (Storm, 1990; Sacchi et al., 1995), and inclusion of I_{KCa} or I_M in the model reproduced the sAHP after repetitive firing. That SRA ratio and sAHP half-decay were correlated further supports co-involvement of these conductances.

2.5.4 *Other factors contributing to modulation of tSPN excitability*

tSPNs are known to express I_A, I_H and I_M (Jobling and Gibbins, 1999). These currents have been shown to modulate EPSP amplitude, synaptic integration, membrane potential, and repetitive firing rate (Connor and Stevens, 1971; Storm, 1990; Rush and Rinzel, 1995; Hoffman et al., 1997; Lamas, 1998; Prescott et al., 2006; George et al., 2009; Kullmann et al., 2016). We found evidence of I_A, I_H and I_M in our recordings by observing phenomena such as notch, sag, and rebound firing, and we replicated their effects using computational modeling. These phenomena typically require hyperpolarization to emerge. While there are no known inhibitory synapses in sympathetic ganglia (McLachlan, 2007), a slow IPSP due to metabotropic activation of K^+ conductances has been observed in SCG (Libet and Kobayashi, 1974; North, 1986). Another method of hyperpolarization observed in a small group of tSPNs is the slowly developing usAHP that follows prolonged activity (Zhang and Sillar, 2012). The usAHP has been observed in rabbit SCG (Lees and Wallis, 1974) and reflects Na^+ dependent activation of the ouabain-sensitive α3 Na^+/K^+-ATPase (Picton et al., 2017). These long-lasting hyperpolarizations may provide a physiological mechanism by which the aforementioned phenomena may emerge.

3 Synaptic properties of thoracic postganglionic neurons

3.1 Abstract

Sympathetic postganglionic neurons (SPNs) receive and integrate synaptic input from preganglionic neurons in the spinal cord. The general organization has long been thought to follow an n+1 rule, whereby SPN activity is primarily driven by a single large (primary) synaptic input, while other (secondary) inputs are much smaller and inconsequential to cellular recruitment. Recent observations in rodent superior cervical and lumbar sympathetic chain neurons have challenged the idea that secondary inputs have a negligible effect on postganglionic firing. To determine synaptic organization within the thoracic chain, we undertook whole-cell voltage clamp recordings of thoracic sympathetic postganglionic neurons (tSPNs) and characterized the properties of spontaneous and evoked excitatory postsynaptic currents (EPSCs). We further examined whether expected reductions in spinal sympathetic preganglionic drive, at 3 and 6 weeks following high thoracic spinal cord injury (SCI), would lead to homeostatic changes in synaptic function.

Nearly all cells displayed some degree of spontaneous synaptic activity. Spontaneous frequency was highly variable between cells, ranging from nearly zero to 1.7Hz (mean = 0.22±0.38Hz). The amplitude of sEPSCs occupied a continuous 30-fold range across all cells (mean = 40.6±28.3pA). Amplitude comparisons of sEPSCs and optically evoked EPSCs (eEPSCs) suggested that some tSPNs received one or two inputs while others have 20-30. Frequency of sEPSCs roughly doubled following SCI. This indicates presynaptic plasticity that could involve increased number of preganglionic synapses and/or increased frequency at preexisting synapses. Amplitude of sEPSCs increased by 15% while decay time constant decreased by 17%. While

amplitude changes may occur by pre- or postsynaptic mechanisms, a decrease in EPSC decay supports plasticity by postsynaptic mechanisms.

3.2 **Introduction**

The ongoing activity of thoracic ganglia *in vivo* has not been studied due to their inopportune location within the thoracic cavity. Therefore, the *in vivo* activity of tSPNs must be inferred from recordings in SCG (Skok and Ivanov, 1983; Ivanov and Purves, 1989; McLachlan et al., 1997) and lumbar ganglia (Jänig, 1988). The ongoing activity of postganglionic neurons depends on the innervation target—vasoconstrictors innervating muscle and visceral vasculature are entrained to the cardiac cycle (Jänig, 1988) or respiration (Skok and Ivanov, 1983). Cutaneous vasoconstrictors, as well as pilomotor and sudomotor neurons are normally silent until activated by an external stimulus (Jänig, 2006). The number of synaptic inputs are approximately equal to the number of primary dendrites (Purves and Hume, 1981). Mouse thoracic neurons have approximately 6 primary dendrites on average (Jobling and Gibbins, 1999), so this is a reasonable estimate for the number of synaptic inputs. The synaptic innervation of postganglionic neurons is thought to be governed by the n+1 rule, whereby postganglionic neurons receive one primary synapse which evokes a suprathreshold response and few secondary synapses which evoke smaller EPSCs (Skok and Ivanov, 1983; Karila and Horn, 2000). Primary and secondary synapses are likely formed by the same preganglionic population (Bratton et al., 2010), but differ in the relative contributions of calcium channels (Ireland et al., 1999). Primary synapses are thought to be the primary drivers of postganglionic firing while the secondary synapses are inconsequential (McLachlan, 2007). These principles were worked out largely in the bullfrog sympathetic chain. It appears that the idea of two distinct classes of synaptic input

also holds for mammalian sympathetic ganglia based on calcium channel expression and AP shape (Skok and Ivanov, 1983; Ireland et al., 1999; Bratton et al., 2010), but the notion that secondary inputs are inconsequential has been recently called into question in SCG (Rimmer and Horn, 2010) and lumbar ganglia (Bratton et al., 2010). Recent whole cell recordings in SCG (Springer et al., 2015) and thoracic ganglia (McKinnon et al., 2019) reveal that sympathetic neurons have greater integrative capacity than previously envisioned. In fact, when driven by simulated preganglionic input, postganglionic neurons can fire at more than double the presynaptic firing rate (Springer et al., 2015).

Most prior studies of changes to the sympathetic nervous system after SCI have focused on reorganization within the spinal cord (Hou and Rabchevsky, 2014). Few if any have looked at the specific role of SCI on maladaptive plasticity within the sympathetic chain. However, previous studies have noted changes in the re-innervation properties of preganglionic-postganglionic interactions after injury. For example, after severing preganglionic axons, the remaining collaterals sprout and form new connections within the ganglion (Murray and Thompson, 1957; Liestol et al., 1987). Reorganization after nerve transection tends to reinstate a rough somatotopic organization (Njå and Purves, 1977b), similar to what is seen in the intact animal (Njå and Purves, 1977a; Lichtman et al., 1980). Furthermore, there is a preferential formation of primary or strong synapses after transection of sympathetic trunk (Ireland, 1999). It is unclear if any of these processes are present after SCI, but an increase in primary synapses would likely be accompanied by an increase in mean EPSC amplitude. The aim of the present study is to characterize the properties of spontaneous and evoked synaptic input to tSPNs using

whole cell recordings of mammalian thoracic sympathetic ganglia. We also aim to determine if any of these properties change after SCI.

3.3 **Results**

3.3.1 *Spontaneous EPSCs*

sEPSCs were observed in nearly all neurons (40 of 41). In some neurons, spontaneous events maintained a relatively high frequency (>0.5Hz) for more than a minute (Figure 3.1A). To validate comparison of firing rate across cells, it was necessary to establish that firing rate was relatively consistent over time. To determine the variability of instantaneous frequency over time, we plotted the instantaneous frequency of synaptic activity over time with a 30 second sliding window. This analysis was limited to neurons with relatively high sustained synaptic activity (>0.5Hz) which were recorded continuously for at least 5 minutes. Within the control group, only 2 cells met these criteria. In one cell recorded continuously for 15 minutes, the instantaneous frequency varied over time but did not appear to monotonically increase or decrease (Figure 3.1B). In the other cell, recorded for only 5 minutes, frequency was less variable. In general, however, high-frequency cells maintained high frequency for the duration of recording and the same was true of low-frequency cells. It is uncertain what factors might cause this variability in spontaneous synaptic frequency *in vitro*, but it may be indicative of a difference in the number of synaptic boutons making contact with a single tSPN or a difference in the frequency of release for a given bouton. We also characterized sEPSC amplitude and time constants of rise and decay (τ_R and τ_D, respectively) by restricting analysis to non-overlapping events. A summary of frequency and fitted parameters of spontaneous synaptic events are presented in Table 3.1. A histogram of sEPSC amplitudes, τ_R, and τ_D for a single cell can be seen

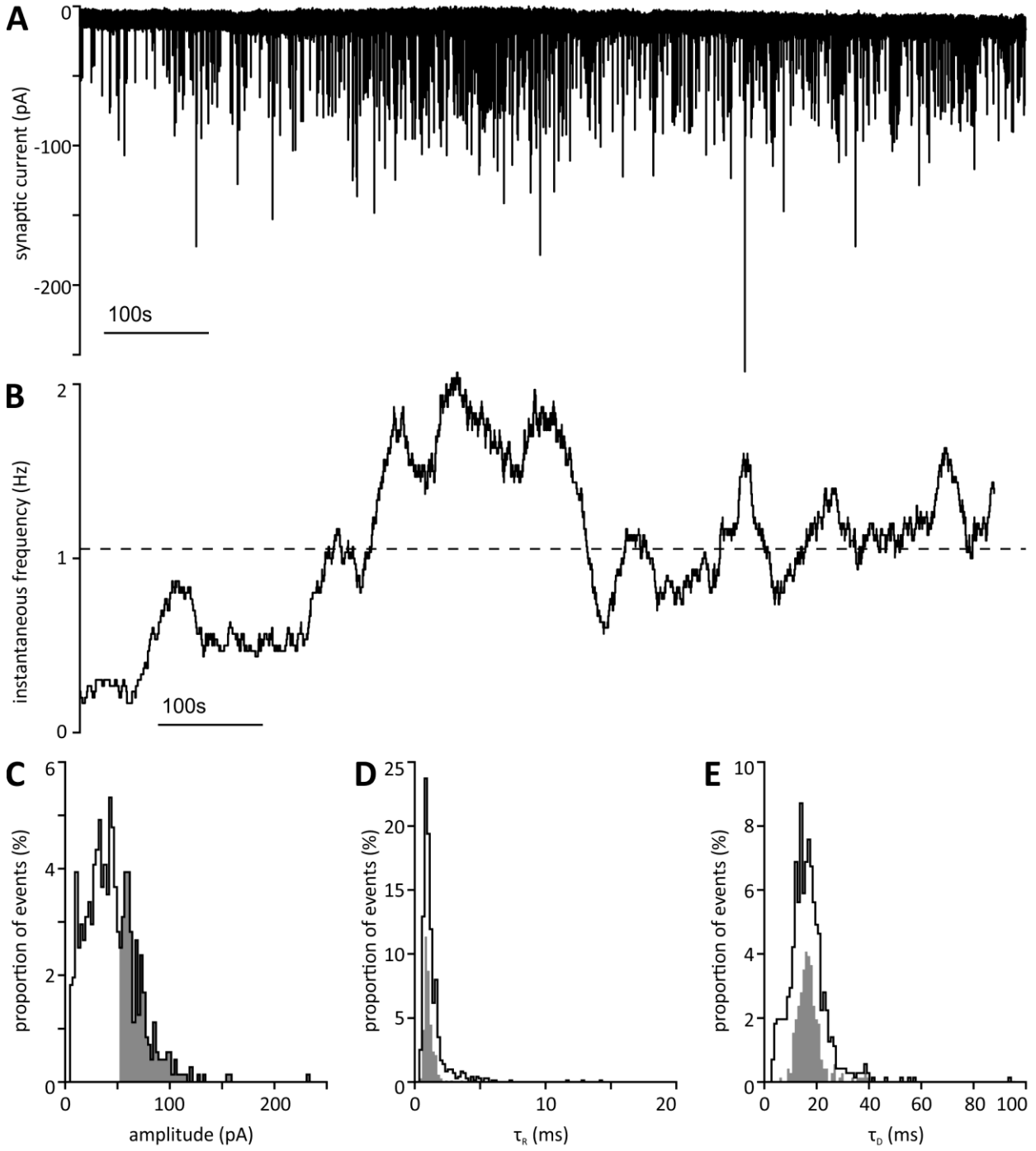

Figure 3.1 Characterization of spontaneous synaptic activity
A, Voltage clamp trace from a cell with above average levels of synaptic activity. Total duration was 15 minutes. B, Instantaneous frequency of synaptic input over time in the same cell, calculated with a 30s sliding window. C-E, Histogram of EPSC amplitudes, rise tau, and decay tau. Gray sub-histograms represent only sEPSCs with amplitude > 50pA.

in Figure 3.1C-E. Smaller amplitude events tend to have significantly longer τ_R (Figure 3.1C-E and Table 3.1).

3.3.2 *Comparison of evoked and spontaneous EPSCs*

sEPSCs can operate by release machinery that is distinct from evoked EPSCs (eEPSC) and activate distinct postsynaptic receptors in ionotropic glutamatergic synapses (Kavalali, 2015). To assess whether sEPSCs had observably different properties than eEPSCs, we compared responses in several cells from transgenic mice expressing channelrhodopsin (ChR2) in cholinergic neurons (ChAT-IRES-cre::R26-ChR2). In such recordings, it was possible to evoke EPSCs using a blue laser. We analyzed the amplitude of eEPSCs as a result of ramus illumination. This analysis was completed in 4 cells. In 2 cells, the amplitude of eEPSCs was an order of magnitude greater than sEPSCs from the same cell (Figure 3.2A,B). In 2 other cells, eEPSC and sEPSC magnitudes were similar (Figure 3.2C,D). However, even in cells that exhibited large eEPSCs, some smaller eEPSCs of a similar magnitude to the sEPSCs were also observed. This may suggest that smaller eEPSCs are unitary events while larger eEPSCs comprise multiple overlapping events recruited at the same time. Assuming that sEPSCs represent unitary events, comparing the amplitude of eEPSCs versus sEPSCs could indicate the number of synapses onto a particular neuron. This would be consistent with the distribution seen in Figure 3.2C. Though the near complete absence of overlap in amplitude in amplitude between sEPSCs and eEPSCs may argue against this, we cannot exclude the possibility that the lowest intensity optical recruitment already co-recruits several synaptic events. If eEPSC amplitude is indicative of the number of synaptic boutons contacting a neuron, we would expect a relationship between sEPSC frequency and eEPSC amplitude. Based on the four cells recorded here, there

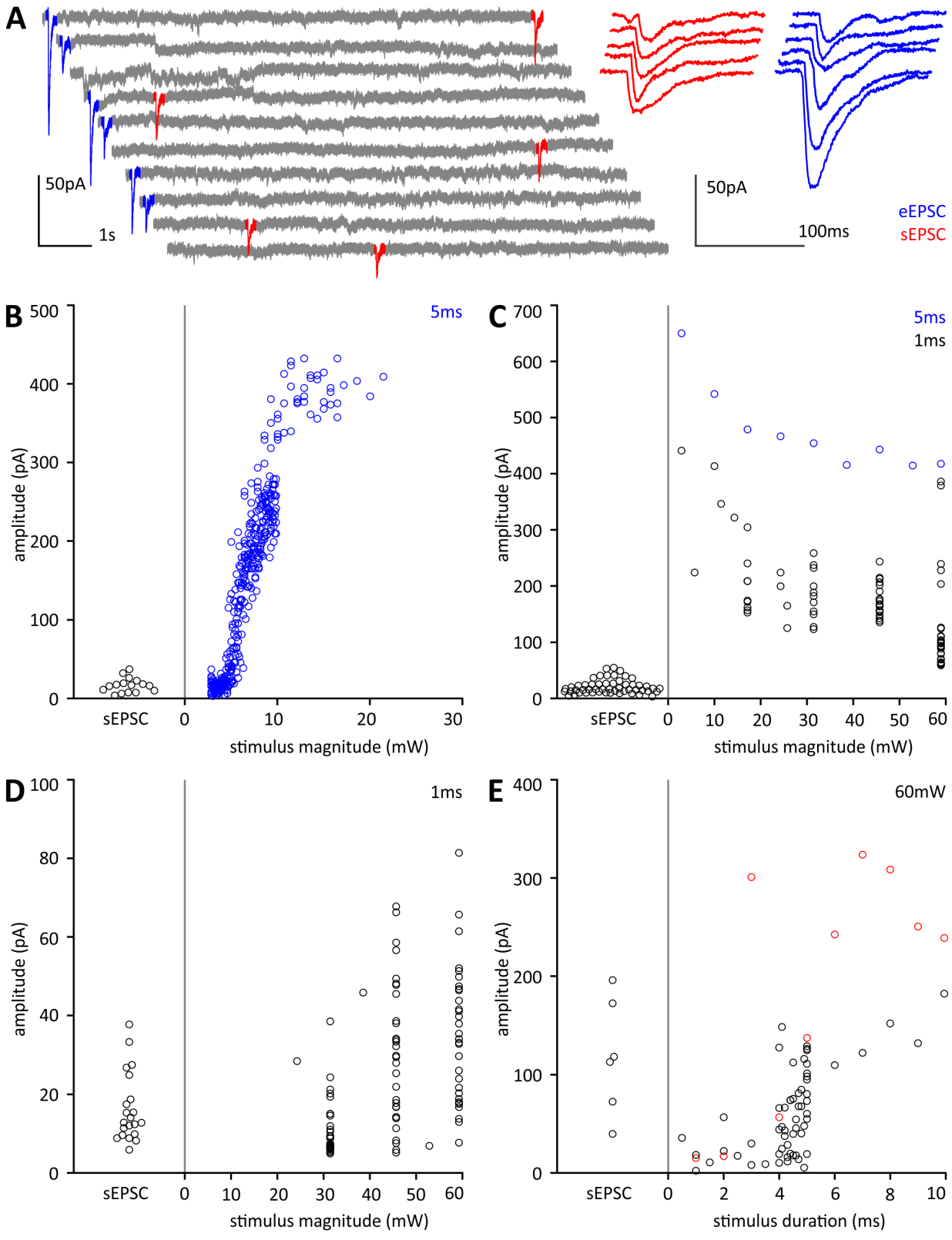
A
50pA
1s
50pA
100ms
eEPSC
sEPSC
B
5ms
amplitude (pA)
sEPSC
stimulus magnitude (mW)
C
5ms
1ms
amplitude (pA)
sEPSC
stimulus magnitude (mW)
D
1ms
amplitude (pA)
sEPSC
stimulus magnitude (mW)
E
60mW
amplitude (pA)
sEPSC
stimulus duration (ms)

Figure 3.2 Comparison of evoked and spontaneous EPSCs in 4 cells
A, Rastered trace showing evoked (blue) and spontaneous (red) EPSCs. Selected event traces are reproduced to the right for ease of comparison. B, The amplitude distribution of sEPSCs is compared to eEPSCs evoked by 5ms stimulus of varying intensity. Note that eEPSC amplitude is comparable to sEPSCs at low illumination and increases with illumination intensity to become much larger than sEPSCs. At higher intensity, action currents were occasionally evoked (not shown). 10 seconds between pulses. C, In a different cell, eEPSCs evoked by 1ms (black) or 5ms (blue) stimuli of varying intensity are much larger than sEPSCs. 10 seconds between pulses. D, In a different cell, eEPSCs evoked by 1ms stimulus of varying intensity are about twice as large as sEPSCs. 30 seconds between pulses. E, In a different cell, eEPSCs evoked by 60mW stimuli of varying duration are slightly larger than sEPSCs. 10 (red) or 30 (black) seconds between pulses.

does not appear to be such a relationship, but the low number of observations would preclude a more detailed analysis.

3.3.3 *Effect of spinal cord injury*

At three or six weeks after spinal cord injury (SCI), spontaneous synaptic events were observed in all cells (32 of 32). sEPSCs are important for regulating synaptic plasticity and development (Kavalali, 2015). We measured sEPSC amplitude, τ_R, and τ_D, and frequency to assess possible plasticity in synaptic function after SCI. All relevant parameters are reported in Table 3.1.

A change in amplitude of spontaneous events could indicate either a presynaptic (e.g. increased quantal content (Turrigiano et al., 1998)) or postsynaptic mechanism (e.g. increased receptor density, synaptic scaling (Queenan et al., 2012; Turrigiano, 2012)), while a change in the shape of sEPSCs, namely the time constants of rise and decay, could indicate changes in nicotinic receptor channel kinetics (*e.g*. different subunit composition or receptor modification via second messenger systems). To determine if any of these features of sEPSCs changed after SCI, we compared the amplitude (Figure 3.3A) and time constants (Figure 3.3B,C) of fitted sEPSCs in SCI and control mice. Parameters were obtained from non-overlapping sEPSCs using a template function (see Methods). Amplitudes of sEPSCs were significantly and similarly larger at both 3

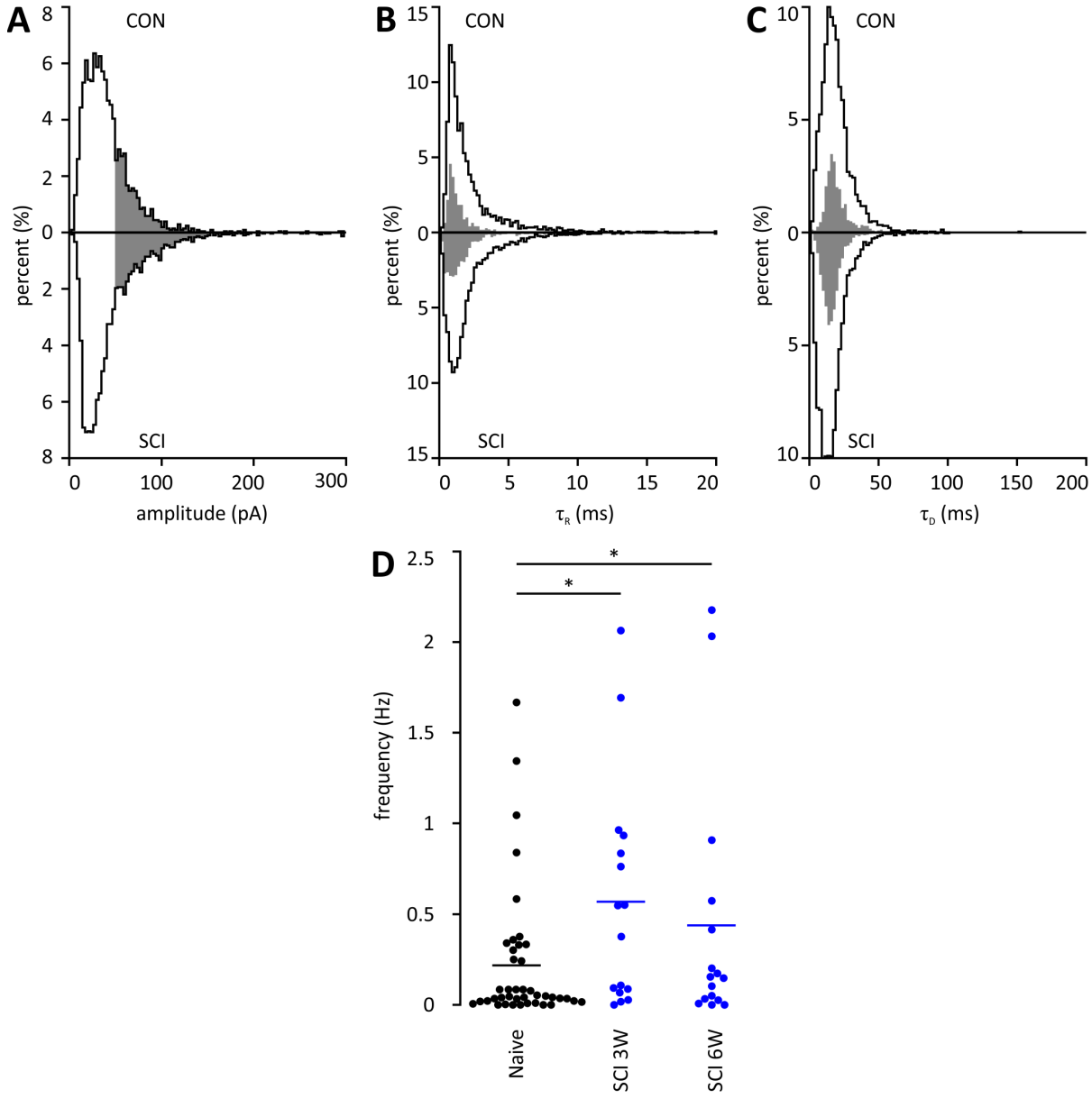

Figure 3.3 Effect of SCI on spontaneous synaptic activity
A, Histogram of sEPSC amplitudes in control (top) and SCI (bottom) mice. B, Histogram of fitted rise time constant in control (top) and SCI (bottom) mice. C, Same a B for decay time constant. In A-C, gray region indicates events with amplitude > 50pA. D, Comparison of sEPSC frequency in naïve (black) and SCI mice (blue) at 3 and 6 weeks post-injury.

and 6 weeks after SCI (15% increase). Though τ_R was unchanged after SCI, τ_D was similarly and significantly decreased at both 3 and 6 weeks after SCI (17% decrease). We compared time constant values of large (>50pA) versus small (<50pA) amplitude sEPSCs to see if there was a systematic relationship between amplitude and time constant. In all cases, the larger amplitude values had a lower standard deviation, likely the effect of noise on the accuracy of the fitting algorithm. Though mean τ_D did not differ between small and larger amplitude events, τ_R was significantly shorter in the larger events. This likely reflects the kinetic relationship between amplitude and rise-time in EPSCs, as larger amplitude EPSCs tend to rise to their maximal value much faster in kinetic simulations (Edelstein et al., 1996).

A change in the frequency of sEPSCs would be indicative of presynaptic compensatory changes (Queenan et al., 2012). In order to identify possible presynaptic homeostatic regulation, we calculated mean sEPSC frequency for cells from control mice and from mice 3 weeks and 6 weeks after SCI. Mean spontaneous synaptic frequency roughly doubled in both SCI time points (Figure 3.3D). This could indicate that within 3 weeks after SCI, there are more synapses, that individual synapses become more active, or a combination thereof. This reorganization is maintained at least to the 6 week time point.

3.3.4 *Effect of TTX on sEPSC frequency*

sEPSCs may arise as a result of spontaneous action potentials (APs) in presynaptic axons or by purely synaptic mechanisms (Kavalali, 2015). To determine if sEPSCs were due to spontaneous APs, we blocked AP-dependent synaptic transmission by applying tetrodotoxin (TTX) and monitored current steps to ensure action currents disappeared (Figure 3.4A). In 7 cells from

	Control	SCI: grouped	3W	6W
Amp., pA	38.6±30.1 (2386)	44.4±37.9 (3052)**	45.0±42.6 (1335)**	44.0±33.8 (1710)**
τ_r, ms	2.2±2.2 (2386)	2.2±2.1 (3052)	2.3±2.5 (1335)	2.1±1.7 (1710)
<50pA	2.4±2.3 (1835)†	2.4±2.2 (2175)†	2.5±2.6 (982)†	2.3±1.9 (1186)†
>50pA	1.5±1.3 (551)†	1.7±1.7 (877)*†	1.6±2.1 (353)†	1.8±1.3 (524)*†
τ_d, ms	19.6±11.6 (2386)	16.3±9.8 (3052)**	16.8±10.5 (1335)**	15.9±9.1 (1710)**
<50pA	19.5±12.2 (1835)	16.1±10.3 (2175)**	16.7±10.8 (982)**	15.6±9.8 (1186)**
>50pA	20.1±9.5 (551)	16.8±8.3 (877)**	17.0±9.7 (353)**	16.7±7.2 (524)**
Incidence	40/41	32/32	16/16	16/16
f, Hz	0.22±0.38 (41)	0.50±0.65 (32)*	0.57±0.62 (16)*	0.43±0.70 (16)

Table 3.1 Comparison of synaptic properties before and after spinal cord injury
Values are presented as mean±SD (n). n for amplitude and time constants is for total number of synaptic events. Significance was calculated by one-way ANOVA followed by Welch's test of unequal variance. n for incidence of spontaneous activity and firing frequency is number of cells. For firing frequency, significance was determined by the Kruskal-Wallis test followed by Mann-Whitney U test.; <50pA and >50pA, considers only events smaller and larger than 50pA in amplitude. Asterisks, values differ significantly from control; *, $p<0.05$; **, $p<10^{-5}$. †, small and large events differ significantly at $p<10^{-5}$.Amp., amplitude; τ_r, rise time constant; τ_d, decay time constant; *f*, frequency.

control mice, 6 had a low sEPSC frequency (<0.5Hz). Of these, no sEPSCs were observed in 2 cells after TTX. In the one cell with high sEPSC frequency (>1Hz), frequency was maintained after TTX application. TTX was also added to 4 cells from SCI mice: three in the 3-week group and one in the 6-week group. In the 3-week group, none of the cells had many sEPSCs before, and only one had any sEPSCs after TTX. The one cell in the 6-week group had a sEPSC frequency which varied somewhat over time, but which remained very high both before (>1Hz) and after (>2Hz) TTX application (Figure 3.4B,C). Overall, it seems likely that most and perhaps all sEPSCs in thoracic ganglia are AP-independent unitary synaptic events comparable to mini EPSCs (Kavalali, 2015; Gonzalez-Islas et al., 2018).

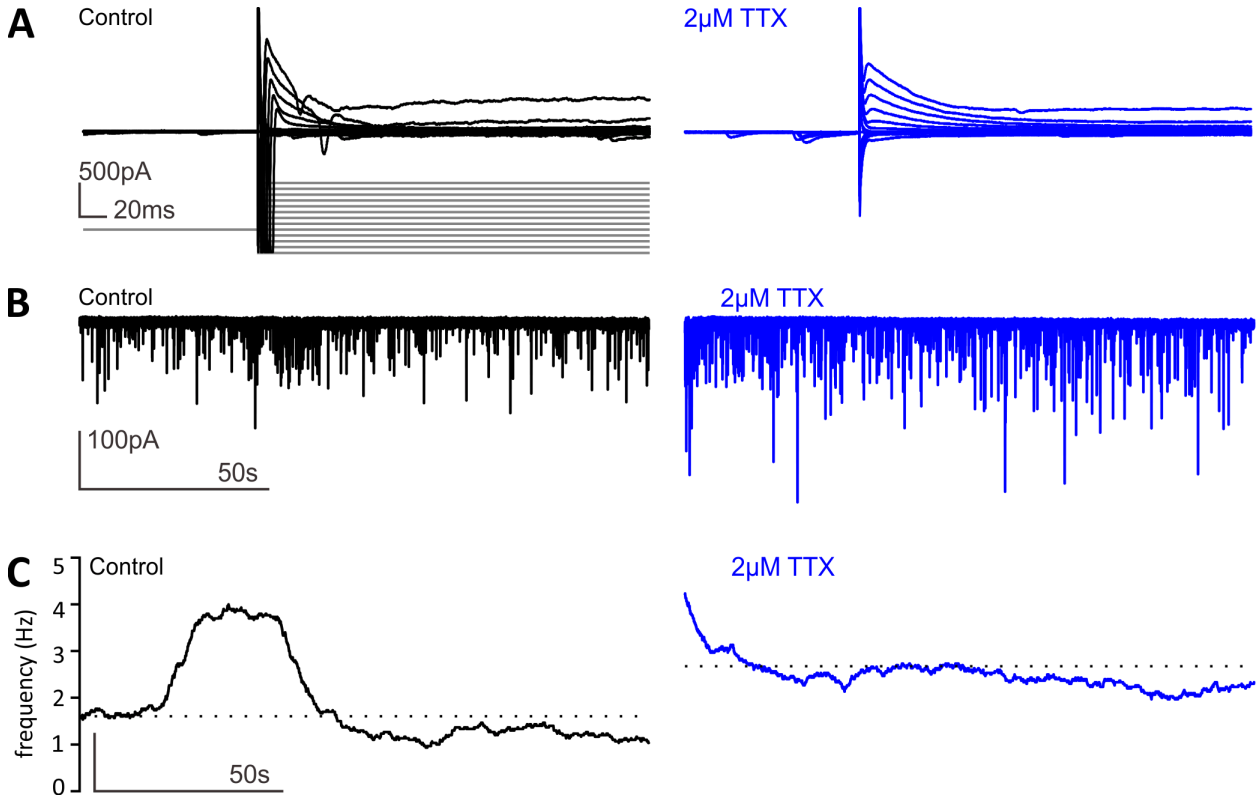

Figure 3.4 sEPSCs are insensitive to TTX
A, Voltage clamp trace from a SCI cell before (black) and after application of 2μM TTX (blue). At this concentration, note that fast sodium current is completely blocked. B, Trace from the same cell in A before and after application of TTX. Note that spontaneous events persist after TTX application. C, Instantaneous frequency over time using 30s sliding window method in the same cell.

3.4 **Discussion**

In this chapter, we explored the synaptic properties of tSPNs in control and SCI mice. We found that nearly all cells exhibit sEPSCs. The frequency of sEPSCs is highly variable between cells, but less variable within a given cell. We then compared the amplitude of sEPSCs to evoked events and found that in some cells they had comparable amplitudes, while in others the amplitude of eEPSCs was much greater. We then identified changes in synaptic properties that occur after SCI. We found that overall frequency of synaptic events roughly doubles. There was also a modest but significant increase in amplitude and a shortening of decay time constant. This lead to larger and shorter sEPSCs after SCI. Finally, we determined that most if not all sEPSCs

are AP independent by showing that frequency of sEPSCs does not decrease after application of TTX.

3.4.1 *Spontaneous events in thoracic neurons*

Nearly all postganglionic neurons exhibited some degree of spontaneous activity, agreeing with prior recordings in thoracic ganglia (Blackman and Purves, 1969). The overall frequency of synaptic events was highly variable between cells, with some cells displaying sustained frequency of over 0.5Hz and several displaying less than one event per minute. The recordings presented in the present study are taken from a heterogeneous population of neurons, but it is uncertain what leads to variability between cells. In recordings of postganglionic neurons *in vivo*, firing properties of neurons vary depending on their neuroeffectors (Jänig, 2006), with cutaneous vasoconstrictors maintaining a higher ongoing firing rate than pilomotor neurons, for example. It may be that this difference in ongoing activity is correlated with difference in spontaneous activity in postganglionics *in vitro*. Additionally, there are several molecularly defined subtypes identified in mouse thoracic ganglia (Furlan et al., 2016) which could receive unique amounts of presynaptic innervation. It is possible that these variables contribute to the range of presynaptic frequencies observed.

In addition to variability between cells, we also observed that spontaneous frequency varied over time within a single cell. In one study, frequency of spontaneous events was increased in the isolated rabbit SCG by increasing osmotic pressure or concentration of K^+ (Ivanov et al., 1975). However, this study found that TTX blocked these effects, which indicates that the aforementioned mechanisms likely correspond to spontaneous AP generation and are therefore

not likely to be the cause of variable frequency within mouse tSPNs. We determined that sEPSCs persist in the presence of TTX at approximately the same frequency, indicating that most if not all sEPSCs in tSPNs are AP independent.

We found the average sEPSC amplitude at −90mV to be 40pA. Assuming a reversal potential around 0mV (Springer et al., 2015), this corresponds to a maximal conductance of 0.44nS, which is an order of magnitude lower than the mean peak conductance of sEPSCs reported in rat SCG (Sacchi et al., 2006). This discrepancy may be due to difference in species or recorded ganglion. The only other study of which we are currently aware that published voltage-clamp recordings in mouse tSPNs reported only 2 sEPSCs (Jobling and Gibbins, 1999). These appear to have amplitudes between 0.1 and 0.2 nA, and an estimated peak conductance of ~1.6nA. However, it must be noted that this does not represent the mean value, but rather the only sEPSCs visible from the reported traces. It is therefore likely that 0.44nS is an accurate estimate of the mean peak conductance of mouse tSPN sEPSC magnitude.

The time constants of rise and decay were approximately 3-5 times longer than those reported in the literature for α3β4 EPSCs in sympathetic ganglia at body temperature (Cassell and McLachlan, 1986; Sacchi et al., 2006) but agree well with reports at room temperature (Bobryshev and Skok, 2002). The kinetics of nicotinic receptors channel openings and closings are highly temperature dependent, with Q_{10} values of 3.0 in bullfrog sympathetic ganglia (MacDermott et al., 1980) and 3.7 in rabbit SCG (Derkach et al., 1983). If nicotinic receptors in mouse tSPNs have a similar Q_{10}, the τ_D at body temperature would be ~4.1ms, in better

agreement with prior reports in lumbar sympathetic chain of the guinea pig at 35°C (4.9ms, cf. Cassell and McLachlan, 1986).

3.4.2 *Evoked events may reveal degree of innervation*

Spontaneous and evoked EPSCs are independent of each other and activate postsynaptic neurons via distinct pathways (Kavalali, 2015). It is therefore possible that sEPSCs are active *in vivo*, and may contribute to the on-going activity of tSPNs. The mean amplitude of sEPSCs can be used as an estimate of mean quantal size (Sacchi and Perri, 1971; McLachlan, 1975). By this reasoning, the ratio of the mean amplitude of sEPSC to eEPSC might be used as a measure of the degree of innervation available to recruit postganglionic neurons. The present study determined that the ratio of eEPSC amplitude to mean sEPSC amplitude ranges from ~2.7 to 27. The higher end of this range far exceeds the estimates of ~5 synaptic inputs to thoracic neurons reported in prior studies (Purves et al., 1986; Jobling and Gibbins, 1999). This may indicate that sEPSCs represent spontaneous activation of a single bouton, while eEPSCs represent axonal recruitment of multiple boutons. Baskets of cholinergic boutons have been observed surrounding some mouse tSPNs (Jobling and Gibbins, 1999; Gibbins et al., 2000) and it has been suggested that primary inputs are the result of a relatively high number of boutons originating from a single axon (Gibbins et al., 1998; Murphy et al., 1998). At the other end of the spectrum is the observation in all 4 cells that some eEPSCs are of a similar magnitude to unitary sEPSCs. eEPSCs are dependent upon axonal recruitment so the smaller evoked events may represent axons that provide secondary inputs with relatively few synaptic boutons. This must be interpreted cautiously, as we cannot be certain that all preganglionic inputs were optically recruited; ramus stimulation would omit inputs coming from different segments, axons may not be recruited

reliably, and there may be high-threshold axons that are unable to be recruited by the highest stimulus intensity used.

3.4.3 *Spontaneous synaptic activity after spinal cord injury*

Following SCI, a number of changes were observed in the properties of sEPSCs in tSPNs. Most striking was the doubling of sEPSC frequency, indicative of a compensatory homeostatic mechanism which restores presynaptic drive after injury-induced reduction in preganglionic input (Queenan et al., 2012). Two potential mechanisms for this increase in frequency are considered here. First, it may be the result of synaptic sprouting. Preferential formation of primary synapses after nerve transection in guinea pig lumbar ganglia has been reported (Ireland, 1999). Damage to preganglionic neurons within the spinal cord would reduce preganglionic input to postganglionic neurons and may lead to a similar reorganization and primary synapse formation. If primary synapses are indeed comprised of a single axon with many boutons (Gibbins et al., 1998; Murphy et al., 1998), preferential formation of primary synapses would be consistent with an increase in the number of sEPSCs observed. Second, doubling of sEPSC frequency may be due to the increased frequency of events occurring at individual synapses. The rate of spontaneous release is proportional to the intracellular Ca^{2+} levels, so any mechanism that would lead to elevated [Ca^{2+}] at the synapse would be consistent with increased sEPSC frequency. A possibility is the up-regulation of R-type Ca^{2+} channels, shown to be largely responsible for spontaneous release (Ermolyuk et al., 2013; Kavalali, 2015) and present in both primary and secondary synapses (McLachlan, 2003). This may be a homeostatic response to the reduced preganglionic drive after high SCI (Teasell et al., 2000).

We observed a ~10% increase in the mean amplitude of sEPSCs. A change in the amplitude of sEPSCs after SCI may be indicative of presynaptic or postsynaptic mechanisms (Turrigiano et al., 1998; Queenan et al., 2012; Turrigiano, 2012). Potential mechanisms that would lead to an increased amplitude include an increase in quantal content of presynaptic neurons (Turrigiano et al., 1998), or postsynaptic up-regulation of nAChRs (Turrigiano et al., 1998; Queenan et al., 2012; Turrigiano, 2012; Gonzalez-Islas et al., 2018). The latter may represent synaptic scaling, a form of homeostatic regulation. In short, loss of presynaptic input and the resultant loss in neuronal output lead to compensatory scaling of synaptic amplitude. Scaling adjusts the amplitude of synaptic input, thereby restoring neuronal output. Importantly, this scaling can also occur as a result of loss of AP-independent spontaneous synaptic input onto the postsynaptic neuron, leading to sEPSC-mediated increase in synaptic amplitude in an effort to restore pre-injury levels of input. The observation of increased sEPSC amplitude is not likely to be the result of primary synapse formation. sEPSCs persist after TTX application so they are independent of APs and represent spontaneous release at a single bouton rather than coordinated release by multiple boutons.

sEPSCs after SCI were shown to have a shorter τ_D. The decay time constant of the EPSC represents the mean duration of single nAChR channel opening (Skok, 2002). The kinetics of nAChRs in autonomic ganglia are relatively insensitive to the many second messenger systems known to influence other groups of ligand-gated receptors (Voitenko et al., 1998; Skok, 2002). While nAChRs of the α3β4 subtype are most common in sympathetic ganglia (Del Signore et al., 2004), several other subtypes with unique decay kinetics are also present in control tSPNs and other autonomic ganglia (Skok, 2002; Furlan et al., 2016). Therefore, the change in decay time

may indicate a change in the relative expression of different channel subtypes, though further studies would be required to verify this.

4 General conclusions and future directions

4.1 Conclusion

The thoracic region of the sympathetic chain is uniquely positioned to modulate sympathetic transmission from the central nervous system to peripheral effectors. Understanding the role that the thoracic chain plays in homeostatic regulation in healthy and spinal cord injured animals is of critical importance, but the region is understudied. This dissertation provides a characterization of intrinsic and synaptic properties of thoracic neurons both before and after spinal cord injury.

4.1.1 *Summary of results*

We developed a technique to acquire whole-cell recordings from intact thoracic ganglia and used these recordings to develop a single-cell computational model of thoracic neurons. Using these techniques, we characterized the intrinsic and synaptic properties of thoracic neurons.

We first sought to characterize the intrinsic and firing properties of thoracic neurons. We determined that tSPNs exhibit considerable diversity in values of RMP. We further found a strong correlation between R_{in} and τm, and established that values recorded with whole-cell patch clamp are on average an order of magnitude larger than prior microelectrode recordings. A major consequence of this was the increased size and duration of sEPSPs in both physiological and computational neurons. We then moved on to characterization of recruitment principles of tSPNs. We found that input conductance is a major contributor to, but not the final arbiter of, cell excitability (*i.e*. rheobase current). Computational modeling studies showed that rheobase is substantially increased, and excitability therefore decreased, by the impalement injury introduced by microelectrode recordings.

From recruitment we moved on to characterization of firing properties. We demonstrate that firing rate has an approximately linear relation with injected current magnitude. This contradicts the prevailing viewpoint, which holds that thoracic postganglionics are only capable of sustaining short bursts of action potentials. We showed that, once again, this discrepancy is due to the leak introduced by microelectrode injury. We further showed through computational modeling that tSPNs are especially susceptible to microelectrode injury as a result of M-type potassium current. We also showed that firing rate decreases over time in response to a constant current injection. Based on computational modeling, we showed that this spike-rate adaptation was dependent upon M-type and Ca^{2+}-dependent potassium currents.

We identified two (possibly three) classes of repetitively firing neurons based on the difference between the initial AP height and subsequent spikes. The two classes differed significantly in parameters related to AP shape, likely indicating that sodium channel expression differs between firing classes. We also characterized three types of afterhyperpolarization: a fast, slow, and ultra-slow. The fast component was observed after single APs and was moderately correlated with τ_m and maximal firing rate. The sAHP was observed after spike trains and was correlated with spike rate adaptation, indicating the likely involvement of I_M and I_{KCa}. The usAHP was rarely observed, but was associated with progressive hyperpolarization of neurons in response to depolarizing current. We used the computational model to explore potential contributions of various conductances to phenomena observed in recorded neurons. We attributed an initial notch upon depolarization to I_A. A voltage sag upon deep hyperpolarization was attributed to I_H. A

voltage sag in response to moderate hyperpolarization and subsequent rebound firing was attributed to I_M.

We then characterized spontaneous synaptic activity in tSPNs. Nearly all neurons exhibited some degree of spontaneous activity, but the mean frequency was highly variable between cells. In individual cells with relatively high firing rate, frequency also varied over time. Amplitudes within a single cell were also variable and occupied a large, continuous range. These sEPSCs were insensitive to TTX, so they are likely comparable to spontaneous mini-EPSCs. We compared evoked EPSCs to sEPSCs and found that in some cells amplitudes were comparable. In others, eEPSC amplitude occupied a nearly 30-fold range that included the sEPSC range and extended to much larger values. Overall this suggests that there are some postganglionic neurons with very few synapses, but that others receive input from many synapses of varying amplitudes.

Finally, we compared intrinsic and synaptic properties in tSPNs before and after SCI. We found that there were no significant differences in any intrinsic membrane properties. However, after SCI we detected changes in the amplitude and frequency of sEPSCs, which may represent homeostatic regulation to restore pre-injury levels of synaptic drive.

4.1.2 *Consequence of enhanced excitability of tSPNs*

The electrophysiological properties of postganglionic neurons in thoracic ganglia (Blackman and Purves, 1969; Lichtman et al., 1980; Jobling and Gibbins, 1999) have not been as extensively characterized as those in other paravertebral ganglia (Eccles, 1935; Erulkar and Woodward, 1968; Purves and Wigston, 1983; Jänig, 1985; Cassell et al., 1986; Valli et al., 1989; Li and

Horn, 2006; Bratton et al., 2010; Springer et al., 2015). All prior studies in thoracic ganglia relied on microelectrode recordings, which considerably reduce the input resistance (R_{in}) and time constant (τ_m) of neurons (Staley et al., 1992; Springer et al., 2015). It is clear from our recordings that prior reports of passive membrane properties in thoracic ganglia were substantially underestimated as a direct consequence of recording method (Blackman and Purves, 1969; Jobling and Gibbins, 1999). In the present study, whole-cell recordings preserved passive membrane properties and led to an increase in R_{in} and τ_m and a reduction in rheobase compared to prior reports, indicating that tSPNs are far more excitable than previously envisioned.

This increased excitability has important implications for the physiological relevance of secondary synapses. It is well established that most postganglionic neurons receive a single primary input which always leads to cell recruitment, and a few secondary inputs with lower amplitude, an organization scheme termed the n+1 rule (Karila and Horn, 2000; McLachlan, 2007). The number of secondary synapses varies by species and ganglion (Ivanov and Purves, 1989), but mouse thoracic postganglionic neurons receive ~5 secondary synapses (Jobling and Gibbins, 1999). Secondary synapses were not traditionally thought to contribute to firing (McLachlan et al., 1998; Karila and Horn, 2000; McLachlan, 2003; Wheeler et al., 2004; Rimmer and Horn, 2010), but more recent work has suggested that secondary synapses may play a role in sympathetic recruitment (Bratton et al., 2010; Springer et al., 2015). By preserving the passive membrane properties of tSPNs, we show that sEPSPs have a greater amplitude and duration than microelectrode recordings would suggest. This echoes findings in rat SCG (Springer et al., 2015). An increase in the amplitude of subthreshold synaptic events could directly alter the firing rate of postganglionics. Postganglionic neurons receive both sub- and

suprathreshold input in a continuous range that overlaps the firing threshold (Bratton et al., 2010). An overall increase in the postsynaptic response to secondary input would lead to a higher proportion of suprathreshold events, thereby increasing the on-going activity of postganglionic neurons *in vivo* (Bratton et al., 2010).

A longer duration for secondary EPSPs could also lead to summation of synaptic events, provided that 2 or more events of sufficient size occur within a defined temporal window (Skok, 1973; Konig et al., 1996; Ratte et al., 2013). Preganglionic neurons typically have a low firing rate *in vivo*, so summation of synaptic events is not thought to contribute substantially to postganglionic recruitment (North, 1986; McLachlan et al., 1997; McLachlan, 2003; Jänig, 2006). However, others have proposed that during states of high frequency synaptic drive, postganglionic neurons act as frequency-dependent gain amplifiers (Karila and Horn, 2000; Horn and Kullmann, 2007). Given the wide range of frequency of spontaneous events that we observe, synaptic integration and the resultant gain in firing frequency could be highly relevant in certain cells and virtually non-existent in others.

Another consequence of preserved passive membrane properties was the observation that tSPNs are capable of repetitive firing. For decades, the prevailing viewpoint held that paravertebral neurons were capable of firing APs only in short bursts in response depolarizing current (Jänig, 1988; Jobling and Gibbins, 1999; Jänig, 2006), but again these results are based on microelectrode recordings. A recent study showed that when passive membrane properties are preserved by using whole-cell recordings, SCG neurons are capable of repetitive firing (Springer et al., 2015). We reached the same conclusion in thoracic ganglia, and additionally used a

computational model to demonstrate that M-type potassium current was responsible for paravertebral neuron firing properties' susceptibility to microelectrode-induced leak. The role of I_M in modulating firing properties of postganglionic neurons has been established previously (Brown and Adams, 1980; Brown and Constanti, 1980; Cassell et al., 1986; Luther and Birren, 2009).

4.1.3 *Benefits of computational modeling*

Throughout this project, electrophysiological recordings have been used to inform a conductance based computational model, and the computational model in turn was used to inform the interpretation of electrophysiological recordings. This model proved to be an invaluable tool for rapidly answering mechanistic questions. In several instances, we used the model to generate hypotheses and identify candidate currents responsible for the various phenomena observed in tSPNs. Perhaps the most interesting finding was the interaction between I_M and I_{imp} with respect to repetitive versus phasic firing. It has been suggested that impalement conductance introduced by microelectrode recordings is responsible for the observation that paravertebral neurons fire phasically in response to sustained current injection (Springer et al., 2015), but repetitive firing is observed in other autonomic neurons (*e.g.* celiac ganglion neurons) when recorded using microelectrodes (Jobling and Gibbins, 1999). What is the unique feature of paravertebral neurons that makes them so susceptible to microelectrode leak? From our computational model, we determined that I_M was primarily responsible for tSPNs unique susceptibility to microelectrode leak. We showed this by demonstrating that phasic firing was no longer possible, regardless of impalement conductance, if I_M was removed from the model. Prior studies have implicated I_M in the interconversion of repetitive and phasic firing neurons (Brown and Adams, 1980; Brown and

Constanti, 1980; Cassell et al., 1986; Luther and Birren, 2009), but the computational model allowed us to quickly establish a mechanistic link between I_M, I_{imp}, and repetitive firing properties.

After establishing that tSPNs can fire repetitively, we characterized the firing frequency as a function of time and injected current magnitude. We found that firing frequency increased linearly with injected current (f-I curves) and decayed as a function of time (spike rate adaptation). The computational model was able to reproduce these dynamic firing features, and allowed us to probe some of the underlying mechanisms. We initially hypothesized that input resistance was a major contributor to the f-I slope given the correlation between the two values. However, the computational model suggested that there was no causal link between the two values and the correlation might be coincidental. We then looked at factors that may contribute to SRA, and found that both I_M and I_{KCa} were capable of reproducing the fast and slow components of SRA. These currents have been implicated in SRA in other cell types (Sawczuk et al., 1997; Powers et al., 1999; Miles et al., 2005; Yi et al., 2015), and our computational model allowed us to rapidly test for this relationship in tSPNs without the need to record firing properties in the presence of ion channel blockers.

We used our computational model to establish that the notch at the beginning of depolarizing traces was due to I_A, a phenomenon observed previously in mouse tSPNs and similarly attributed to I_A (Jobling and Gibbins, 1999). The model also showed that the sag observed upon hyperpolarization was due to a combination of I_H and I_M, agreeing with prior reports in tSPNs (Jobling and Gibbins, 1999) and SCG (Cassell et al., 1986) and that rebound firing was due

primarily to I_M, agreeing with prior observations in cortical neurons (Constanti and Galvan, 1983). All of these observations were made without the need for bath application of ion-channel blockers, greatly expediting this research.

Finally, we combined our own recordings of synaptic events with an established synaptic conductance template (Springer et al., 2015) to explore the impact that leak conductance can have on synaptic integration. By adjusting model parameters, we were able to show temporal summation of subthreshold synaptic events could lead to cell recruitment, lending credibility to the idea that secondary synapses can be active participants in the output properties of thoracic ganglia (Karila and Horn, 2000; Jänig, 2006; Horn and Kullmann, 2007).

4.1.4 *Consequence of spinal cord injury on postganglionic neuron function*

Spinal cord injury leads to dramatic reorganization within the spinal cord (Karlsson, 1999; Hou and Rabchevsky, 2014), altering the excitability of sympathetic preganglionic neurons which innervate postganglionic neurons. SCI can also increase the responsiveness of peripheral adrenoceptors, thereby increasing the strength of the vasomotor response to postganglionic activity (Innes and Kosterlitz, 1954; Mathias et al., 1976; Rummery et al., 2010; Tripovic et al., 2010; Tripovic et al., 2011). Several studies have characterized re-innervation of sympathetic ganglia following transection of preganglionic axons in peripheral nerves (McLachlan, 1974; Njå and Purves, 1977b; Njå and Purves, 1978; Ireland, 1999; Serebryakova, 2008), but we are not aware of any studies that have specifically characterized reorganization within paravertebral ganglia after SCI. We explored and characterized intrinsic and synaptic properties of tSPNs in order to determine if any changes occur as a result of SCI. We found that overall, passive

membrane properties and intrinsic excitability of tSPNs were unchanged between groups. However, in this population there is evidence that SCI leads to differences in the incidence or magnitude of individual voltage-gated ion channels (Li et al., in preparation), so compensatory homeostatic mechanisms may have been invoked after injury to return excitability to a level seen in uninjured mice.

In comparison, differences in synaptic properties were observed after SCI. Notably, the frequency of spontaneous synaptic activity doubled. This may indicate an increase in synaptic sprouting similar to what is observed in the spinal cord after SCI (Hou et al., 2008; Hou et al., 2009; Hou and Rabchevsky, 2014) and in paravertebral ganglia after nerve transection (Njå and Purves, 1977b; Ireland, 1999). It may also indicate the upregulation of Ca^{2+} channels (*e.g.* R-type) at presynaptic cites, leading to an increase in the frequency of sEPSCs at individual boutons (Ermolyuk et al., 2013; Kavalali, 2015). We also observed a slight increase in the amplitude of sEPSCs, which may suggest homeostatic synaptic scaling at individual synapses (Turrigiano, 2012; Gonzalez-Islas et al., 2018). It may also reflect the preferential formation of primary synapses (Ireland, 1999) as primary synapses have a higher quantal content than secondary synapses (McLachlan, 1975). SCI also led to a decrease in the decay time-constant of sEPSCs, possibly indicating differential expression of nAChR subtypes (Skok, 2002; Furlan et al., 2016), but unlikely a reflection of receptor modification by secondary messengers (Voitenko et al., 1998; Skok, 2002).

4.2 **Future directions**

Any study that seeks to understand an underexplored region will inevitably raise more questions than it answers. This study was no exception, and some of the more interesting questions raised are provided below.

4.2.1 *Is there a correlation between cell type and firing properties?*

There are known to be several molecularly distinct subpopulations in thoracic ganglia (Furlan et al., 2016), and we have shown that there may be functionally distinct groups based on intrinsic membrane properties. Is there a correlation between these molecularly and functionally defined subtypes? Intracellular dye-filling could help to answer this question. One could include a fluorophore in the patch electrode, record electrophysiological properties, and subsequently immersion fix the tissue and perform immunohistochemistry. Jobling and Gibbins (1999) performed each of these maneuvers separately (electrophysiological recording, intracellular dye filling, and immunohistochemistry), but no attempt was made to correlate electrophysiological properties to immunohistochemical data. It would therefore be useful to perform all maneuvers in the same cell to determine if any correlations exist.

4.2.2 *Impact of SCI-induced changes on cell recruitment?*

We have established that there are changes in the frequency, amplitude, and decay kinetics of spontaneous synaptic events in tSPNs after SCI. Do these changes in input have a physiologically relevant impact on the activity of tSPNs in vivo? Answering this question directly would be difficult, but combining the computational model developed in Chapter 2 with the changes observed in Chapter 3 would be feasible and relatively straightforward.

4.2.3 *Computational model of individual cells?*

The computational model presented herein is based on generalized models of ionic currents known to be present in paravertebral neurons, and no effort was made to tailor the model to the specific subtypes present in thoracic neurons. A recent study reported RNA transcript levels in tSPNs (Furlan et al., 2016). By correlating transcript number to maximal conductance of various molecularly defined ion channel subtypes (Schulz et al., 2006), we could tailor a computational model to an individual cell based on its unique ion channel expression, similar to efforts already undertaken in crustacean neurons (Northcutt et al., 2016).

4.2.4 *Impact of SCI on evoked synaptic events?*

We have established that sEPSCs and eEPSCs occupy overlapping amplitudes, but that eEPSCs tend to be larger and likely reflect the recruitment of multiple synaptic boutons. The difference could indicate the amount of synaptic innervation received by a single neuron. It would be interesting to see if this relationship changes after SCI.

In conclusion, my dissertation has provided valuable insight into the physiological function of tSPNs both before and after spinal cord injury, and I have created methods and a computational model that will be useful to future researchers aiming to further study this system.

5 Methods

5.1 Animals

All animal procedures were performed in accordance with the Emory University Institutional Animal Care and Use Committee's regulations and conformed to the Guide for the Care and Use of Laboratory Animals. Experiments were performed on adult (P37-379) C57BL/6 mice (RRID:IMSR_JAX:000664). Mice were anesthetized with inhaled isoflurane and maintained or killed with urethane (i.p. injection, 40mg/kg for transcardial perfusions, ~500mg/kg for *in vitro* electrophysiology). Complete sedation or death was confirmed by lack of foot pinch and eye blink reflex.

5.2 Spinal cord injury

Mice were anesthetized in a chamber containing 5% isoflurane. Dorsal skin was shaved and the animal was returned to the induction chamber with isoflurane level reduced to 1.5%. The mouse was then placed in a nose cone dorsal side up for the duration of the procedure. Incision site was sterilized with betadine and isopropyl alcohol. In incision was made above the T2-T3 vertebrae. Intervening fat and muscle was displaced to allow access to the vertebral column. Bone scissors were then used to perform a dorsal vertebrectomy at the T2-T3 level to expose the spinal cord. The cord was then transected with surgical scissors. Hemostatic gauze was inserted between transected sections to prevent bleeding. The incision was closed using surgical adhesive. Mice were given 0.3 mg/kg buprenorphine as an analgesic and allowed to recover alone in a home cage. Bladders were manually voided twice daily as necessary until bladder function recovered. Mice were allowed to survive for 3 or 6 weeks. These time points were chosen to coincide with onset of symptoms of autonomic dysreflexia.

5.3 **Immunohistochemistry**

5.3.1 *Neurotransmitter identity*

Two ChAT-eGFP mice (RRID:IMSR_JAX:007902), a male and a female (P91 and P101, respectively) were anesthetized and transcardially perfused with heparinized saline (0.9% NaCl, 0.1% $NaNO_2$, 10units/mL heparin), followed by 4% paraformaldehyde (0.5M phosphate, 4% paraformaldehyde, NaOH). Tissue was post-fixed overnight, then transferred to a 15% sucrose solution and stored at 4°C. Sympathetic chains were isolated from stellate (T1 and T2) to T12/13. Tissue was embedded (TissueTek® optimal cutting temperature compound), sectioned on a cryostat (−21°C, 8µm slice thickness), and mounted on glass slides. Tissue was washed in 0.1M phosphate buffered saline (PBS) for one hour and permeabilized with PBS containing 0.3% Triton X-100 (PBS-T) overnight. Sections were subsequently incubated for 2-3 days with primary antibodies: sheep anti-Tyrosine Hydroxylase (Millipore, 1:100, RRID:AB_90755) and chicken anti-green fluorescent protein (Jackson, 1:100). Preparations were then washed in PBS-T 3 x 30 min) and incubated for 1.5 hours with secondary antibodies: Cy3 donkey anti-sheep (Abcam, 1:250) and Alexa 488 donkey anti-chicken (Abcam, 1:250). Slides were washed a final time in PBS-T (20 min), then 50mM Tris-HCl (2 x 20 min) and allowed to dry before being coverslipped (SlowFade® Gold antifade reagent with 4',6-diamidino-2-phenylindole (DAPI)). Sections were visualized under a fluorescent microscope (Olympus BX51). Cells with visible nuclei were counted and assessed for neurotransmitter identity. Inter-animal cell count variability was substantial (6,494 vs. 19,721 cells).

5.3.2 *Cell diameter*

Six C57Bl/6J mice (RRID:IMSR_JAX:000664), 5 males and one female (all ~P60) were transcardially perfused, as above. T5 Sympathetic ganglia were isolated. Unmounted tissue was washed in PBS-T overnight. Slides were subsequently incubated for 5 days with sheep anti-Tyrosine Hydroxylase (Millipore, 1:100, RRID:AB_90755). Preparations were then washed in PBS-T (3 x 2 hours) and incubated for 3 days with Alexa 488 donkey anti-sheep (Jackson, 1:100). Slides were washed a final time in PBS-T (2 hours), then 50mM Tris-HCl (2 x 1 hour). Intact ganglia were mounted on glass slides and coverslipped (SlowFade® Gold antifade reagent with DAPI). TH-immunoreactive cells were visualized under a fluorescent microscope (Olympus BX51, 40X objective) using a Microfire digital camera (Optronics, Santa Barbara, CA), and traced using Neurolucida software (MBF Bioscience, Burlington, VT, RRID:SCR_001775). Cell diameters were calculated as the arithmetic mean of minimum and maximum feret. Diameter was only determined for cells with a discernible perimeter (176±131 cells per ganglion) representing a mean 71% of the total TH^+ cell population (range of 36-95% neurons/ganglia measured). As diameter distributions were comparable between ganglia, the possibility of sampling bias in estimated cell diameter is unlikely. Results are reported as mean ± SD.

5.4 **Electrophysiology**

5.4.1 *Tissue Preparation*

Mice were anesthetized with isoflurane. Once complete sedation was confirmed by lack of foot pinch and eye blink reflex, mice were euthanized with urethane (0.2mL, 50% solution). Dorsal skin was removed to expose the muscle surrounding the spinal column. Two lateral incisions were made from the peritoneal cavity through the ribs and up to the neck. An additional incision

was made through the lumbar spinal column, and the spinal column was then gently lifted upward. Viscera were carefully cut away leaving only spinal column, ribs, musculature, spinal cord, and sympathetic chain. A final cut was made through the cervical spinal cord to separate the tissue. This tissue was washed briefly in oxygenated ACSF to remove blood and hair, and placed in a dissection chamber with ACSF. The preparation was pinned down dorsal side up. Fat, muscle, and connective tissue adherent to the vertebral column were removed, and a longitudinal incision was made through the midline of the dorsal vertebral column, starting at the rostral end. The preparation was then flipped over and pinned ventral side up. The right thoracic chain was always used, as it was more easily accessible. An incision was made between the sympathetic chain and aorta, taking great care to avoid damaging the chain. A second incision was made on the contralateral side to remove the aorta completely and expose the ventral surface of the spinal column. A second longitudinal cut was made on the contralateral side of the vertebral column, leaving the centrum for stability. The two halves of the spinal column were gently separated, and the spinal cord was removed. Finally, the ribs were trimmed short and the lumbar section was cut off just below the thirteenth rib. The remaining tissue incubated at 37°C in continually oxygenated ACSF containing collagenase (20mg type III per 1mL ACSF, Worthington Biochemical Corporation) for 1.5 hours. ACSF used for incubation was buffered with either bicarbonate or HEPES. No difference was observed as a result of incubation buffer. Following incubation, tissue was vortexed to remove adherent fat and washed with ACSF several times to eliminate residual collagenase. The intact sympathetic chain was removed by severing rami, and was then pinned down into a clear Sylgaard recording dish (Figure 5.1A), through which recirculating, oxygenated ACSF was continually perfused.

5.4.2 *Whole-cell recordings*

Whole-cell patch recordings were obtained from postganglionic cells at room temperature. Cells were identified using an upright microscope (Olympus, BX51WI) affixed with a low-light camera (Olympus, OLY-150). Patch electrodes were pulled on a vertical puller (Narishige, PP-83) from 1.5mm outer diameter filamented, borosilicate glass capillaries (World Precision Instruments, stock # TW150F-4) for a target resistance of 5-9MOhms. Signals were amplified using a MultiClamp 700A and digitized at 10 kHz using a Digidata 1322A and Clampex software (Molecular Devices, RRID:SC_011323).

We considered for analysis all cells which displayed clearly defined action potentials upon depolarization by square current steps. Of these, cells were excluded if more than 100pA was required to hyperpolarize a cell to −70mV (indicative of a significant leak), if action potentials appeared stunted (indicative of an incomplete breakthrough), or if membrane potential was highly variable (indicative of improper seal formation). All cells which met these criteria (n = 35) had resting membrane potentials more negative than −50mV and input resistances higher than 200MΩ. All recordings were made in ACSF containing (in mM): NaCl [127.99], KCl [1.90], $MgSO_4 \cdot 7H_2O$ [1.30], $CaCl_2 \cdot 2H_2O$ [2.40], KH_2PO_4 [1.20], glucose [9.99], and $NaHCO_3$ [26.04]. ACSF pH was adjusted to 7.4 after saturation with gas (95%O_2, 5%CO_2) at room temperature. Intracellular patch clamp solution contained (in mM): K-gluconate [140.0], EGTA [11.0], HEPES [10], and $CaCl_2$ [1.32] and pH was adjusted to 7.3 using KOH. Target osmolarity was less than 290 mOsm. In most recordings (25/39 cells), support solution was added consisting of ATP [4.0] and GTP [1.0].

The ratio of male to female mice was approximately 1:1. Recordings were taken from the right thoracic ganglia, with the majority of recordings coming from T5. The number of cells from ganglia T3 through T12 was 2,6,17,3,2,1,1,0,1, and 2, respectively. We initially assessed sex and segment related differences in cell properties. Our sample size precludes a more detailed analysis of segment-specific differences, but we were able to pool data from rostral (T3 and T4) and caudal (T5 to T12) segments (Furlan et al., 2016). Statistical tests revealed no differences with respect to sex or rostro-caudal location (t-test, 2-tailed, unequal variance, Šidák corrected α=0.0019), so all data were pooled for additional analyses.

5.4.3 *Optogenetic stimulation*

Optical stimulation of preganglionic axons was performed on mice expressing channelrhodopsin (ChR2) in cholinergic ($ChAT^+$) neurons. Driver lines were either ChAT-IRES-cre (JAX: 006410) or ChAT-Gsat-GM24-cre. Reporter line used was R26-ChR2-eYFP (JAX: 012569). After tissue was dissected and affixed in the recording chamber, a fiber optic cable was connected to a custom built laser diode control box and the free end aimed at the tissue. Stimulus locus was variable between experiments. Typically, the closer the stimulus locus to the recording site the greater chance of recruitment. These stimulus loci include ventral root, ramus, interganglionic nerve, and ganglion.

5.5 **Data analysis**

5.5.1 *Analysis of intrinsic membrane properties*

All cellular properties were analyzed in Clampfit (Molecular Devices, RRID:SCR_011323) or MATLAB (MathWorks, RRID:SCR_001622). All parameters were estimated from a single set

of current steps for each cell. This ensured that parameters for a given cell were estimated at nearly the same point in time. In current clamp mode, membrane voltage response to hyperpolarizing current steps of at least 1.5 seconds was fit to an exponential of the form [1] using the Levenberg-Marquardt algorithm built in to Clampfit. The value of membrane time constant (τ_m) was calculated in this manner (Golowasch et al., 2009). R_{in} was estimated by dividing maximal voltage deflection (ΔV) by the injected current (I_{inj}) [2]. Membrane capacitance (C_m), a measure of total cell surface area, was estimated by dividing τ_m by R_{in} [3].

$$\Delta V \cdot \exp(-t/\tau_m) + (V_{hold} - \Delta V) \quad [1]$$

$$R_{in} = \Delta V / I_{inj} \quad [2]$$

$$C_m = \tau_m / R_{in} \quad [3]$$

Measured rheobase current (I_{rheo}) was taken as the smallest long-duration (1.5 seconds or longer) positive current injection which elicited a single spike. In the case that an incremental increase in current elicited multiple spikes, rheobase was estimated to be the mean of the adjacent subthreshold and suprathreshold steps, *e.g.* if 30pA did not elicit any spikes but 40pA elicited several, the measured rheobase estimate would be 35pA. In order to achieve a more finely-grained estimate of rheobase, we also calculted rheobase based on the equation:

$$\hat{I}_{rheo} = (V_{th} - V_{hold})/R_{in}$$

where V_{th} is the action potential threshold, taken to be the point at which the first derivative of voltage, dV_m/dt, begins to increase (Platkiewicz and Brette, 2010). Measured values related to action potential (AP) and post-spike afterhyperpolarization (AHP) characteristics were taken from traces elicited at minimal suprathreshold current, *i.e.* the smallest current magnitude used which elicited at least one AP.

The parameters of the fAHP varied as a function of firing rate, so analysis of fAHP properties was limited to cells which fired a single spike at minimal suprathreshold current intensity. Action potential amplitude was defined as the difference between the peak voltage and threshold. AP half-width is the width of the spike at half AP amplitude. Fast afterhyperpolarization (fAHP) amplitude was defined as the difference between peak negative voltage and steady-state voltage at rheobase current injection. fAHP half-decay is the time it takes for the fAHP to decay to half its amplitude. fAHP duration is the time between spike onset and return to baseline (Hochman and McCrea, 1994). Slow afterhyperpolarization (sAHP) amplitude was defined as the difference between peak negative voltage and baseline (holding voltage). sAHP half-decay is the time it takes for the sAHP to decay to half its amplitude. A visual explanation of AP and fAHP parameters is provided in Figure 5.1B

Instantaneous firing rate (IFR) was taken as the inverse of the inter-spike interval. Maximal firing rate was the IFR for the first spike pair at the beginning of current onset. Sustained firing rate was the mean IFR for the last three inter-spike intervals, given they occur during the last half of the depolarizing current step. f-I slope is the slope of the linear regression of the f-I curve. The SRA ratio is defined as the ratio between the maximal and sustained firing rate at a given current injection (Venance and Glowinski, 2003; Miles et al., 2005). In order to directly compare firing rate across cells with variable R_{in} and -I curves, we used the sustained firing rate at twice minimal suprathrechold current injection. Current step duration was at least 1.5 seconds for all cells, and 3 seconds for the majority. Liquid junction potential was calculated to be −9.8mV and empirically measured to be −13mV. All values of absolute voltage (resting membrane potential, absolute threshold, peak voltage) were adjusted by −10mV to approximately account for liquid

junction potential. For example, a recorded AP peak of 30mV would be reported as 20mV and a recorded RMP of −60mV would be reported as −70mV.

5.5.2 *Analysis of synaptic events*

To quantify incidence of sEPSCs, all files associated with a single cell were analyzed for evidence of synaptic events. This analysis included voltage- and current-clamp data and events that occurred during current or voltage steps. If at least one event was observed, the cell was determined to have spontaneous synaptic activity.

To analyze the frequency of sEPSCs, we analyzed the flat regions of voltage-clamp files, excluding the time during voltage steps and any traces after pharmacological agents were added to the perfusing solution. EPSCs were either identified manually or by using a threshold on filtered data. Events detected by the threshold method were later verified by manual inspection. Filter coefficients and threshold were customized to each file, as noise characteristics varied between files. Events were deemed valid if they presented with a sharp increase in inward current followed by a more gradual return to baseline. Total number of events was divided by the total time which met the above criteria to generate a value of sEPSC frequency for each cell.

5.5.3 *sEPSC curve fitting algorithm*

Analysis of amplitude and rise/decay time constant was limited to non-overlapping EPSCs detected at −90mV. Holding current was estimated by taking the mean current for the 10ms preceding optical activation. Amplitude was the difference between peak value and holding

current. Each EPSC was filtered using a Savitzky-Golay filter and fit, using the Levenberg-Marquardt algorithm, to the difference of two exponential functions of the form:

$$I_{syn} = \begin{cases} I_{start} & \text{if } t < t_s \\ \left(Ae^{-(t-t_s)/\tau_d} - Be^{-(t-t_s)/\tau_r} \right) + I_{end} & \text{if } t \geq t_s \end{cases}$$

where t_s is the start time of the event, and τ_r and τ_d are the time constants of rise and decay, respectively, A and B are scaling factors for the decay and rise exponentials, respectively, and I_{start} and I_{end} are the starting and ending currents, respectively. The choice to use separate scaling variables for each exponential and to allow the start and end currents to vary was made to accommodate baseline variability, which often led to inaccurate fitting of events. Separating the exponentials provides a better curve fit and more reliable extraction of EPSC parameters. Fit parameters were then run through a series of goodness-of-fit tests to ensure accuracy. The tests were as follows:

1. |filtered peak current − fit peak current| < 40pA
2. Fit peak current < right half-height current < I_{end}
3. Event start < left half-height time < fit peak time
4. Peak must not be multimodal (no overlapping events)

An example fit with various parameters indicated is presented in Figure 5.1C. This fitting algorithm was developed in collaboration with David Stockton and Astrid Prinz.

5.6 **Computational Modeling**

5.6.1 *Single Neuron Model*

We built a conductance-based neuron model to help understand observed results in relation to their underlying biophysical mechanisms. While tSPNs do possess dendrites, their dendritic

arborizations are relatively simple. We therefore assume that ganglionic cells are electrotonically compact, and that a single-compartment model can replicate all essential physiological properties observed in experiments (Belluzzi et al., 1985). All currents included in the model have been observed in rodent sympathetic ganglia (Galvan and Sedlmeir, 1984; Sacchi et al., 1995; Jobling and Gibbins, 1999; Rittenhouse and Zigmond, 1999) and transcript expression in mouse thoracic ganglia has recently been confirmed by a single-cell RNA-seq study (Furlan et al., 2016).

The model is based on a model of bullfrog paravertebral sympathetic ganglia (Wheeler et al., 2004), which represents the most complete available computational model of a paravertebral neuron. From this model the following conductances were taken: a fast sodium current, I_{Na}; a delayed-rectifier potassium current, I_{Kd}; a slow and non-inactivating potassium current, I_M; and a voltage-independent leak current, I_{leak}. Additional conductances were added from models derived in other species. These include the following: a fast transient potassium current, I_A (Rush and Rinzel, 1995); a hyperpolarization-activated inward current, I_h (Kullmann et al., 2016); and a calcium-dependent potassium current, I_{KCa} (Ermentrout and Terman, 2010). I_{KCa} depends on intracellular calcium concentration, $[Ca^{2+}]$, so a model of persistent calcium current, I_{CaL} (Bhalla and Bower, 1993) and somatic calcium dynamics (Kurian et al., 2011) were added as well. Model parameters were then tuned to fit recorded data from the present study.

The membrane voltage, V, is updated according to the equation:

$$C_m \frac{dV}{dt} = -\sum I_i - I_{input} \qquad [4]$$

Membrane capacitance, C_m, was set at 100pF to approximate the mean in recorded neurons. Each current, $I_{i,}$, is described by the equation:

$$I_i = G_i m^p h^q (V - E_i) \qquad [5]$$

where G_i is the maximal conductance, E_i is the reversal potential, and m and h are gating variables for activation and inactivation. A standard model neuron was used to replicate the majority of observed phenomena. Maximal conductances of this standard neuron are indicated in Table 5.1. The standard model was modified as necessary to fit individual recordings, which comprise a heterogeneous population. The reversal potentials for the various membrane currents are indicated in Table 5.1.

The activation and inactivation variables m and h are updated by the equation:

$$\frac{dx}{dt} = \frac{x_\infty - x}{\tau_x} \qquad [6]$$

The intracellular calcium concentration is updated by:

$$\frac{d}{dt}[Ca^{2+}] = \lambda(-\alpha I_{CaL} - k_{CaS}[Ca^{2+}]) \qquad [7]$$

where λ = 0.01 is the ratio of free to bound $[Ca^{2+}]$, α= 0.002 $uM \cdot ms^{-1} \cdot pA^{-1}$ is the conversion factor from current to concentration, and k_{CaS} = 0.024 ms^{-1} is the somatic $[Ca^{2+}]$ removal rate. This computational model was developed in collaboration with Kun Tian and Astrid Prinz.

5.6.2 *Impalement simulation*

To replicate impalement injury, an additional leak conductance was added to the model in order to simulate microelectrode impalement. This conductance, g_{imp}, was modeled as a non-selective ohmic leak channel with E_{imp} = −15mV. The impalement reversal potential was estimated by solving the Goldman-Hodgkin-Katz equation, [8], with equal permeabilities of the three major

ionic species. This estimate agrees well with estimates of impalement reversal potential in bullfrog ganglia (Brown, 1988). For analysis, model neurons were subjected to a bias current and held at −70mV, unless otherwise stated. g_{imp} was normally set at 0nS, and was only included where indicated for simulation of impalement.

$$E_m = \frac{RT}{F} ln\left(\frac{P_{Na}[Na^+]_{out} + P_K[K^+]_{out} + P_{Cl}[Cl^-]_{in}}{P_{Na}[Na^+]_{in} + P_K[K^+]_{in} + P_{Cl}[Cl^-]_{out}}\right) \qquad [8]$$

5.6.3 *Synapse simulation*

Synaptic input was implemented with equation:

$$I_{syn}(t) = A \cdot g_{syn}(t) \cdot \left(V - E_{syn}\right) \qquad [9]$$

where I_{syn} is synaptic current, A is conductance amplitude, and E_{syn} is the synaptic reversal potential set at 0mV. Synaptic conductance, g_{syn}, was calculated from the equation:

$$g_{syn}(t) = s \cdot \left(e^{-t/\tau_d} - e^{-t/\tau_r}\right) \qquad [10]$$

where τ_r and τ_d are the rise and decay time constants, respectively, and s is a scaling factor to normalize the amplitude to 1nS. Equations were adapted from Springer et al. (2015). Rise and decay time constants were 1 and 15ms, respectively, as estimated from voltage clamp recordings of spontaneous synaptic activity. We assume that synapses are very near cell somata and that a single-compartment model can sufficiently reproduce observed phenomena.

5.6.4 *Code accessibility*

Source code for all simulation and analysis are available online at https://github.com/pinewave/tSPN and ModelDB (Hines et al., 2004, accession #245926). Simulation and analysis scripts were written in Python 2.7.10 and executed in PyCharm (CE 2017.1.2) on macOS 10.12.3 with a 1.7-GHz processor. Scripts were also translated into MATLAB code and executed on Windows 10 with a 2.4-GHz processor. All differential

equations were integrated using an Exponential Euler method with a time step of 0.1 ms (Prinz et al., 2004).

5.7 **Experimental design and Statistical analysis**

The present study used a descriptive design. Statistical analyses were performed in Microsoft Excel. Basic properties are presented as mean ± SD in Table 2.2. Correlations were determined by Pearson's correlation coefficient, r. A two-tailed t-test was used to calculate each p-value. To control for 30 multiple comparisons and maintain an experiment-wise $\alpha=0.05$, a Šidák corrected $\alpha=0.0017$ was used to assign statistical significance. In some cases, parameter pairs with moderate values of r, ($|r|>0.4$) failed to reach significance as a result of intrinsic variability inherent within this data. Such correlations are reported as moderate, and should be interpreted cautiously. Exact r, R^2, and p-values are presented in Table 2.3.

Current	G_{max} (nS)	E_{rev} (mV)
I_{Na}	300	0
I_{CaL}	1.2	120
I_{Kd}	2000	−90
I_{M}	50	”
I_{KCa}	50	”
I_{A}	50	”
I_{H}	1	−32
I_{leak}	1	−55
I_{imp}*	0	−15

Table 5.1 Model parameters
Maximal conductance and reversal potential for the standard model neuron used for computational analysis. *Note that I_{imp} is set to 0nS as it is only included in simulations concerned with microelectrode impalement.

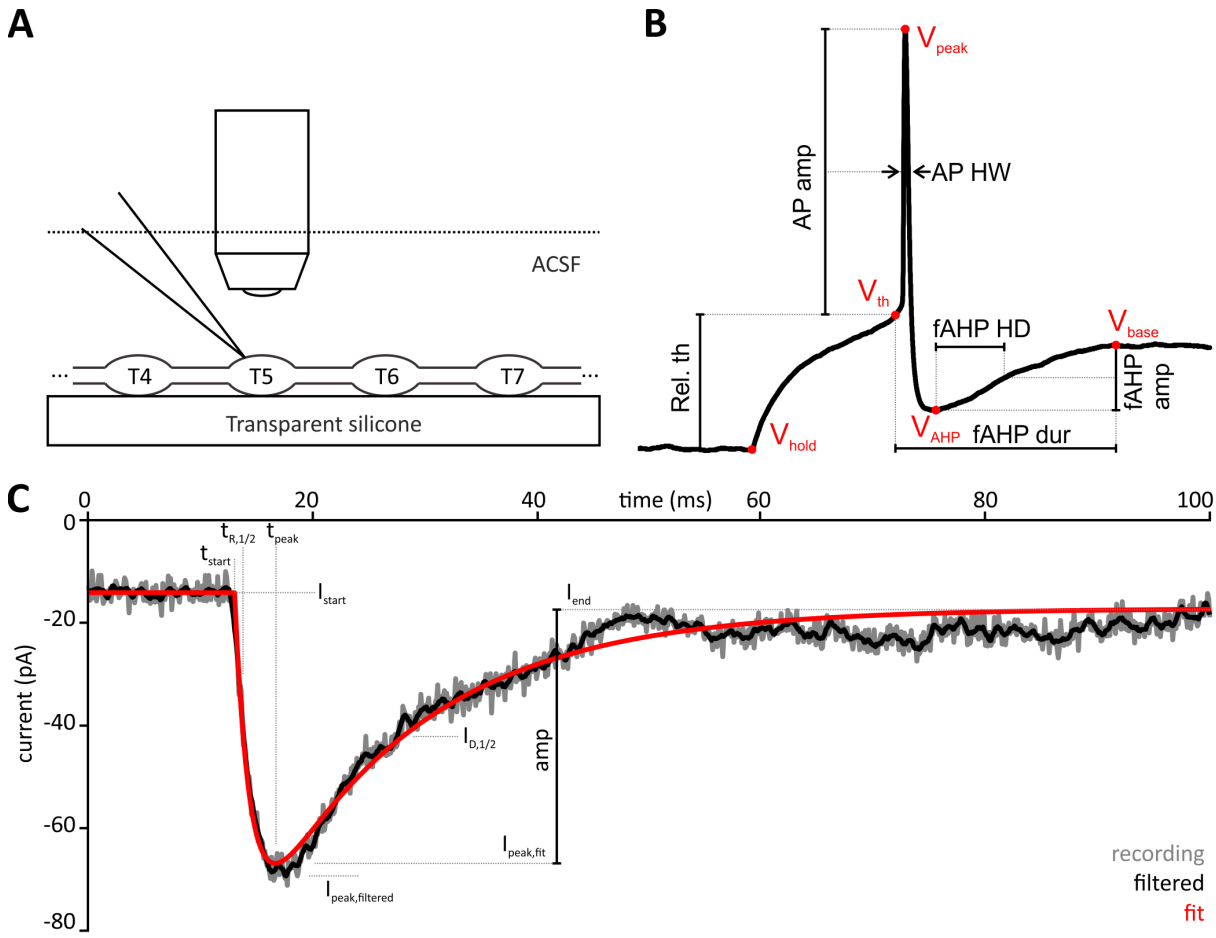

Figure 5.1 Methods

A, General setup for whole-cell recording. Tissue is pinned down onto transparent silicone and imaged with an immersion lens. B, Explanation of action potential and fAHP parameters. Rel. th, relative threshold; V_{hold}, holding voltage; V_{th}, absolute threshold; AP amp, action potential amplitude; V_{peak}, action potential peak voltage; AP HW, action potential half-width; fAHP dur; fAHP duration; fAHD HD, fAHP half-decay time; fAHP amp, fAMP amplitude. C, EPSC fitting method. Recorded trace (black) is filtered with a Savitsky-Golay filter (gray), and fitted to a template function using the Levenberg-Marquardt algorithm. t_{start}, event start time; $t_{R,1/2}$, time at half rise; t_{peak}, time of peak; I_{start}, baseline current; I_{peak}, most negative value for the filtered and fitted traces; $I_{D,1/2}$, current at half decay; I_{end}, final current; amp, amplitude is the difference between I_{end} and $I_{peak,fit}$.

6 Appendix

6.1 Equations for computational model

6.1.1 *Fast Na+ current:*

$$\alpha_m = 0.36 \cdot \frac{V+33}{1-e^{\frac{-(V+33)}{3}}} \qquad \alpha_h = -0.1 \cdot \frac{V+55}{1-e^{\frac{-(V+55)}{6}}}$$

$$\beta_m = -0.4 \cdot \frac{V+42}{1-e^{\frac{-(V+42)}{20}}} \qquad \beta_h = \frac{4.5}{1+e^{\frac{-V}{10}}}$$

$$\tau_m = \frac{2}{\alpha_m + \beta_m} \qquad \tau_h = \frac{2}{\alpha_h + \beta_h}$$

$$m_\infty = \frac{\alpha_m}{\alpha_m + \beta_m} \qquad h_\infty = \frac{\alpha_h}{\alpha_h + \beta_h}$$

$$\frac{dm}{dt} = \frac{m_\infty - m}{\tau_m} \qquad \frac{dh}{dt} = \frac{h_\infty - h}{\tau_h}$$

$$g_{Na} = G_{Na} \cdot m^2 h$$

$$I_{Na} = g_{Na} \cdot (V - E_{Na})$$

6.1.2 *Delayed rectifier K+ current:*

$$\alpha_n = 0.0047 \cdot \frac{V+12}{1-e^{\frac{-(V+12)}{12}}}$$

$$\beta_n = e^{\frac{-(V+147)}{30}}$$

$$\tau_n = \frac{1}{\alpha_n + \beta_n}$$

$$n_\infty = \frac{\alpha_n(V-20)}{\alpha_n(V-20) + \beta_n(V-20)}$$

$$\frac{dn}{dt} = \frac{n_\infty - n}{\tau_n}$$

$$g_K = G_K \cdot n^4$$

$$I_K = g_K \cdot (V - E_K)$$

6.1.3 *L-type Ca2+ current:*

$$\alpha_m = \frac{7.5}{1 + e^{\frac{-(V-13)}{7}}} \qquad \alpha_h = \frac{0.0068}{1 + e^{\frac{(V+30)}{12}}}$$

$$\beta_m = \frac{1.65}{1 + e^{\frac{(V-14)}{4}}} \qquad \beta_h = \frac{0.06}{1 + e^{\frac{-V}{11}}}$$

$$\tau_m = \frac{1}{\alpha_m + \beta_m} \qquad \tau_h = \frac{1}{\alpha_h + \beta_h}$$

$$m_\infty = \frac{\alpha_m}{\alpha_m + \beta_m} \qquad h_\infty = \frac{\alpha_h}{\alpha_h + \beta_h}$$

$$\frac{dm}{dt} = \frac{m_\infty - m}{\tau_m} \qquad \frac{dh}{dt} = \frac{h_\infty - h}{\tau_h}$$

$$g_{CaL} = G_{CaL} \cdot mh$$

$$I_{CaL} = g_{CaL} \cdot (V - E_{Ca})$$

6.1.4 *M-type K+ current:*

$$\tau_m = \frac{2000}{3.3 \cdot \left(e^{\frac{(V+35)}{40}} + e^{\frac{-(V+35)}{20}}\right)}$$

$$m_\infty = \frac{1}{1 + e^{\frac{-(V+35)}{10}}}$$

$$\frac{dm}{dt} = \frac{m_\infty - m}{\tau_m}$$

$$g_M = G_M \cdot m^2$$

$$I_M = g_M \cdot (V - E_K)$$

6.1.5 *Ca2+-dependent K+ current:*

$$\tau_m = \frac{50}{1 + [Ca^{2+}]^2}$$

$$m_\infty = \frac{[Ca^{2+}]^2}{[Ca^{2+}]^2 + 1}$$

$$\frac{dm}{dt} = \frac{m_\infty - m}{\tau_m}$$

$$g_{KCa} = G_{KCa} \cdot m$$

$$I_{KCa} = g_{KCa} \cdot (V - E_K)$$

6.1.6 *A-type K+ current:*

$$\tau_m = 0.3632 + \frac{1.158}{1 + e^{\frac{V+55.96}{20.12}}}$$

$$\tau_h = 0.124 + \frac{2.678}{1 + e^{\frac{V+50}{16.027}}}$$

$$m_\infty = \left(0.0761 \cdot \frac{e^{\frac{V+94.22}{31.84}}}{1 + e^{\frac{V+1.17}{28.93}}}\right)^{\frac{1}{3}}$$

$$h_\infty = \left(\frac{1}{1 + e^{0.069 \cdot (V+53.3)}}\right)^4$$

$$\frac{dm}{dt} = \frac{m_\infty - m}{\tau_m}$$

$$\frac{dh}{dt} = \frac{h_\infty - h}{\tau_h}$$

$$g_A = G_A \cdot m^3 h$$

$$I_A = g_A \cdot (V - E_K)$$

6.1.7 *H-current:*

$$\tau_m = \begin{cases} 53.5 + 67.7 \cdot e^{\frac{V+120}{22.4}}, & \frac{dm_\infty}{dt} > 0 \\ 40.9 - 0.45 \cdot V, & \frac{dm_\infty}{dt} \leq 0 \end{cases}$$

$$m_\infty = \frac{1}{1 + e^{\frac{V+87.6}{11.7}}}$$

$$\frac{dm}{dt} = \frac{m_\infty m}{\tau_m}$$

$$g_h = G_h \cdot m$$

$$I_h = g_h \cdot (V - E_h)$$

6.1.8 *Leak current:*

$$I_{leak} = G_{leak} \cdot (V - E_{leak})$$

6.1.9 *Injury current:*

$$I_{injury} = G_{injury} \cdot \left(V - E_{injury}\right)$$

6.1.10 *Synaptic current:*

$$g_{syn}(t) = s \cdot \left(e^{-t/15} - e^{-t/1}\right)$$

$$I_{syn} = \sum_{i=1}^{n_{events}} A_i \cdot g_{syn}(t - t_i) \cdot \left(V - E_{syn}\right)$$

6.1.11 *Somatic [Ca2+]:*

$$\frac{d}{dt}[Ca^{2+}] = 0.01 \cdot (-0.002 \cdot I_{CaL} - 0.024 \cdot [Ca^{2+}])$$

6.1.12 *Master equation:*

$$C_m \frac{dV}{dt} = -I_{input} - \sum I_i$$

7 References

Anderson KD (2004) Targeting recovery: priorities of the spinal cord-injured population. Journal of neurotrauma 21:1371–1383.

Ascoli GA, Gasparini S, Medinilla V, Migliore M (2010) Local control of postinhibitory rebound spiking in CA1 pyramidal neuron dendrites. J Neurosci 30:6434-6442.

Bartness TJ, Vaughan CH, Song CK (2010) Sympathetic and sensory innervation of brown adipose tissue. Int J Obes (Lond) 34 Suppl 1:S36-42.

Belluzzi O, Sacchi O (1988) The interactions between potassium and sodium currents in generating action potentials in the rat sympathetic neurone. J Physiol 397:127-147.

Belluzzi O, Sacchi O (1991) A five-conductance model of the action potential in the rat sympathetic neurone. Prog Biophys Mol Biol 55:1-30.

Belluzzi O, Sacchi O, Wanke E (1985) A fast transient outward current in the rat sympathetic neurone studied under voltage-clamp conditions. J Physiol 358:91-108.

Benda J, Herz AV (2003) A universal model for spike-frequency adaptation. Neural Comput 15:2523-2564.

Benda J, Tabak J (2013) Spike-Frequency Adaptation. In: Encyclopedia of Computational Neuroscience (Jaeger D, Jung R, eds), pp 1-12. New York, NY: Springer New York.

Bhalla US, Bower JM (1993) Exploring parameter space in detailed single neuron models: simulations of the mitral and granule cells of the olfactory bulb. J Neurophysiol 69:1948-1965.

Bini G, Hagbarth KE, Wallin BG (1981) Cardiac rhythmicity of skin sympathetic activity recorded from peripheral nerves in man. J Auton Nerv Syst 4:17-24.

Blackman JG, Purves RD (1969) Intracellular recordings from ganglia of the thoracic sympathetic chain of the guinea-pig. The Journal of physiology 203:173–198.

Blumberg H, Janig W (1983) Enhancement of resting activity in postganglionic vasoconstrictor neurones following short-lasting repetitive activation of preganglionic axons. Pflugers Arch 396:89-94.

Bobryshev AY, Skok VI (2002) Fast excitatory postsynaptic currents in neurons of the rabbit pelvic plexus. Auton Neurosci 99:78-84.

Bratton B, Davies P, Jänig W, McAllen R (2010) Ganglionic transmission in a vasomotor pathway studied *in vivo*: Vasomotor ganglionic transmission *in vivo*. The Journal of Physiology 588:1647-1659.

Brown A, Ricci MJ, Weaver LC (2004) NGF message and protein distribution in the injured rat spinal cord. Exp Neurol 188:115-127.

Brown AG (1981) Organization in the Spinal Cord: The Anatomy and Physiology of Identified Neurones: Springer London.

Brown DA (1988) M Currents. In: Ion Channels (Narahashi T, ed), pp 55-94.

Brown DA, Constanti A (1980) Intracellular observations on the effects of muscarinic agonists on rat sympathetic neurones. Br J Pharmacol 70:593-608.

Brown DA, Adams PR (1980) Muscarinic suppression of a novel voltage-sensitive K+ current in a vertebrate neurone. Nature 283:673-676.

Brownstone RM, Jordan LM, Kriellaars DJ, Noga BR, Shefchyk SJ (1992) On the regulation of repetitive firing in lumbar motoneurones during fictive locomotion in the cat. Exp Brain Res 90:441-455.

Cassell JF, McLachlan EM (1986) The effect of a transient outward current (IA) on synaptic potentials in sympathetic ganglion cells of the guinea-pig. The Journal of Physiology 374:273-288.

Cassell JF, Clark AL, McLachlan EM (1986) Characteristics of phasic and tonic sympathetic ganglion cells of the guinea-pig. J Physiol 372:457-483.

Cho HM, Lee DY, Sung SW (2005) Anatomical variations of rami communicantes in the upper thoracic sympathetic trunk. Eur J Cardiothorac Surg 27:320-324.

Coggeshall RE, Galbraith SL (1978) Categories of axons in mammalian rami communicantes. Part II. J Comp Neurol 181:349-359.

Cole AE, Shinnick-Gallagher P (1984) Muscarinic inhibitory transmission in mammalian sympathetic ganglia mediated by increased potassium conductance. Nature 307:270-271.

Connor JA, Stevens CF (1971) Prediction of repetitive firing behaviour from voltage clamp data on an isolated neurone soma. J Physiol 213:31-53.

Constanti A, Galvan M (1983) M-current in voltage-clamped olfactory cortex neurones. Neurosci Lett 39:65-70.

Coote JH (1990) Bulbospinal serotonergic pathways in the control of blood pressure. J Cardiovasc Pharmacol 15 Suppl 7:S35-41.

Cymbalyuk GS, Gaudry Q, Masino MA, Calabrese RL (2002) Bursting in leech heart interneurons: cell-autonomous and network-based mechanisms. J Neurosci 22:10580-10592.

Davies PJ, Ireland DR, McLachlan EM (1996) Sources of Ca2+ for different Ca(2+)-activated K+ conductances in neurones of the rat superior cervical ganglion. J Physiol 495 (Pt 2):353-366.

De Schutter E (2010) Computational Modeling Methods for Neuroscientists. Campbridge, MA: The MIT Press.

Del Signore A, Gotti C, Rizzo A, Moretti M, Paggi P (2004) Nicotinic acetylcholine receptor subtypes in the rat sympathetic ganglion: pharmacological characterization, subcellular distribution and effect of pre- and postganglionic nerve crush. J Neuropathol Exp Neurol 63:138-150.

Derkach VA, Selyanko AA, Skok VI (1983) Acetylcholine-induced current fluctuations and fast excitatory post-synaptic currents in rabbit sympathetic neurones. J Physiol 336:511-526.

Deuchars SA, Lall VK (2015) Sympathetic preganglionic neurons: properties and inputs. Compr Physiol 5:829-869.

Docherty JR (2010) Subtypes of functional alpha1-adrenoceptor. Cell Mol Life Sci 67:405-417.

Eccles JC (1935) The action potential of the superior cervical ganglion. The Journal of physiology 85:179–206.

Eccles RM, Libet B (1961) Origin and blockade of the synaptic responses of curarized sympathetic ganglia. J Physiol 157:484-503.

Edelstein SJ, Schaad O, Henry E, Bertrand D, Changeux JP (1996) A kinetic mechanism for nicotinic acetylcholine receptors based on multiple allosteric transitions. Biol Cybern 75:361-379.

Elfvin L-G, Lindh B, Hökfelt T (1993) The chemical neuroanatomy of sympathetic ganglia. Annual review of neuroscience 16:471–507.

Engbers JD, Anderson D, Tadayonnejad R, Mehaffey WH, Molineux ML, Turner RW (2011) Distinct roles for I(T) and I(H) in controlling the frequency and timing of rebound spike responses. J Physiol 589:5391-5413.

Ermentrout GB, Terman DH (2010) Mathematical Foundations of Neuroscience.

Ermolyuk YS, Alder FG, Surges R, Pavlov IY, Timofeeva Y, Kullmann DM, Volynski KE (2013) Differential triggering of spontaneous glutamate release by P/Q-, N- and R-type Ca2+ channels. Nat Neurosci 16:1754-1763.

Erulkar SD, Woodward JK (1968) Intracellular recording from mammalian superior cervical ganglion in situ. J Physiol 199:189-203.

Fagius J, Wallin BG, Sundlof G, Nerhed C, Englesson S (1985) Sympathetic outflow in man after anaesthesia of the glossopharyngeal and vagus nerves. Brain 108 (Pt 2):423-438.

Ferrante M, Shay CF, Tsuno Y, William Chapman G, Hasselmo ME (2017) Post-Inhibitory Rebound Spikes in Rat Medial Entorhinal Layer II/III Principal Cells: In Vivo, In Vitro, and Computational Modeling Characterization. Cereb Cortex 27:2111-2125.

Furlan A, La Manno G, Lubke M, Haring M, Abdo H, Hochgerner H, Kupari J, Usoskin D, Airaksinen MS, Oliver G, Linnarsson S, Ernfors P (2016) Visceral motor neuron diversity delineates a cellular basis for nipple- and pilo-erection muscle control. Nat Neurosci 19:1331-1340.

Galvan M, Sedlmeir C (1984) Outward currents in voltage-clamped rat sympathetic neurones. J Physiol 356:115-133.

George MS, Abbott LF, Siegelbaum SA (2009) HCN hyperpolarization-activated cation channels inhibit EPSPs by interactions with M-type K(+) channels. Nat Neurosci 12:577-584.

Gibbins I (2013) Functional organization of autonomic neural pathways. Organogenesis 9:169-175.

Gibbins IL (1991) Vasomotor, pilomotor and secretomotor neurons distinguished by size and neuropeptide content in superior cervical ganglia of mice. J Auton Nerv Syst 34:171-183.

Gibbins IL, Rodgers HF, Matthew SE, Murphy SM (1998) Synaptic organisation of lumbar sympathetic ganglia of guinea pigs: serial section ultrastructural analysis of dye-filled sympathetic final motor neurons. J Comp Neurol 402:285-302.

Gibbins IL, Jobling P, Messenger JP, Teo EH, Morris JL (2000) Neuronal morphology and the synaptic organisation of sympathetic ganglia. Journal of the Autonomic Nervous System 81:104–109.

Gilbey MP, Peterson DF, Coote JH (1982) Some characteristics of sympathetic preganglionic neurones in the rat. Brain Res 241:43-48.

Golowasch J, Thomas G, Taylor AL, Patel A, Pineda A, Khalil C, Nadim F (2009) Membrane capacitance measurements revisited: dependence of capacitance value on measurement method in nonisopotential neurons. J Neurophysiol 102:2161-2175.

Gonsalvez DG, Kerman IA, McAllen RM, Anderson CR (2010) Chemical coding for cardiovascular sympathetic preganglionic neurons in rats. J Neurosci 30:11781-11791.

Gonzalez-Islas C, Bulow P, Wenner P (2018) Regulation of synaptic scaling by action potential-independent miniature neurotransmission. J Neurosci Res 96:348-353.

Gustafsson B, Pinter MJ (1984) An investigation of threshold properties among cat spinal alpha-motoneurones. The Journal of Physiology 357:453.

Guyenet PG (2006) The sympathetic control of blood pressure. Nature Reviews Neuroscience 7:335-346.

Haley JE, Delmas P, Offermanns S, Abogadie FC, Simon MI, Buckley NJ, Brown DA (2000) Muscarinic inhibition of calcium current and M current in Galpha q-deficient mice. J Neurosci 20:3973-3979.

Hines ML, Morse T, Migliore M, Carnevale NT, Shepherd GM (2004) ModelDB: A Database to Support Computational Neuroscience. J Comput Neurosci 17:7-11.

Hirst GD, McLachlan EM (1984) Post-natal development of ganglia in the lower lumbar sympathetic chain of the rat. J Physiol 349:119-134.

Hochman S, McCrea DA (1994) Effects of chronic spinalization on ankle extensor motoneurons. II. Motoneuron electrical properties. Journal of Neurophysiology 71:1468–1479.

Hodges GJ, Jackson DN, Mattar L, Johnson JM, Shoemaker JK (2009) Neuropeptide Y and neurovascular control in skeletal muscle and skin. Am J Physiol Regul Integr Comp Physiol 297:R546-555.

Hodgkin AL, Huxley AF (1952) A quantitative description of membrane current and its application to conduction and excitation in nerve. J Physiol 117:500-544.

Hoffman DA, Magee JC, Colbert CM, Johnston D (1997) K+ channel regulation of signal propagation in dendrites of hippocampal pyramidal neurons. Nature 387:869-875.

Horn JP, Dodd J (1981) Monosynaptic muscarinic activation of K+ conductance underlies the slow inhibitory postsynaptic potential in sympathetic ganglia. Nature 292:625-627.

Horn JP, Kullmann PHM (2007) Dynamic clamp analysis of synaptic integration in sympathetic ganglia. Neurophysiology 39:423-429.

Hou S, Rabchevsky AG (2014) Autonomic consequences of spinal cord injury. Compr Physiol 4:1419-1453.

Hou S, Duale H, Rabchevsky AG (2009) Intraspinal sprouting of unmyelinated pelvic afferents after complete spinal cord injury is correlated with autonomic dysreflexia induced by visceral pain. Neuroscience 159:369-379.

Hou S, Duale H, Cameron AA, Abshire SM, Lyttle TS, Rabchevsky AG (2008) Plasticity of lumbosacral propriospinal neurons is associated with the development of autonomic dysreflexia after thoracic spinal cord transection. J Comp Neurol 509:382-399.

Hu Y, Converse C, Lyons MC, Hsu WH (2018) Neural control of sweat secretion: a review. Br J Dermatol 178:1246-1256.

Innes IR, Kosterlitz HW (1954) The effects of preganglionic and postganglionic denervation on the responses of the nictitating membrane to sympathomimetic substances. J Physiol 124:25-43.

Inokuchi H, McLachlan EM (1995) Lack of evidence for P2X-purinoceptor involvement in fast synaptic responses in intact sympathetic ganglia isolated from guinea-pigs. Neuroscience 69:651-659.

Ireland DR (1999) Preferential formation of strong synapses during re-innervation of guinea-pig sympathetic ganglia. J Physiol 520 Pt 3:827-837.

Ireland DR, Davies PJ, McLachlan EM (1999) Calcium channel subtypes differ at two types of cholinergic synapse in lumbar sympathetic neurones of guinea-pigs. J Physiol 514 (Pt 1):59-69.

Ivanov A, Purves D (1989) Ongoing electrical activity of superior cervical ganglion cells in mammals of different size. J Comp Neurol 284:398-404.

Ivanov A, Lukomskaia N, Magazanik LG (1975) [The spontaneous electrical activity of the isolated rabbit superior cervical ganglion]. Neirofiziologiia 7:632-638.

Jain P, Raza K, Singh S, Kumari C, Kaler S, Rani N (2016) Lumbar sympathetic chain: anatomical variation and clinical perspectives. Clin Ter 167:185-187.

Janig W (1986) Spinal cord integration of visceral sensory systems and sympathetic nervous system reflexes. Prog Brain Res 67:255-277.

Janig W, Szulczyk P (1980) Functional properties of lumbar preganglionic neurones. Brain Res 186:115-131.

Janig W, Szulczyk P (1981) The organization of lumbar preganglionic neurons. J Auton Nerv Syst 3:177-191.

Janig W, Krauspe R, Wiedersatz G (1982) Transmission of impulses from pre- to postganglionic vasoconstrictor and sudomotor neurons. J Auton Nerv Syst 6:95-106.

Janig W, Krauspe R, Wiedersatz G (1984) Activation of postganglionic neurones via non-nicotinic synaptic mechanisms by stimulation of thin preganglionic axons. Pflugers Arch 401:318-320.

Jänig W (1985) Organization of the lumbar sympathetic outflow to skeletal muscle and skin of the cat hindlimb and tail. In: Reviews of Physiology, Biochemistry and Pharmacology, Volume 102, pp 119-213. Berlin, Heidelberg: Springer Berlin Heidelberg.

Jänig W (1988) Pre- and postganglionic vasoconstrictor neurons: differentiation, types, and discharge properties. Annu Rev Physiol 50:525-539.

Jänig W (2006) The Integrative Action of the Autonomic Nervous System: Cambridge University Press.

Jobling P, Gibbins IL (1999) Electrophysiological and morphological diversity of mouse sympathetic neurons. Journal of neurophysiology 82:2747–2764.

Karila P, Horn JP (2000) Secondary nicotinic synapses on sympathetic B neurons and their putative role in ganglionic amplification of activity. The Journal of Neuroscience 20:908–918.

Karlsson AK (1999) Autonomic dysreflexia. Spinal Cord 37:383-391.

Kavalali ET (2015) The mechanisms and functions of spontaneous neurotransmitter release. Nat Rev Neurosci 16:5-16.

Kawatani M, Rutigliano MJ, de Groat WC (1987) Vasoactive intestinal polypeptide facilitates the late component of the 5-hydroxytryptamine-induced discharge in the cat superior cervical ganglion. Neurosci Lett 73:59-64.

Kennedy C (2015) ATP as a cotransmitter in the autonomic nervous system. Auton Neurosci 191:2-15.

Kertser S, Bobryshev A, Voitenko S, Gmiro V, Brovtsyna N, Skok V (1998) Dimensions of neuronal nicotinic acetylcholine receptor channel as estimated from the analysis of the channel-blocking effects. J Membr Biol 163:111-118.

Kommuru H, Jothi S, Bapuji P, Sree DL, Antony J (2014) Thoracic part of sympathetic chain and its branching pattern variations in South Indian cadavers. J Clin Diagn Res 8:AC09-12.

Konig P, Engel AK, Singer W (1996) Integrator or coincidence detector? The role of the cortical neuron revisited. Trends Neurosci 19:130-137.

Krassioukov AV, Weaver LC (1995) Episodic hypertension due to autonomic dysreflexia in acute and chronic spinal cord-injured rats. Am J Physiol 268:H2077-2083.

Krassioukov AV, Weaver LC (1996) Morphological changes in sympathetic preganglionic neurons after spinal cord injury in rats. Neuroscience 70:211-225.

Krassioukov AV, Bunge RP, Pucket WR, Bygrave MA (1999) The changes in human spinal sympathetic preganglionic neurons after spinal cord injury. Spinal Cord 37:6-13.

Krenz NR, Weaver LC (1998) Sprouting of primary afferent fibers after spinal cord transection in the rat. Neuroscience 85:443-458.

Kullmann PH, Sikora KM, Clark KL, Arduini I, Springer MG, Horn JP (2016) HCN hyperpolarization-activated cation channels strengthen virtual nicotinic EPSPs and thereby elevate synaptic amplification in rat sympathetic neurons. J Neurophysiol 116:438-447.

Kuo DC, Yamasaki DS, Krauthamer GM (1980) Segmental organization of sympathetic preganglionic neurons of the splanchnic nerve as revealed by retrograde transport of horseradish peroxidase. Neurosci Lett 17:11-16.

Kurian M, Crook SM, Jung R (2011) Motoneuron model of self-sustained firing after spinal cord injury. J Comput Neurosci 31:625-645.

Lamas JA (1998) A hyperpolarization-activated cation current (Ih) contributes to resting membrane potential in rat superior cervical sympathetic neurones. Pflugers Arch 436:429-435.

Langley JN (1903) The Autonomic Nervous System. Brain 26:1-26.

Langley JN (1921) The Autonomic Nervous System. Part I. Cambridge: W. Heffer.

Langley JN, Dickinson WL (1889) III. On the local paralysis of peripheral ganglia, and on the connexion of different classes of nerve fibres with them. Proc Roy Soc Lond 46.

Lees GM, Wallis DI (1974) Hyperpolarization of rabbit superior cervical ganglion cells due to activity of an electrogenic sodium pump. Br J Pharmacol 50:79-93.

Lewis JC, Burton PR (1977) Ultrastructural studies of the superior cervical trunk of the mouse: distribution, cytochemistry and stability of fibrous elements in preganglionic fibers. J Comp Neurol 171:605-618.

Li C, Horn JP (2006) Physiological classification of sympathetic neurons in the rat superior cervical ganglion. J Neurophysiol 95:187-195.

Li C, McKinnon ML, Hochman S (in preparation) The impact of spinal cord injury on the Intrinsic membrane properties of thoracic postganglionic neurons In.

Libet B, Kobayashi H (1974) Adrenergic mediation of slow inhibitory postsynaptic potential in sympathetic ganglia of the frog. J Neurophysiol 37:805-814.

Lichtman JW, Purves D, Yip JW (1980) Innervation of sympathetic neurones in the guinea-pig thoracic chain. The Journal of physiology 298:285–299.

Liestol K, Maehlen J, Nja A (1987) Two types of synaptic selectivity and their interrelation during sprouting in the guinea-pig superior cervical ganglion. J Physiol 384:233-245.

Llewellyn-Smith IJ, Weaver LC (2001) Changes in synaptic inputs to sympathetic preganglionic neurons after spinal cord injury. Journal of Comparative Neurology 435:226–240.

Locknar SA, Barstow KL, Tompkins JD, Merriam LA, Parsons RL (2004) Calcium-induced calcium release regulates action potential generation in guinea-pig sympathetic neurones. J Physiol 555:627-635.

Lu C, Fuchs E (2014) Sweat gland progenitors in development, homeostasis, and wound repair. Cold Spring Harb Perspect Med 4.

Luther JA, Birren SJ (2009) p75 and TrkA signaling regulates sympathetic neuronal firing patterns via differential modulation of voltage-gated currents. J Neurosci 29:5411-5424.

MacDermott AB, Connor EA, Dionne VE, Parsons RL (1980) Voltage clamp study of fast excitatory synaptic currents in bullfrog sympathetic ganglion cells. J Gen Physiol 75:39-60.

Madden CJ, Morrison SF (2006) Serotonin potentiates sympathetic responses evoked by spinal NMDA. J Physiol 577:525-537.

Maingret F, Coste B, Hao J, Giamarchi A, Allen D, Crest M, Litchfield DW, Adelman JP, Delmas P (2008) Neurotransmitter modulation of small-conductance Ca2+-activated K+ channels by regulation of Ca2+ gating. Neuron 59:439-449.

Mallory BS (1994) Autonomic Function in the Isolated Spinal Cord. In: The Physiological Basis of Rehabilitation Medicine, 2 Edition (John A. Downey SJM, Erwin G. Gonzalez, James S. Lieberman, ed), pp 519-541.

Marina N, Taheri M, Gilbey MP (2006) Generation of a physiological sympathetic motor rhythm in the rat following spinal application of 5-HT. J Physiol 571:441-450.

Masliukov PM, Timmermans JP (2004) Immunocytochemical properties of stellate ganglion neurons during early postnatal development. Histochem Cell Biol 122:201-209.

Mathias CJ (2006) Orthostatic hypotension and paroxysmal hypertension in humans with high spinal cord injury. Prog Brain Res 152:231-243.

Mathias CJ, Frankel HL, Christensen NJ, Spalding JM (1976) Enhanced pressor response to noradrenaline in patients with cervical spinal cord transection. Brain 99:757-770.

McKinnon ML, Tian K, Li Y, Sokoloff AJ, Galvin ML, Choi MH, Prinz A, Hochman S (2019) Dramatically amplified thoracic sympathetic postganglionic excitability and integrative capacity revealed with whole-cell patch clamp recordings. eNeuro.

McLachlan EM (1974) The formation of synapses in mammalian sympathetic ganglia reinnervated with preganglionic or somatic nerves. J Physiol 237:217-242.

McLachlan EM (1975) An analysis of the release of acetylcholine from preganglionic nerve terminals. J Physiol 245:447-466.

McLachlan EM (2003) Transmission of signals through sympathetic ganglia--modulation, integration or simply distribution? Acta Physiol Scand 177:227-235.

McLachlan EM (2007) Diversity of sympathetic vasoconstrictor pathways and their plasticity after spinal cord injury. Clinical Autonomic Research 17:6-12.

McLachlan EM, Davies PJ, Habler HJ, Jamieson J (1997) On-going and reflex synaptic events in rat superior cervical ganglion cells. J Physiol 501 (Pt 1):165-181.

McLachlan EM, Habler HJ, Jamieson J, Davies PJ (1998) Analysis of the periodicity of synaptic events in neurones in the superior cervical ganglion of anaesthetized rats. J Physiol 511 (Pt 2):461-478.

Miao FJ, Kinnman E, Janig W, Levine JD (1995) Variation in the anatomy of the lumbar sympathetic chain in the rat. J Auton Nerv Syst 56:115-118.

Miles GB, Dai Y, Brownstone RM (2005) Mechanisms underlying the early phase of spike frequency adaptation in mouse spinal motoneurones: Mechanisms underlying SFA in spinal motoneurones. The Journal of Physiology 566:519-532.

Murata Y, Takahashi K, Yamagata M, Takahashi Y, Shimada Y, Moriya H (2003) Variations in the number and position of human lumbar sympathetic ganglia and rami communicantes. Clin Anat 16:108-113.

Murphy SM, Matthew SE, Rodgers HF, Lituri DT, Gibbins IL (1998) Synaptic organisation of neuropeptide-containing preganglionic boutons in lumbar sympathetic ganglia of guinea pigs. J Comp Neurol 398:551-567.

Murray JG, Thompson JW (1957) The occurrence and function of collateral sprouting in the sympathetic nervous system of the cat. J Physiol 135:133-162.

Nagashima K, Nakai S, Tanaka M, Kanosue K (2000) Neuronal circuitries involved in thermoregulation. Auton Neurosci 85:18-25.

Nishi S, Koketsu K (1960) Electrical properties and activities of single sympathetic neurons in frogs. J Cell Comp Physiol 55:15-30.

Njå A, Purves D (1977a) Specific innervation of guinea-pig superior cervical ganglion cells by preganglionic fibres arising from different levels of the spinal cord. The Journal of physiology 264:565–583.

Njå A, Purves D (1977b) Re-innervation of guinea-pig superior cervical ganglion cells by preganglionic fibres arising from different levels of the spinal cord. The Journal of physiology 272:633–651.

Njå A, Purves D (1978) Specificity of initial synaptic contacts made on guinea-pig superior cervical ganglion cells during regeneration of the cervical sympathetic trunk. The Journal of physiology 281:45–62.

North RA (1986) Mechanisms of Autonomic Integration. In: Compr Physiol 2011, Supplement 4: Handbook of Physiology, The Nervous System, Intrinsic Regulatory Systems of the Brain, pp 115-153.

Northcutt AJ, Lett KM, Garcia VB, Diester CM, Lane BJ, Marder E, Schulz DJ (2016) Deep sequencing of transcriptomes from the nervous systems of two decapod crustaceans to

characterize genes important for neural circuit function and modulation. BMC Genomics 17:868.

NSCISC (2019) National Spinal Cord Injury Statistical Center: Facts and Figures at a Glance. In. Birmingham, AL: University of Alabama at Birmingham.

Osborn JW, Taylor RF, Schramm LP (1989) Determinants of arterial pressure after chronic spinal transection in rats. Am J Physiol 256:R666-673.

Pape H-C (1996) Queer current and pacemaker: The Hyperpolarization-Activated Cation Current in Neurons. Annual Reviews Physiology 58:299-327.

Picton LD, Nascimento F, Broadhead MJ, Sillar KT, Miles GB (2017) Sodium Pumps Mediate Activity-Dependent Changes in Mammalian Motor Networks. J Neurosci 37:906-921.

Platkiewicz J, Brette R (2010) A threshold equation for action potential initiation. PLoS Comput Biol 6:e1000850.

Powers RK, Sawczuk A, Musick JR, Binder MD (1999) Multiple mechanisms of spike-frequency adaptation in motoneurones. The Journal of Physiology 93:101-114.

Prescott SA, Ratte S, De Koninck Y, Sejnowski TJ (2006) Nonlinear interaction between shunting and adaptation controls a switch between integration and coincidence detection in pyramidal neurons. J Neurosci 26:9084-9097.

Prinz AA, Bucher D, Marder E (2004) Similar network activity from disparate circuit parameters. Nat Neurosci 7:1345-1352.

Purves D, Hume RI (1981) The relation of postsynaptic geometry to the number of presynaptic axons that innervate autonomic ganglion cells. J Neurosci 1:441-452.

Purves D, Wigston DJ (1983) Neural units in the superior cervical ganglion of the guinea-pig. J Physiol 334:169-178.

Purves D, Rubin E, Snider WD, Lichtman J (1986) Relation of animal size to convergence, divergence, and neuronal number in peripheral sympathetic pathways. J Neurosci 6:158-163.

Pyner S, Coote JH (1994) A comparison between the adult rat and neonate rat of the architecture of sympathetic preganglionic neurones projecting to the superior cervical ganglion, stellate ganglion and adrenal medulla. J Auton Nerv Syst 48:153-166.

Queenan BN, Lee KJ, Pak DT (2012) Wherefore art thou, homeo(stasis)? Functional diversity in homeostatic synaptic plasticity. Neural Plast 2012:718203.

Rall W (2011) Core Conductor Theory and Cable Properties of Neurons. In: Handbook of Physiology, The Nervous System, Cellular Biology of Neurons, pp 39-97.

Ratte S, Hong S, De Schutter E, Prescott SA (2013) Impact of neuronal properties on network coding: roles of spike initiation dynamics and robust synchrony transfer. Neuron 78:758-772.

Rimmer K, Horn JP (2010) Weak and straddling secondary nicotinic synapses can drive firing in rat sympathetic neurons and thereby contribute to ganglionic amplification. Front Neurol 1:130.

Rittenhouse AR, Zigmond RE (1999) Role of N- and L-type calcium channels in depolarization-induced activation of tyrosine hydroxylase and release of norepinephrine by sympathetic cell bodies and nerve terminals. J Neurobiol 40:137-148.

Roth A, van Rossum M (2009) Modeling Synapses. In: Computational Modeling Methods for Neuroscientists, pp 139-159.

Rummery NM, Tripovic D, McLachlan EM, Brock JA (2010) Sympathetic vasoconstriction is potentiated in arteries caudal but not rostral to a spinal cord transection in rats. J Neurotrauma 27:2077-2089.

Rush ME, Rinzel J (1995) The potassium A-current, low firing rates and rebound excitation in Hodgkin-Huxley models. Bulletin of mathematical biology 57:899–929.

Sacchi O, Perri V (1971) Quantal release of acetylcholine from the nerve endings of the guinea-pig superior cervical ganglion. Pflugers Arch 329:207-219.

Sacchi O, Rossi ML, Canella R (1995) The slow Ca(2+)-activated K+ current, IAHP, in the rat sympathetic neurone. J Physiol 483 (Pt 1):15-27.

Sacchi O, Belluzzi O, Canella R, Fesce R (1998) A model of signal processing at a mammalian sympathetic neurone. J Neurosci Methods 80:171-180.

Sacchi O, Rossi ML, Canella R, Fesce R (2006) Synaptic and somatic effects of axotomy in the intact, innervated rat sympathetic neuron. J Neurophysiol 95:2832-2844.

Salinas E, Thier P (2000) Gain modulation: a major computational principle of the central nervous system. Neuron 27:15-21.

Sargent PB (2014) Autonomic Nervous System Transmission. In: Nicotinic Receptors (Lester RAJ, ed), pp 169-184: Humana Press.

Sawczuk A, Powers RK, Binder MD (1997) Contribution of outward currents to spike-frequency adaptation in hypoglossal motoneurons of the rat. J Neurophysiol 78:2246-2253.

Schafer MK, Eiden LE, Weihe E (1998) Cholinergic neurons and terminal fields revealed by immunohistochemistry for the vesicular acetylcholine transporter. II. The peripheral nervous system. Neuroscience 84:361-376.

Schobesberger H, Wheeler DW, Horn JP (2000) A model for pleiotropic muscarinic potentiation of fast synaptic transmission. J Neurophysiol 83:1912-1923.

Schulz DJ, Goaillard JM, Marder E (2006) Variable channel expression in identified single and electrically coupled neurons in different animals. Nat Neurosci 9:356-362.

Schutz B, Schafer MK, Gordes M, Eiden LE, Weihe E (2015) Satb2-independent acquisition of the cholinergic sudomotor phenotype in rodents. Cell Mol Neurobiol 35:205-216.

Serebryakova IY (2008) Dynamics of the remodeling of neural connections in the superior cervical ganglion in rats after dosed compression of the preganglionic trunk. Neurosci Behav Physiol 38:811-815.

Shafton AD, Oldfield BJ, McAllen RM (1992) CRF-like immunoreactivity selectively labels preganglionic sudomotor neurons in cat. Brain Res 599:253-260.

Shreckengost J (2011) On the mechanisms of presynaptic inhibition of primary afferents. In: Graduate Division of Biological and Biomedical Sciences: Emory University.

Skok VI (1973) Physiology of autonomic ganglia. Tokyo: Igaku Shoin.

Skok VI (2002) Nicotinic acetylcholine receptors in autonomic ganglia. Autonomic Neuroscience 97:1–11.

Skok VI, Ivanov AY (1983) What is the ongoing activity of sympathetic neurons? J Auton Nerv Syst 7:263-270.

Springer MG, Kullmann PHM, Horn JP (2015) Virtual leak channels modulate firing dynamics and synaptic integration in rat sympathetic neurons: implications for ganglionic transmission *in vivo*: Firing dynamics and synaptic gain in rat sympathetic neurons. The Journal of Physiology 593:803-823.

Staley KJ, Otis TS, Mody I (1992) Membrane properties of dentate gyrus granule cells: comparison of sharp microelectrode and whole-cell recordings. J Neurophysiol 67:1346-1358.

Standring S (2016) Gray's anatomy : the anatomical basis of clinical practice.

Stauffer EK, McDonagh JC, Hornby TG, Reinking RM, Stuart DG (2007) Historical reflections on the afterhyperpolarization--firing rate relation of vertebrate spinal neurons. J Comp Physiol A Neuroethol Sens Neural Behav Physiol 193:145-158.

Storm JF (1990) Potassium currents in hippocampal pyramidal cells. Prog Brain Res 83:161-187.

Tansey EA, Johnson CD (2015) Recent advances in thermoregulation. Adv Physiol Educ 39:139-148.

Tator CH (1995) Update on the pathophysiology and pathology of acute spinal cord injury. Brain Pathol 5:407-413.

Teasell RW, Arnold JMO, Krassioukov A, Delaney GA (2000) Cardiovascular consequences of loss of supraspinal control of the sympathetic nervous system after spinal cord injury. Archives of Physical Medicine and Rehabilitation 81:506-516.

Tripovic D, Pianova S, McLachlan EM, Brock JA (2010) Transient supersensitivity to alpha-adrenoceptor agonists, and distinct hyper-reactivity to vasopressin and angiotensin II after denervation of rat tail artery. Br J Pharmacol 159:142-153.

Tripovic D, Al Abed A, Rummery NM, Johansen NJ, McLachlan EM, Brock JA (2011) Nerve-evoked constriction of rat tail veins is potentiated and venous diameter is reduced after chronic spinal cord transection. J Neurotrauma 28:821-829.

Turrigiano G (2012) Homeostatic synaptic plasticity: local and global mechanisms for stabilizing neuronal function. Cold Spring Harb Perspect Biol 4:a005736.

Turrigiano GG, Leslie KR, Desai NS, Rutherford LC, Nelson SB (1998) Activity-dependent scaling of quantal amplitude in neocortical neurons. Nature 391:892-896.

Valli P, Zucca G, Botta L, Seghezzi R (1989) Lumbar sympathetic ganglia in man: an electrophysiological study in vitro. J Auton Nerv Syst 28:211-217.

Venance L, Glowinski J (2003) Heterogeneity of spike frequency adaptation among medium spiny neurones from the rat striatum. Neuroscience 122:77-92.

Voitenko SV, Bobryshev A, Skok VI (1998) [Intracellular regulation of neuronal nicotinic cholinergic receptors]. Ross Fiziol Zh Im I M Sechenova 84:985-993.

Wahlestedt C, Hakanson R, Vaz CA, Zukowska-Grojec Z (1990) Norepinephrine and neuropeptide Y: vasoconstrictor cooperation in vivo and in vitro. Am J Physiol 258:R736-742.

Weaver LC, Cassam AK, Krassioukov AV, Llewellyn-Smith IJ (1997) Changes in immunoreactivity for growth associated protein-43 suggest reorganization of synapses on spinal sympathetic neurons after cord transection. Neuroscience 81:535-551.

Wheeler DW, Kullmann PH, Horn JP (2004) Estimating use-dependent synaptic gain in autonomic ganglia by computational simulation and dynamic-clamp analysis. J Neurophysiol 92:2659-2671.

Willette RN, Hieble JP, Sauermelch CF (1991) Sympathetic regulation of cutaneous circulation in the rat. J Auton Nerv Syst 32:135-144.

Won HJ, Lee JE, Lee WT, Won HS (2018) Topographical study of the connections of the rami communicantes from the first to the fifth thoracic sympathetic ganglia. Clin Anat 31:1151-1157.

Yamada WM, Koch C, Adams PR (1989) Multiple channels and calcium dynamics- modeling bullfrog sympathetic ganglion cells. In: Methods in Neuronal Modeling: From Synapses to Networks (Koch C, Segev I, eds). Cambridge, MA: MIT press.

Yi G, Wang J, Tsang KM, Wei X, Deng B, Han C (2015) Spike-frequency adaptation of a two-compartment neuron modulated by extracellular electric fields. Biol Cybern 109:287-306.

Zhang HY, Sillar KT (2012) Short-term memory of motor network performance via activity-dependent potentiation of Na+/K+ pump function. Curr Biol 22:526-531.

Zimmerman A, Hochman S (2010) Heterogeneity of membrane properties in sympathetic preganglionic neurons of neonatal mice: evidence of four subpopulations in the intermediolateral nucleus. J Neurophysiol 103:490-498.